

Lattice Boltzmann Simulations of Some Novel Multiphase Flows

A Thesis Submitted to
Indian Institute of Technology Hyderabad
In Partial Fulfillment of the Requirements for
The Degree of

Doctor of Philosophy

by

Prasanna Rani Redapangu

Reg. No. CH10P007



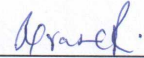
DEPARTMENT OF CHEMICAL ENGINEERING
INDIAN INSTITUTE OF TECHNOLOGY HYDERABAD
Hyderabad – 502 205

January 2014

To the Lord Almighty and my parents

DECLARATION

I hereby declare that this written submission represents my ideas in my own words, and where ideas or words of others have been included, I have adequately cited and referenced the original sources. I also declare that I have adhered to all principles of academic honesty and integrity and have not misrepresented or fabricated or falsified any idea/data/fact/source in my submission. I understand that any violation of the above will be a cause for disciplinary action by the Institute and can also evoke penal action from the sources that have thus not been properly cited, or from whom proper permission has not been taken when needed.



Prasanna Rani Redapangu

CH10P007

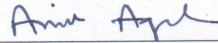
(Reg. No.)

APPROVAL SHEET

This thesis entitled "Lattice Boltzmann Simulations of Some Novel Multiphase Flows" by Ms. Prasanna Rani Redapangu is approved for the degree of Doctor of Philosophy from Indian Institute of Technology Hyderabad.



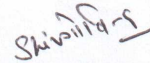
(Prof. R.P.Chhabra) Examiner
Department of Chemical Engineering
IIT Kanpur



(Prof. Amit Agrawal) Examiner
Department of Mechanical Engineering
IIT Bombay



(Dr. Vinod Janarthanan) Examiner
Department of Chemical Engineering
IIT Hyderabad



(Dr. Shiv Govind Singh) observer
Department of Electrical Engineering
IIT Hyderabad



(Prof. Kirti Chandra Sahu) Adviser
Department of Chemical Engineering
IIT Hyderabad

Acknowledgements

This thesis would not have been completed without the help, inspiration and support of many individuals.

My first and sincere gratitude goes to my advisor Dr. Kirti Chandra Sahu, for his continuous motivation and support in all stages of my Ph.D and for all I have learned from him. He has always made himself available to clarify my doubts despite his busy schedules and I consider it as a great opportunity and a great experience working with him.

I thank Prof. Surya Pratap Vanka, Department of Mechanical Science and Engineering, University of Illinois at Urbana-Champaign Urbana for collaborating with us and helping us in the development of GPU based lattice Boltzmann solver. I also thank him for his valuable suggestions throughout my research work.

I am very much grateful to my doctoral committee, Dr. Saptarshi Majumdar, Dr. Vinod Janarthanan and Dr. Raja Banerjee, for accessing my work and for their invaluable suggestions throughout my PhD.

I am very much thankful to my institute, Indian Institute of Technology Hyderabad and the Director, Prof. U. B. Desai, for providing a good research environment and excellent research facilities despite of all problems involved in a temporary campus. I thank the institute for granting financial aid to attend various national and international conferences. I would like to express my sincere gratitude to the head of the department, chemical engineering, Dr. Vinod Janarthanan and every faculty of the department for their support and encouragement in every possible way. I enjoyed every course I took during my PhD and learnt a lot from them.

I am also grateful to MHRD for providing scholarship during my PhD. I thank the department of science and technology (DST) for funding our project.

My group members Manoj, Ashima, Pinaki, Kusuma and Teja, with whom I worked with, are wonderful with excellent group spirit. I thank each of them for their cooperation, support and encouragement.

I am lucky enough to have very good friends in hostel who made my stay at IIT Hyderabad a very memorable one. Special thanks to Anusha, Vimala, Vandana, Vijaya, Meenakshi, Anupama, Anitha, Swetha Ram, Deepika, Sweta G, Unnisa, Dayamani, Remya, Vasavi and Satya Eswari. I remember each and every moment spent with them. They are always there beside me not only in every happy moment but also in times of trouble and depression. I heartfully thank them for the wonderful support and making IIT Hyderabad a home away from home.

My other PhD colleagues Ravi, Harikishan, Srinivas, Lakshmi, Balraju, Vishnu, Manohar, Nanda Kumar, Chandrasekhar, Sudhakar, Anindita, Jyothi, Susri are very cooperative and supportive. I may not have spent much valuable time with them, but each one of them is very special and I am heartfully thankful to them.

I thank Chakravarthy, Satish and Rahul of server room, Srikanth and Madhu of CAE and HPC labs for helping me in installing our workstations and various softwares. I thank each and every staff member of the institute, administration, academics, accounts, stores, library, hostel staff, security, care takers, warden, bus and cab drivers etc. for their service to achieve smooth, secured and peaceful stay at IIT Hyderabad.

I would also like to thank few people outside IIT Hyderabad. I thank Prof. Rama Govindarajan (TIFR Hyderabad) for her valuable suggestions both professionally as well as personally. The interaction with her during the APS DFD-2013, Pittsburgh conference trip was very memorable.

I thank Mr. Surender (Fujitsu technologies) for supplying us workstations and Nvidia GPU cards. I thank Accutech infosystems pvt. ltd. and emmerson technologies for supplying UPS to our workstations.

I am grateful to form close relation with Mrs. Vardini and family from Ordnance factory (in which the IIT Hyderabad temporary campus is situated). Their love, support and encouragement are ever memorable.

Finally I would like to thank my parents for their constant care and blessings which helped me to grow in both professional and social life. Their support and encouragement in every stage of my life is so precious and valuable. I would like to thank my brothers (David and Praveen), sister (Jyothi), sister-in-law (Usha) and brother-in-law (Ramesh (late)), and all my well-wishers for their love which gave me enough courage to face any situation.

*I believe that its my God who put these many people around me to love, care, guide and protect me in every situation I face. The prayers of my family, friends and well wishers are always my secret strength. I acknowledge that what I am today is purely because of God's grace and love. **"He is my strength and my shield"**.*

Synopsis

Multiphase flows can be observed in many naturally occurring phenomena such as rain, snow, avalanches, clouds, underground water flows, sea waves, etc. Multiphase flows are also common in many industrial processes, such as transportation of crude oil in pipelines; enhance oil recovery, hydrology, filtration, coating, and many other applications. In food processing industries, the cleaning of plants involves the removal of highly viscous fluid by fast flowing water streams injected at the inlet of the conduits. Therefore, the fundamental understanding of such flows is essential, thus attracting many experimentalists and theoreticians to investigate the miscible and immiscible systems in various flow configurations.

The main objective of the present thesis is to investigate the flow dynamics and instabilities occurring in buoyancy-driven and pressure-driven displacement flows of two immiscible liquids with varying viscosities and densities in two- and three-dimensional geometries. The resulting flow in such systems can give rise to several new instability patterns, which have been studied using lattice Boltzmann method (LBM) for multiphase flows [He *et al.* (1999*a,b*), Zhang *et al.* (2000), Sahu & Vanka (2011)]. The behavior of infinitesimal small disturbance is also investigated via a linear stability analysis, and the results are compared with those obtained from the LBM simulations.

The LBM is an alternative computational method for fluid flows and is found to be very promising for interfacial flows. It is a mesoscopic model derived from lattice gas automata. The explicit nature of this method and the absence of the pressure-Poisson equation (which is essential to satisfy the conservation of mass in conventional Navier-Stokes (N-S) solvers) make the method computationally very economical and an easily parallelizable technique. In addition to this, our LBM code is implemented on graphics processing unit (GPU), which gives 25 times speed up over the corresponding CPU based code. The GPU is a new paradigm for scientific computing. It is a powerful tool for performing parallel computations with less energy consumption (one GPU card requires only 150 Watts and it costs only Rs. 60,000-70,000). The LBM, which itself is computationally faster than the conventional N-S solvers, when implemented on GPU, gives a very high computational speed-up.

The various problems investigated in the present work are discussed below.

(i) Buoyancy-driven flow which is commonly known as lock-exchange flow refers to the interpenetration of two immiscible fluids initially separated by a partition and suddenly allowed to mix under the action of gravitational force. Considering miscible fluids having different density, but the same dynamic viscosity, this problem has been studied experimentally and numerically by many researchers [Séon *et al.* (2004), Séon *et al.* (2007*a,b*), Hallez & Magnaudet (2008)]. In the present work, the buoyancy-induced interpenetration of two immiscible fluids of varying viscosities and densities is investigated in a confined tilted channel. In this configuration, the gravitational force has two components, which act in the axial and transverse directions. The axial component of gravity

induces a downward motion of the heavier fluid, which in turn, by mass conservation, displaces the lighter fluid to move into the region of the heavier fluid. Thus both the heavier and the lighter fluids accelerate into the lower and the upper parts of the channel, respectively. On the other hand, the component of the gravitational force in the transverse direction, acts to segregate the two fluids. The interface between the fluids becomes unstable, which give rise to the development of the interfacial instabilities.

The main aim of this study is to investigate the effects of viscosity differential on the flow dynamics. For high viscosity ratios relatively stable fingers are observed, which move essentially like two individual Poiseuille flows in the opposite directions. The intensity of interfacial instabilities increases with decreasing viscosity differential of the fluids and the flow becomes progressively more complex. The front velocities decrease with increase in viscosity ratios. The effect of other parameters like the angle of inclination and surface tension are also investigated. A three-dimensional extension of this study is carried out and the results are compared with those obtained in two-dimensional channel.

(ii) Next, the effects of imposed pressure-gradient on the flow dynamics has been investigated. In this case, the displacement of an initially resident fluid inside the channel by another fluid of different viscosity and density, which is injected at the inlet, has been studied. As discussed above, the displacement flow of one fluid by another one can be found in many industrial and geological applications. In this case, the flow dynamics is a result of the competition between the imposed pressure-gradient and the axial component of gravity. The pressure-driven flow induces motion of displacing fluid into the channel, whereas the axial component of the gravity opposes this force by accelerating the displaced fluid in the upstream direction. When a less viscous fluid displaces a high viscous fluid, the flow becomes unstable forming interesting instability patterns at the interface separating the fluids.

This is a parametrically rich problem, involving several dimensionless parameters, such as, viscosity ratio, Atwood number, Reynolds number, Froude number, Capillary number and angle of inclination. A detailed parametric study is conducted to investigate the effects of these parameters on the flow dynamics. The Yih-type interfacial instabilities of sawtooth-like shape are observed at the interface separating the fluids. It is found that the displacement rate of the resident fluid decreases with increase in viscosity ratio. Although viscosity ratio has a non-monotonic effect on the velocity of the leading front, the velocity of the trailing front is found to be decreasing with increasing the viscosity ratio. Our results also predict the front velocity of the “lock-exchange flow” of two immiscible fluids in the exchange flow dominated regime which is consistent with the experiments of Séon *et al.* (2005). A single dimensionless parameter $\chi (\equiv 2Re \sin \theta / At Fr^2)$ is derived by balancing the buoyancy force in the axial direction with the imposed pressure force. Various flow regimes such as temporary back flow, stationary back flow and instantaneous displacement are identified based on χ . The critical value of χ for which transition of the exchanged flow regime to the displacement flow regime occurs agrees with the experimental finding of Taghavi *et al.* (2012). A linear stability analysis for a three-layer flow has been conducted and qualitative agreement is found with the results obtained from the lattice Boltzmann simulations.

(iii) Finally, in order to get the complete picture of the instabilities, the above study is extended to three-dimensions. A new screw-type instability is observed in the three-dimensional simulations. It is also shown that increasing angle of inclination increases the intensity of the instabilities. The effects of other parameters like Atwood number, Froude number and surface-tension parameter are observed to be qualitatively similar to those obtained in a two-dimensional channel.

Refereed Publications

1. “Multiphase lattice Boltzmann simulations of buoyancy-induced flow of two immiscible fluids with different viscosities”, P. R. Redapangu, S. P. Vanka and K. C. Sahu, *European J. Mechanics B/Fluids*, 34, 2012, 105-114.
2. “A study of pressure-driven displacement flow of two immiscible liquids using a multiphase lattice Boltzmann approach”, P. R. Redapangu, K. C. Sahu and S. P. Vanka, *Physics of Fluids*, 24, 2012, 102110.
3. “Lattice Boltzmann simulation of two immiscible liquids in a square duct”, P. R. Redapangu, K. C. Sahu and S. P. Vanka, *ASME Journal of Fluids Engineering*, 135, 2013, 121202.

Conference Paper

4. “Three dimensional lattice Boltzmann simulation of pressure-driven displacement flow of two immiscible fluids”, 21st International conference on Discrete Simulation of Fluid Dynamics, July 2012, Bangalore, India.
5. “A study of pressure-driven displacement flow of two immiscible liquids using a multiphase lattice Boltzmann approach”, 65th Annual fall DFD meeting, American Physical Society, Nov’ 2012, San Deigo.
6. “Interpenetration of two immiscible fluids in an oscillating channel using lattice Boltzmann method”, International congress on computational mechanics and simulations (ICCMS), Dec, 2012, IIT Hyderabad, India.
7. “Three dimensional simulation of buoyancy-induced mixing of two immiscible liquids”, National Conference on Parallel Computing Technologies (PARCOMPTECH), 2013, 21-23 Feb.
8. “Three-dimensional simulations of pressure-driven displacement flow of two immiscible liquids using a multiphase lattice Boltzmann approach”, 66th Annual fall DFD meeting, American Physical Society, Nov 24-26, 2013, Pittsburgh.

Some of the materials in this thesis are taken from the abovementioned papers, which I have published during my PhD.

Nomenclature

Roman Letters

L, H, W	:	length, height and width of the channel, respectively
h	:	height of the interface
f_α	:	index distribution function
g_α	:	pressure distribution function
e_α	:	lattice vector
w_α	:	weighing coefficient
c_s	:	velocity of sound
F_s	:	surface tension force
G	:	gravity force
g	:	acceleration due to gravity
a	:	strength of molecular interaction
a_c	:	critical value of Carnahan-Starling equation of state
p	:	pressure
R	:	gas constant
T	:	temperature
L/H	:	aspect ratio
m	:	viscosity ratio
Q	:	volumetric flow rate
Re	:	Reynolds number
At	:	Atwood number
Fr	:	Froude number
Ca	:	Capillary number
V_r, V_b	:	front velocities of heavier and lighter fluids, respectively
V_l, V_t	:	velocities of leading and trailing fronts, respectively
T_p	:	time period of oscillation
L_o, L_m	:	mixing lengths in non-oscillating and oscillating channels, respectively
L_o/L_m	:	normalised mixing length
c	:	phase speed of the disturbance

x, y, z	:	axial, wall normal and azimuthal coordinates, respectively
t	:	time
$\delta t, \delta x$:	time and space increments, respectively
i, j, k	:	index in the axial, wall normal and azimuthal directions, respectively
n_x, n_y, n_z	:	number of lattice points in the axial, wall normal and azimuthal directions, respectively
u, v, w	:	velocities in the axial, wall normal and azimuthal directions, respectively
$U_{wall}, V_{wall}, W_{wall}$:	wall velocities in the axial, wall normal and azimuthal directions, respectively

Greek Letters

α	:	lattice direction
θ	:	angle of inclination
θ_m	:	angle of inclination in oscillating channel
μ	:	viscosity
ν	:	kinematic viscosity
ρ	:	density
τ	:	relaxation time
ϕ	:	index function
ϕ_1, ϕ_2	:	minimum and maximum values of the index function, respectively
κ	:	magnitude of surface tension
σ	:	surface tension
ζ	:	direction normal to the interface
β	:	axial real wavenumber
ω	:	complex frequency
Φ	:	amplitude of the streamfunction
η	:	amplitude of the interfacial perturbation

Subscripts

α	:	lattice direction
1	:	properties of fluid 1
2	:	properties of fluid 2

Superscripts

eq	:	equilibrium
0	:	base state quantity
'	:	differentiation
^	:	disturbance quantity
-	:	averaged quantity

Abbreviations

<i>LGA</i>	:	lattice gas automata
<i>LGCA</i>	:	lattice gas cellular automata
<i>LBM</i>	:	lattice Boltzmann method
<i>LBE</i>	:	lattice Boltzmann equation
<i>BGK</i>	:	Bhatnagar-Gross-Krook
<i>N – S</i>	:	Navier-Stokes
<i>K – H</i>	:	Kelvin-Helmholtz
<i>C – S</i>	:	Carnahan-Starling
<i>GPU</i>	:	graphics processing unit
<i>CUDA</i>	:	compute unified device architecture
<i>D2Q7</i>	:	two-dimensional-seven-velocity
<i>D2Q9</i>	:	two-dimensional-nine-velocity
<i>D3Q15</i>	:	three-dimensional-fifteen-velocity
<i>D3Q19</i>	:	three-dimensional-nineteen-velocity
<i>D3Q27</i>	:	three-dimensional-twentyseven-velocity

List of Figures

1.1	Schematic diagram of a core-annular flow.	2
1.2	Schematic diagram of lock-exchange flow. H and L are the width and length of the channel, respectively. The partition is placed at $x = L/2$. g is the acceleration due to gravity. θ is the tilt angle measured with the horizontal. The density of fluid '1' is higher than that of fluid '2'.	4
1.3	Schematic showing the pressure-driven displacement of fluid '2' by fluid '1' in an inclined channel. θ is the angle of inclination, and g is the acceleration due to gravity. The viscosity and density of fluid '1' and '2' are μ_1, ρ_1 and μ_2, ρ_2 , respectively.	5
2.1	Lattice structures in two- and three-dimensional geometries.	13
2.2	Coexistence curve of ϕ [He <i>et al.</i> (1999b)]	14
2.3	Dependence of I on a [Zhang <i>et al.</i> (2000)].	15
2.4	Grid near the wall.	17
2.5	Thread hierarchy of GPU [Vanka <i>et al.</i> (2011)]	19
3.1	Schematic diagram of the initial equilibrium configuration of the system. Aspect ratio of the confined channel is 1 : 40.	24
3.2	(a) Spatio-temporal diagram of $\int_0^H \phi dy$ obtained using (a) 2562×66 (b) 3842×98 and (c) 5122×130 grid points. The slope of the white dashed lines represent the front velocities. The rest of the parameter values are $Re = 500$, $At = 0.05$, $m = 5$, $\kappa = 0.005$ and $\theta = 30^\circ$	25
3.3	Spatio-temporal evolutions of the density contours and velocity vector-fields for (a) $m = 0.1$, (b) $m = 1$ and (c) $m = 10$. The rest of the parameter values are $Re = 500$, $At = 0.05$, $\kappa = 0$ and $\theta = 60^\circ$	26
3.4	Evolution of the axial variation of the depth-averaged c (\bar{c}_x) and the transverse variation of the axial-averaged c (\bar{c}_y) for (a,b) $m = 0.1$, (c,d) $m = 1$ and (e,f) $m = 10$, respectively. The rest of the parameter values are $Re = 500$, $At = 0.05$, $\kappa = 0$ and $\theta = 60^\circ$	28

3.5	Effects of surface tension parameter (κ) on the density contours and velocity vector-fields at $t = 80$ for (a) $m = 0.1$, (b) $m = 1$ and (c) $m = 10$. The rest of the parameter values are $Re = 500$, $At = 0.05$ and $\theta = 60^\circ$	29
3.6	Effects of surface tension parameter (κ) on the axial variation of the depth-averaged c (\bar{c}_x) and the transverse variation of the axial-averaged c (\bar{c}_y) at $t = 80$ for (a,b) $m = 0.1$, (c,d) $m = 1$ and (e,f) $m = 10$, respectively. The rest of the parameter values are $Re = 500$, $At = 0.05$ and $\theta = 60^\circ$	30
3.7	Spatio-temporal evolutions of the density contours and velocity vector-fields for (a) $m = 0.1$, (b) $m = 1$ and (c) $m = 10$. The rest of the parameter values are $Re = 500$, $At = 0.05$, $\kappa = 0$ and $\theta = 30^\circ$	31
3.8	Evolution of the axial variation of the depth-averaged c (\bar{c}_x) and the transverse variation of the axial-averaged c (\bar{c}_y) for (a,b) $m = 0.1$, (c,d) $m = 1$ and (e,f) $m = 10$, respectively. The rest of the parameter values are $Re = 500$, $At = 0.05$, $\kappa = 0$ and $\theta = 30^\circ$	32
3.9	Effects of surface tension parameter (κ) on the density contours and velocity vector-fields at $t = 80$ for (a) $m = 0.1$, (b) $m = 1$ and (c) $m = 10$. The rest of the parameter values are $Re = 500$, $At = 0.05$ and $\theta = 30^\circ$	33
3.10	Effects of surface tension parameter (κ) on the axial variation of the depth-averaged c (\bar{c}_x) and the transverse variation of the axial-averaged c (\bar{c}_y) at $t = 80$ for (a,b) $m = 0.1$, (c,d) $m = 1$ and (e,f) $m = 10$, respectively. The rest of the parameter values are $Re = 500$, $At = 0.05$ and $\theta = 30^\circ$	34
3.11	Variation of the front velocity of the “blue” fluid, V_b with m for (a) $\theta = 60^\circ$ and (b) $\theta = 30^\circ$. The rest of the parameter values are $Re = 500$ and $At = 0.05$	35
3.12	Schematic diagram of the initial equilibrium configuration of the system. Aspect ratio of the confined channel is 1 : 32.	36
3.13	Evolution of the isosurface of ϕ at the interface at different times (from left to right: $t = 20, 40, 60, 80$ and 100). The parameters are $Re = 100$, $m = 1$, $At = 0.05$, $\kappa = 0$ and $\theta = 60^\circ$	36
3.14	Spatio-temporal evolution of the contours of the index function ϕ at different times in (a) x - y plane of the 3D channel, and (b) 2D channel. The parameters are the same as that of Fig.3.13.	37
4.1	Schematic showing the geometry (not to scale) and initial flow configuration. The inlet and outlet are located at $x = 0$ and $x = L$, respectively. The aspect ratio of the channel, L/H , is 48. Initially the channel is filled with fluids ‘1’ and ‘2’ from $0 \leq x \leq 5$ and $5 \leq x \leq L$ of the channel, respectively.	40
4.2	(a) Contour showing the penetrating finger and the leading and trailing fronts, (b) the spatio-temporal diagram of $\int_0^H \phi dy$ in time versus x plane showing the leading and the trailing front regimes. The plots are for a particular set of parameters.	41

4.3	(a) Variation of volume fraction of the displaced fluid (M_t/M_0) with time obtained using different mesh densities, and (b) the spatio-temporal diagram of $\int_0^H \phi dy$ in time versus x plane for $At = 0.2$, $m = 2$, $Fr = 2.236$, $Re = 100$, $Ca = 0.263$ and $\theta = 45^\circ$. The dotted line in panel (a) represents the analytical solution of the plug-flow displacement, given by $M_t/M_0 = 1 - tH/L$	42
4.4	Spatio-temporal evolution of the contours of the index function, ϕ for $At = 0.2$, $m = 2$, $Fr = 2.236$, $Re = 100$, $Ca = 0.263$ and $\theta = 45^\circ$	43
4.5	Variation of volume fraction of the displaced fluid (M_t/M_0) with time for different values of viscosity ratio, m for (a) $At = 0$ and $Fr = \infty$, and (b) $At = 0.3$, $Fr = 0.577$. The rest of the parameters are $Re = 100$, $Ca = 0.263$ and $\theta = 0^\circ$. The dotted lines in panels (a) and (b) represent the analytical solution of plug-flow displacement, given by $M_t/M_0 = 1 - tH/L$	44
4.6	Variations of velocities of (a) the leading (V_l) and (b) the trailing (V_t) fronts with viscosity ratio, m . The rest of the parameter values are $Re = 100$, $Ca = 0.263$ and $\theta = 0^\circ$	44
4.7	The contours of the index function, ϕ at $t = 15$ and $t = 50$ in a horizontal channel ($\theta = 0^\circ$) for two different values of viscosity ratio, m for (a) $At = 0$ and $Fr = \infty$ and (b) $At = 0.3$ and $Fr = 0.577$. The rest of the parameter values are $Re = 100$ and $Ca = 0.263$	45
4.8	The contours of the index function, ϕ at $t = 30$ for different inclination angles. The rest of the parameter values are $m = 10$, $At = 0.2$, $Fr = 1$, $Re = 100$ and $Ca = 0.263$	46
4.9	The effects of angle of inclination on the variation of the volume fraction of the displaced fluid, (M_t/M_0) with time. The parameters used are $m = 10$, $At = 0.2$, $Fr = 1$, $Re = 100$ and $Ca = 0.263$. The dotted line represents the analytical solutions of the variation of M_t/M_0 for plug-flow displacement, given by $M_t/M_0 = 1 - tH/L$	46
4.10	The spatio-temporal diagram of $\int_0^H \phi dy$ in time versus x plane for (a) $\theta = 0^\circ$, (b) $\theta = 5^\circ$, (c) $\theta = 60^\circ$ and (d) $\theta = 85^\circ$. The rest of the parameter values the same as those in Fig. 4.8.	47
4.11	The vorticity (first panel) and velocity vectors (second panel) fields for the same parameter values as those used to generate Fig. 4.8. The color-maps for the vorticity contours are shown as third panel.	48
4.12	Spatio-temporal evolution of contours of the index function, ϕ for (a) $m = 0.8$, (b) $m = 10$ and (c) $m = 30$. The rest of the parameters are $At = 0.2$, $Fr = 1$, $Re = 100$, $\theta = 45^\circ$ and $Ca = 0.263$	49
4.13	The spatio-temporal diagram of $\int_0^H \phi dy$ in time versus x plane for (a) $m = 0.8$, (b) $m = 10$ and (c) $m = 30$. The rest of the parameter values are the same as those used to generate Fig. 4.12.	50
4.14	Effects of viscosity ratio, m on variation of the volume fraction of the displaced fluid, (M_t/M_0) with time. The rest of the parameter values are the same as those used to generate Fig. 4.12. The dotted line represents the analytical solution for plug-flow displacement, given by $M_t/M_0 = 1 - tH/L$	50
4.15	The contours of the index function, ϕ for different values of capillary number at $t = 30$. The rest of the parameter values are $m = 5$, $At = 0.2$, $Fr = 1$, $Re = 100$ and $\theta = 45^\circ$	50

4.16	Variation of the normalized front velocity, FrV_l with Froude number, Fr for (a) $m = 1$ (b) $m = 10$. The rest of the parameter values are $Re = 100$, $Ca = 0.263$ and $\theta = 5^\circ$. The dashed line is the best fitted polynomial, given by $FrV_l = 0.38 + 0.665Fr + 0.3534Fr^2$. The red, blue and green square boxes in panel (a) correspond to $Fr = 0.604$, $Fr = 0.671$ and $Fr = 2.24$, respectively.	51
4.17	The spatio-temporal diagram of $\int_0^H \phi dy$ in time versus x plane for (a) $Fr = 0.604$, (b) $Fr = 0.671$ and (c) $Fr = 2.24$ for the parameters $At = 0.2$, $m = 1$, $Re = 100$, $\theta = 5^\circ$ and $Ca = 0.263$. The white dashed lines represent the initial location of the interface ($x = 5$).	52
4.18	Normalized front velocity as a function of normalized Fr, for (a) $m = 1$ and (b) $m = 10$ where $\chi = 2Re\sin\theta/AtFr^2$. The rest of the parameters are $Re = 100$, $\theta = 5^\circ$ and $Ca = 0.263$. The solid line represents the line $V_l = V_0$. The filled circle in (a) corresponds to $Fr = 0.671$, the squares to the left and the right of this filled circle correspond to $Fr = 0.604$ and $Fr = 2.24$, respectively.	52
4.19	Schematic showing the geometry and initial condition of the flow. Also shown here is profile of the steady, streamwise velocity component generated with $m = 10$ and $h^0 = 0.5$	53
4.20	Variation of (a) maximal growth rate, $\omega_{i,max}$ (a) axial wavenumber associated with the most dangerous mode, β_{max} with viscosity ratio, m . The rest of the parameter values are $Re = 100$, $At = 0.1$, $Fr = 1$, $\theta = 0^\circ$ and $Ca = 0.263$	55
4.21	Variation of (a) maximal growth rate, $\omega_{i,max}$ (a) axial wavenumber associated with the most dangerous mode, β_{max} with Atwood number At . The rest of the parameter values are $Re = 100$, $m = 10$, $Fr = 1$, $\theta = 0^\circ$ and $Ca = 0.263$	55
4.22	Variation of (a) maximal growth rate, $\omega_{i,max}$ (a) axial wavenumber associated with the most dangerous mode, β_{max} with Froude number, Fr . The rest of the parameter values are $Re = 100$, $m = 10$, $At = 0.1$, $\theta = 0^\circ$ and $Ca = 0.263$	56
4.23	Variation of (a) maximal growth rate, $\omega_{i,max}$ (a) axial wavenumber associated with the most dangerous mode, β_{max} with capillary number, Ca . The rest of the parameter values are $Re = 100$, $m = 10$, $At = 0.1$, $\theta = 0^\circ$ and $Fr = 1$	56
5.1	Schematic describing the geometry and the initial configuration. The inlet and outlet are located at $x = 0$ and $x = L$, respectively. The aspect ratio of the channel, L/H , is 32. Initially the channel portions from $0 \leq x \leq H/4$ and $H/4 \leq x \leq L$ are filled with liquid '1' and liquid '2', respectively.	60
5.2	Variation of mass fraction of the displaced liquid (M_t/M_0) with time for different grids. The rest of the parameters are $Re = 100$, $m = 10$, $At = 0.2$, $Fr = 5$, $\kappa = 0.005$ and $\theta = 45^\circ$. The dotted line represents the analytical solution of the plug-flow displacement, given by $M_t/M_0 = 1 - tH/L$	61
5.3	Contours of the index function, ϕ at (a) $t = 10$ and (b) $t = 30$ in the x - y plane at $z = W/2$ for different grids. The parameters are the same as those of Fig. 5.2	62

5.4	Evolution of the isosurface of ϕ at the interface at different times (from left to right: $t = 12, 18, 30$ and 50) for the simulation domain of $2112 \times 66 \times 66$ grid. The parameters are $Re = 100$, $m = 10$, $At = 0.2$, $Fr = 5$, $\kappa = 0.005$ and $\theta = 45^\circ$. The flow is in the positive x -direction.	62
5.5	Contours of the index function, ϕ at $t = 20$ in (a) x - y plane at $z = W/2$, and (b) x - z plane at $y = H/2$. The parameters are $Re = 100$, $At = 0.2$, $m = 10$, $Fr = 1$ and $\kappa = 0.005$	63
5.6	Contours of the index function, ϕ at $t = 20$ in the y - z plane at $x = L/2$. The parameters are $Re = 100$, $At = 0.2$, $m = 10$, $Fr = 1$ and $\kappa = 0.005$	64
5.7	Axial variation of normalized average viscosity, $\bar{\mu}_{yz} (\equiv \mu_{yz}/\mu_{yz}^0)$ for (a) $\theta = 30^\circ$ and (b) $\theta = 85^\circ$. The rest of the parameters are $Re = 100$, $At = 0.2$, $m = 10$, $Fr = 1$ and $\kappa = 0.005$. Here $\mu_{yz} = \frac{1}{HW} \int_0^W \int_0^H \mu dy dz$, and μ_{yz}^0 is the value of μ_{yz} at $x = 0$	64
5.8	Vertical variation of normalized average viscosity, $\bar{\mu}_{xz} (\equiv \mu_{xz}/\mu_{xz}^0)$ for (a) $\theta = 30^\circ$, and (b) $\theta = 85^\circ$. The rest of the parameters are the same as those used in Fig. 5.5. Here $\mu_{xz} = \frac{1}{LW} \int_0^W \int_0^L \mu dx dz$, and μ_{xz}^0 is the value of μ_{xz} at $y = 0$	65
5.9	Axial variation of normalized average viscosity, $\bar{\mu}_y (\equiv \mu_y/\mu_y^0)$, for (a) $\theta = 5^\circ$, (b) $\theta = 85^\circ$ in a two-dimensional channel. The rest of the parameters are the same as those used to generate Fig. 5.5. Here $\mu_y = \frac{1}{H} \int_0^H \mu dy$, and μ_y^0 is the value of μ_y at $x = 0$	65
5.10	Vertical variation of normalized average viscosity, $\bar{\mu}_x (\equiv \mu_x/\mu_x^0)$, for (a) $\theta = 5^\circ$, (b) $\theta = 85^\circ$ in a two-dimensional channel. The rest of the parameters are the same as those used to generate Fig. 5.5. Here $\mu_x = \frac{1}{L} \int_0^L \mu dx$, and μ_x^0 is the value of μ_x at $y = 0$	66
5.11	Spatio-temporal evolution of the contours of the index function, ϕ . (a) x - y plane at $z = W/2$ (three-dimensional simulation), and (b) the corresponding two-dimensional results. The parameters are $Re = 100$, $m = 20$, $At = 0.2$, $Fr = 5$, $\theta = 30^\circ$ and $\kappa = 0.005$	67
6.1	Schematic showing the geometry (not to scale) of the system.	69
6.2	Spatio-temporal evolution of density contours in a non-oscillating vertical channel. The simulation parameters are $At = 0.01$, $m = 1$, $Re = 500$, $\theta_m = 0^\circ$ and $\kappa = 0$	70
6.3	Spatio-temporal evolution of density contours in an oscillating channel with $T_p = 9600$. The simulation parameters are $At = 0.01$, $m = 1$, $Re = 500$, $\theta_m = 45^\circ$ and $\kappa = 0$	71
6.4	Evolution of the (a) axial variation of the depth-averaged c (\bar{c}_x) and (b) the transverse variation of the axially-averaged c (\bar{c}_y) in an oscillating channel with $T_p = 9600$. The rest of the parameter values are $At = 0.01$, $m = 1$, $Re = 500$, $\theta_m = 45^\circ$ and $\kappa = 0$	72
6.5	The effect of T_p on the normalized mixing length (L_m/L_0). The parameters are $At = 0.01$, $m = 1$, $Re = 500$, $\theta_m = 45^\circ$ and $\kappa = 0$	72
6.6	The temporal variation of mixing length in an oscillating channel (L_m) for various At and T_p . The parameters are $m = 1$, $Re = 500$, $\theta_m = 45^\circ$ and $\kappa = 0$	73

List of Tables

- 3.1 The velocities of the “red” (V_r) and “blue” (V_b) fingers for different grid densities. The rest of the parameter values are $Re = 500$, $At = 0.05$, $m = 5$, $\kappa = 0.005$ and $\theta = 30^\circ$ 25
- 4.1 The velocity of the leading (V_l) and trailing (V_t) fronts for different grid densities. The rest of the parameter values are $At = 0.2$, $m = 2$, $Fr = 2.236$, $Re = 100$, $Ca = 0.263$ and $\theta = 45^\circ$ 42

Contents

Acknowledgements	iii
Synopsis	v
Nomenclature	ix
List of Figures	xvii
List of Tables	xix
1 Introduction	1
1.1 Background	1
1.1.1 Miscible flow configuration	1
1.1.2 Immiscible flow configuration	2
1.2 Buoyancy-driven flow	3
1.3 Pressure-driven displacement flow	5
1.4 Lattice Boltzmann method	7
1.4.1 LBM approaches for multiphase flows	8
1.5 LBM on Graphics Processing Unit	9
1.6 Outline of the thesis	10
2 LBM Formulation	11
2.1 Numerical approach	12
2.2 Boundary conditions	17

2.3	GPU Implementation	18
2.3.1	GPU Architecture	18
2.3.2	GPU Programing	19
3	Buoyancy-driven flow	23
3.1	Problem definition	23
3.2	Results and discussion	24
3.3	Buoyancy driven flow in a three-dimensional inclined channel	35
3.4	Summary	38
4	Pressure-driven displacement flow	39
4.1	Problem description	39
4.2	Results and discussion	40
4.2.1	Grid independency test	40
4.2.2	Horizontal channel	43
4.2.3	Inclined channel	45
4.2.4	Near horizontal channel	51
4.3	Linear stability analysis	53
4.4	Summary	57
5	Pressure-driven displacement flow in a square duct	59
5.1	Problem description	59
5.2	Results and discussion	60
5.3	Summary	67
6	Other studies	69
6.1	Interpenetration of two immiscible fluids in an oscillating channel	69
6.1.1	Results and discussion	70
7	Conclusions	75

Appendices	77
I Derivation of Navier-Stokes equation from the Boltzmann equation	77
A Maxwell-Boltzmann equilibrium distribution function and some important identities . . .	77
A.1 Proof of Eq. (I.2)	78
A.2 Proof of Eq. (I.3)	78
A.3 Proof of Eq. (I.4)	79
A.4 Proof of Eq. (I.5)	80
A.5 Proof of Eq. (I.6)	81
B Moments of Maxwell-Boltzmann equilibrium distribution function	83
B.1 Zeroth moment of equilibrium distribution function	83
B.2 First moment of equilibrium distribution function	83
B.3 Second moment of equilibrium distribution function	83
B.4 Third moment of equilibrium distribution function	84
C Conservation of mass	84
D Conservation of momentum	85
Bibliography	91

CHAPTER 1

Introduction

1.1 Background

Multiphase flows of fluids having different fluid properties are common in many industrial processes, such as transportation of crude oil in pipelines [Joseph *et al.* (1997)], enhance oil recovery [Taghavi *et al.* (2012)], hydrology, filtration, coating, etc. In food processing industries, the cleaning of plants involves the removal of highly viscous fluid by fast flowing water stream injected at the inlet of the conduits [Regner *et al.* (2007)]. Multiphase systems can also be observed in many naturally occurring phenomena such as rain, snow, avalanches, clouds, underground water flows, sea waves, etc. Thus, many fascinating and counter-intuitive phenomena in multiphase fluid mechanics continue to be discovered despite the long fluid mechanics history in the areas, such as viscous fingering [Homsy (1987)], drop deformation [Clayton *et al.* (1998)] and electro-hydrodynamics [Melcher & Taylor (1969)]. A variety of situations were studied by considering the fluids to be immiscible (fluids separated by sharp interface, where the fluid properties undergoes a sudden jump) and miscible (where the flow dynamics is dominated by diffusion). A brief review of the literature conducted on these systems is given below. An extensive review of instabilities/flow dynamics in miscible and immiscible systems can also be found in Sahu & Govindarajan (2014).

1.1.1 Miscible flow configuration

A large number of studies have been conducted in various miscible configurations, such as three-layer and core-annular flows, displacement of one fluid by another fluid in channels, pipes, Hele-Shaw cells and porous media. In fact, the later one is extensively considered and the phenomenon known as viscous fingering, which occurs when a less viscous fluid displaces a more viscous one in porous media, has been investigated by several authors [see review by Homsy (1987)]. Hill *et al.* (1952) were the first to study viscous fingering phenomena in the context of packed columns. Hill *et al.* (1952), Homsy (1987) and also other researchers working in this area studied viscous fingering by considering isodensity fluids. The effects of density contrast in buoyancy-driven flow, wherein a highly dense fluid overlays a less dense one in a confined geometry, are investigated by several researchers experimentally [Séon *et al.* (2004), Séon *et al.* (2005), Séon *et al.* (2006a, 2007b)] and numerically [Grosfils *et al.* (2004), Goyal & Meiburg (2006), Hallez & Magnaudet (2008), Sahu & Vanka (2011)]. The effects of viscosity and density contrast are also studied in three-layer and core-annular flows (shown in Fig. 1.1) by several researchers [e.g., Ranganathan & Govindarajan (2001), Govindarajan (2004), Goyal *et al.* (2007), Sahu *et al.* (2009a), Selvam *et al.* (2009), Sahu & Govindarajan (2011)] by conducting linear stability analysis and analysing infinitesimally small perturbation. In a three-layer channel flow, Ranganathan & Govindarajan (2001) and Govindarajan (2004) showed that these flows are unstable at low Reynolds numbers and high Schmidt numbers. Ern *et al.* (2003) demonstrated the destabilizing effect of diffusion for continuous but rapidly varying viscosity stratification in a similar system.

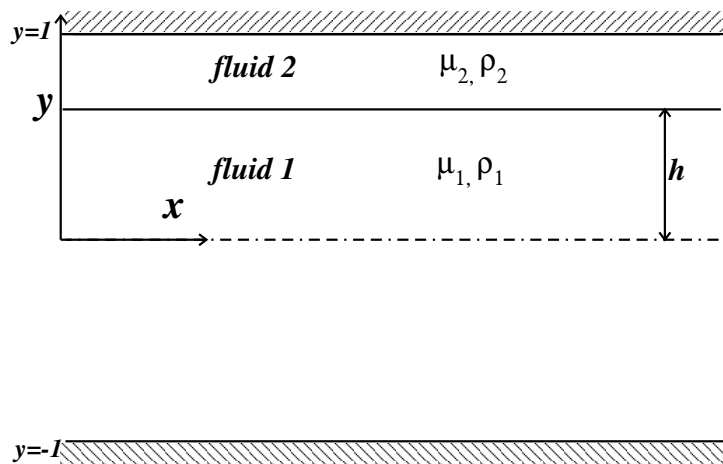


Figure 1.1: Schematic diagram of a core-annular flow.

Several authors [e.g. Taylor (1961), Cox (1962), Chen & Meiburg (1996), Petitjeans & Maxworthy (1996), Kuang *et al.* (2003)] experimentally studied core-annular miscible flows and focused on determining the thickness of the highly viscous fluid left on the pipe wall following its displacement by a less viscous fluid and on measuring the tip speed of the propagating finger of the less viscous fluid. In immiscible lubricated pipelining [Joseph *et al.* (1997)] and miscible three-layer channel flows [Govindarajan *et al.* (2001), Malik & Hooper (2005)], the flow is unstable if the annular fluid is more viscous than that of the fluid in the core of the channel/pipe. However, in the case of neutrally buoyant core-annular flow, Selvam *et al.* (2007) showed that beyond a critical viscosity ratio, the flow is unstable even when the less viscous fluid occupies near the wall. They also showed that axisymmetric (corkscrew) mode is unstable if the more (less) viscous fluid occupies the core of the pipe, for large Schmidt numbers, relatively small Reynolds number and large wave numbers.

1.1.2 Immiscible flow configuration

Many investigators have focused on the stability of immiscible fluids [Yih (1967), Hickox (1971), Joseph *et al.* (1984), Hu & Joseph (1989), Joseph *et al.* (1997), Kouris & Tsamopoulos (2001), Kouris & Tsamopoulos (2002) and references therein]. Starting with the work of Yih (1967) and Hickox (1971) carried out using long-wave theory in planar channel and cylindrical pipe, respectively, these studies have shown that two-layer flows are unstable due to interfacial mode at arbitrarily small Reynolds numbers. Yih (1967) used an asymptotic analysis to derive an expression for the complex wave speed as a function of the relevant system parameters, such as density, viscosity, and thickness ratios. He then demonstrated that instability exists due to an interfacial mode which results from the viscosity stratification even in the limit of vanishingly small Reynolds numbers. Yiantsios & Higgins (1988*b*) subsequently showed the appearance of a shear mode at sufficiently large Reynolds numbers, which corresponds to a short-wave Tollmien-Schlichting (TS) mode. Yiantsios & Higgins (1988*a*) also carried out an asymptotic analysis and extended the work of Yih (1967) to cover large wavenumbers and to account for the effects of gravity and interfacial tension using the perturbation scheme of Hooper & Boyd (1983); the latter authors examined the short-wave asymptotics of the interfacial instability between two unbounded viscous fluids. They provided predictions of critical Reynolds numbers for both the shear and interfacial modes and demonstrated the existence of discrepancies between these predictions and the experimental data of Kao & Park (1972). They also compared their results with the weakly nonlinear evolution of the interface

considered by Hooper & Grimshaw (1985).

Short-wave asymptotics were also carried out by Hooper & Boyd (1983), who showed that viscous stratification of two unbounded, immiscible fluids undergoing Couette flow leads to an unconditional instability in the absence of surface tension; the physical mechanism of this instability was elucidated by Hinch (1984). At sufficiently large Reynolds numbers, a short-wave, shear mode also becomes unstable [Yiantsios & Higgins (1988*b*)]. An extensive review of the work on the linear stability of planar two-fluid Poiseuille flow is provided by Boomkamp & Miesen (1996). A number of studies have also been carried out on the stability of immiscible core-annular flows in connection with lubricated oil pipelines and static mixers [Joseph *et al.* (1997)]. These studies have included linear stability analyses for horizontal [Joseph *et al.* (1984), Renardy & Joseph (1985), Hu & Joseph (1989), Preziosi *et al.* (1989), Hu *et al.* (1990), Sahu *et al.* (2007)] and vertical pipes [Hickox (1971), Hu & Patankar (1995)] accounting for viscosity and density contrasts, experiments [Charles *et al.* (1961), Bai *et al.* (1992)] and numerical simulations in straight [Li & Renardy (1999), Kouris & Tsamopoulos (2001), Kouris & Tsamopoulos (2002)] and corrugated pipes [Wei & Rumschitzki (2002*a*), Wei & Rumschitzki (2002*b*), Cao *et al.* (2003)].

The linear instability of two-dimensional disturbance in pressure-driven two-layer channel flow was studied by Sahu *et al.* (2007), wherein a Newtonian fluid layer overlies a layer of a Herschel-Bulkley fluid. The results of their study indicate a destabilizing effect by increasing the yield stress, prior to the formation of unyielded zones. An energy analysis was also conducted to study the mechanism of this instability. Frigaard (2001) studied two-dimensional linear stability of two-layer Poiseuille flow of two Bingham fluids in which only a fraction of the Bingham fluid has yielded. Their study involves an unyielded region between the Newtonian fluid and the yielded part of the Bingham fluid unlike in the study of Sahu *et al.* (2007). Interfacial waves would not develop under such conditions; this suppression of interfacial modes then leads to superstable two-layer flows [Frigaard (2001), Nouar *et al.* (2007)], similar to single-fluid pressure-driven flows. The effects of three-dimensional disturbances on the interfacial mode in the linear regime was also investigated by Sahu & Matar (2010). They found that three-dimensional disturbances are more unstable than two-dimensional disturbances, which arises a question on the application of Squire's theorem [Squire (1933)] on the interfacial flows.

Next, the literatures directly relevant to the present study are discussed. Two typical configurations, namely:

1. Buoyancy-driven flow
2. Pressure-driven displacement of one fluid by another fluid

are considered in this thesis.

1.2 Buoyancy-driven flow

A flow problem of considerable industrial and natural importance is the interpenetration of two immiscible fluids initially separated by a partition in a confined inclined channel and suddenly allowed to mix by the action of the gravitational force [Benjamin (1968), Joseph *et al.* (1997), Debacq *et al.* (2003), Ding *et al.* (2007)]. This problem is frequently referred to as the lock-exchange problem [Séon *et al.* (2004), Séon *et al.* (2007*a,b*), Hallez & Magnaudet (2008)], schematic of this configuration is shown in Fig. 1.2. This phenomenon plays an important role in the design of chemical and petroleum engineering

processes [Benjamin (1968), Joseph *et al.* (1997)] as well as for the understanding of various natural systems in oceanography and atmospheric sciences [Baird *et al.* (1992)]. In the absence of pressure-gradient, buoyancy-induced mixing has been previously studied experimentally by Séon *et al.* (2004, 2005), Séon *et al.* (2006a,b) and numerically by Hallez & Magnaudet (2008) and Sahu & Vanka (2011).

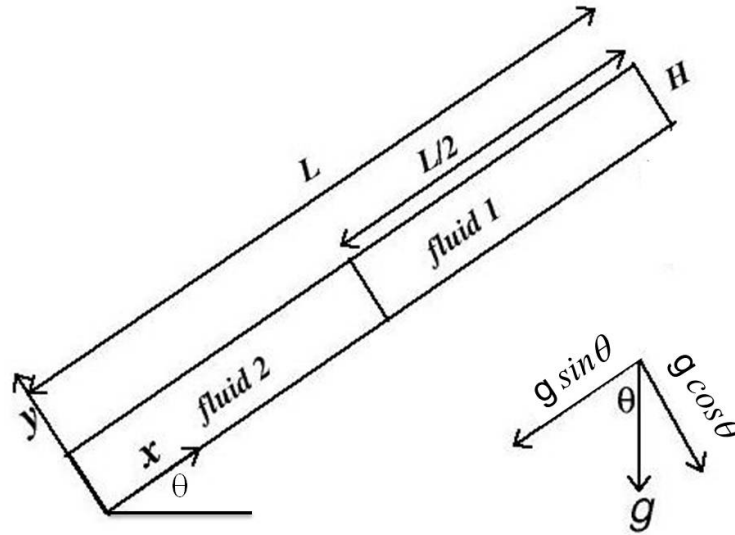


Figure 1.2: Schematic diagram of lock-exchange flow. H and L are the width and length of the channel, respectively. The partition is placed at $x = L/2$. g is the acceleration due to gravity. θ is the tilt angle measured with the horizontal. The density of fluid ‘1’ is higher than that of fluid ‘2’.

In the experiments of Séon *et al.* (2005), three distinct regions of the flow and mixing patterns were observed as the tilt angle was increased. For smaller tilt angles ($\theta < 65^\circ$, θ is the angle with vertical), the velocity of the high and low density fluids (moving in the opposite directions) increased linearly as the tilt angle was increased. The mixing (or interpenetration) of the two fluids could be characterized by a diffusive process described by a diffusion equation with a suitably defined diffusion coefficient. The flow and mixing are influenced by two distinct processes. First, the component of gravitational force along the axis of the channel accelerates the two fluids into each other at comparable velocities depending on the individual densities of the fluids. The interface of the two fluids becomes unstable and gives rise to the Kelvin-Helmholtz (KH) instabilities, and consequent transverse mixing. However, the component of the gravitational force normal to the channel axis has an opposite effect by acting to segregate the two fluids. The front velocity depends on the local density contrast across the interface, which in turn is decreased from the initial maximum value because of diffusional mixing (smearing) of the interface. Thus, while the KH instabilities decrease the front velocity, the segregation of the two fluids caused by the transverse gravitational force increases the front velocity. For $65^\circ < \theta < 82^\circ$, the flow is characterized by a regime in which the front velocity is nearly constant, with a value approximately $0.7 \sqrt{Atgd}$, where g is the gravitational acceleration and d is a characteristic dimension of the confining channel. The region of constant front velocity depends on the fluid viscosity (for a given Atwood number) with a higher fluid viscosity causing an earlier transition to the constant front velocity limit. This is a result of decreased small scale transverse mixing due to lower Reynolds number. When the pipe is almost horizontal ($\theta > 82^\circ$) the flow transitions to a third region in which the two fluids move as counter-current Poiseuille flows and the front velocity is then determined by the balance between buoyancy and wall friction. In this region, the velocity decreases with tilt angle because of the reduced buoyancy force.

Only a limited number of computational studies have been reported for this flow. Hallez & Mag-

naudet (2008) solved the governing equations with a finite volume method and studied the buoyancy-induced mixing of two fluids in circular, rectangular and square geometries. They found that the vortices which develop during the flow are more coherent and persistent in two than in three dimensional channel. Consequently, the vortices give rise to more intense mixing and long-lasting flow structures in two-dimensional than in three dimensional geometries. Recently, Sahu & Vanka (2011) used a two-phase lattice Boltzmann method (LBM) to simulate the interpenetration of two immiscible fluids in a tilted channel. They investigated the effects of Atwood number, Reynolds number, tilt angle and surface tension in terms of flow structures, front velocities and velocity profiles. They compared the result of a typical case with that of a finite volume method using the diffuse interface technique [Ding *et al.* (2007)] and found good agreement. Their results also compared well with the previous experimental results [Debacq *et al.* (2003), Séon *et al.* (2004, 2005)]. Recently, the study of Sahu & Vanka (2011) is extended to multicomponent systems by Lee & Kim (2013), where more than two fluids are allowed to mix inside a two-dimensional channel.

1.3 Pressure-driven displacement flow

The pressure-driven displacement flow of one fluid by another fluid is also common in many industrial processes, such as transportation of crude oil in pipelines [Joseph *et al.* (1997)], oil recovery, food-processing, coating, etc. The cleaning of plants also involves removal of viscous fluids by fast-flowing water streams [Regner *et al.* (2007)]. In enhanced oil recovery, hydrocarbon solvent or supercritical carbon dioxide is used to displace oil from an oil reservoir.

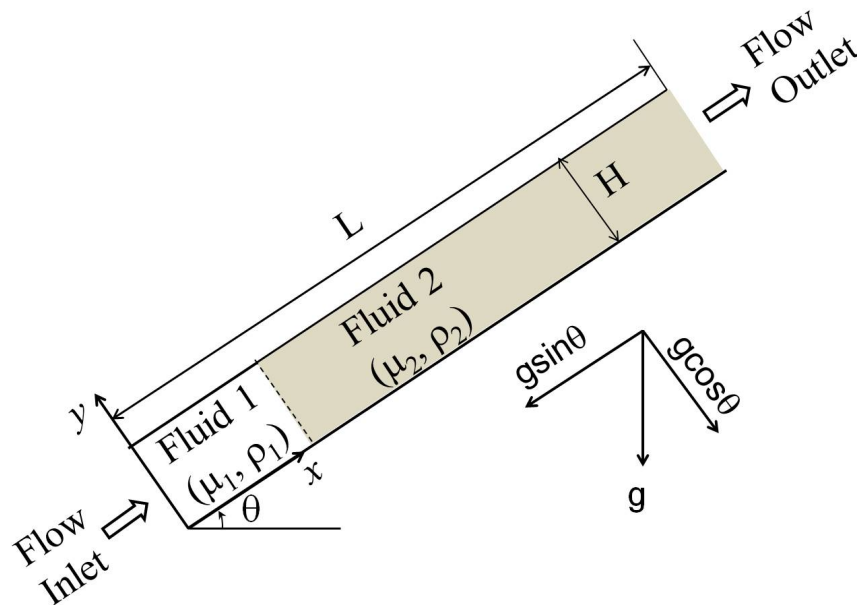


Figure 1.3: Schematic showing the pressure-driven displacement of fluid ‘2’ by fluid ‘1’ in an inclined channel. θ is the angle of inclination, and g is the acceleration due to gravity. The viscosity and density of fluid ‘1’ and ‘2’ are μ_1, ρ_1 and μ_2, ρ_2 , respectively.

The schematic of pressure-driven displacement of one fluid by another is shown in Fig. 1.3. When

a less viscous fluid displaces a more viscous one (i.e. $\mu_1 < \mu_2$) a two-layer/core-annular flow is obtained in most part of the channel/pipe as the elongated ‘finger’ of the less viscous fluid penetrates into the bulk of the more viscous one [Sahu *et al.* (2009a)]. The interface between the two fluids becomes unstable forming Yih-type instability in immiscible [Yih (1967)] and Kelvin-Helmholtz (KH) type instabilities and “roll-up” structures in miscible flows. A review of the phenomenon occurring in porous media (commonly known as viscous fingering) can be found in Homsy (1987). In pressure-driven two-layer/core-annular flows several authors have conducted linear stability analyses by considering the fluids to be immiscible [Yih (1967), Yiantsios & Higgins (1988b), Sahu *et al.* (2007), Sahu & Matar (2010)] and miscible [Govindarajan (2004), Malik & Hooper (2005), Selvam *et al.* (2007), Sahu *et al.* (2009a), Sahu & Govindarajan (2011)]. This problem was also studied by many researchers experimentally [Charles *et al.* (1961), Bai *et al.* (1992)] and numerically [Li & Renardy (1999), Kouris & Tsamopoulos (2001, 2002), Wei & Rumschitzki (2002b)]. In miscible core-annular flows, the thickness of the more viscous fluid layer left on the pipe walls and the speed of the propagating ‘finger’ were experimentally investigated by many authors [Taylor (1961), Cox (1962), Petitjeans & Maxworthy (1996), Chen & Meiburg (1996), Kuang *et al.* (2003)] and the axisymmetric and “corkscrew” patterns were found [Lajeunesse *et al.* (1997), Lajeunesse *et al.* (1999), Scoffoni *et al.* (2001), Gabard & Hulin (2003), Cao *et al.* (2003)]. In neutrally-buoyant core-annular pipe flows, d’Olce *et al.* (2008) observed axisymmetric “pearl” and “mushroom” patterns at high Schmidt number. By an asymptotic analysis, Yang & Yortsos (1997) studied miscible displacement flow between parallel plates and in cylindrical capillary tube with large aspect ratio in the Stokes regime. They investigated viscous fingering instability for large viscosity ratio and found that the displacement efficiency decreases with increasing viscosity ratio. Goyal *et al.* (2007) studied miscible displacement flows in a vertical Hele-Shaw cell with less-viscous fluid displacing a more-viscous one. They found that the flow develops as a result of linear instability, and the front velocity increases with increasing unstable density stratification and decreasing diffusion. The flow fields are qualitatively similar to those observed in the experiment of Petitjeans & Maxworthy (1996) in a capillary tube and in the theoretical predictions of Lajeunesse *et al.* (1999) in Hele-Shaw cells.

Sahu *et al.* (2009b) studied pressure-driven miscible displacement flow in an inclined channel via numerical solution of the Navier-Stokes equations coupled to a convective-diffusion equation for the concentration of the more viscous fluid. The viscosity and density are assumed to be function of the concentration of the more viscous fluid. The effects of density ratio, Froude number, and channel inclination were investigated. Their results demonstrated that the rate of mixing and displacement of the more viscous fluid are promoted by the development of KH-type instabilities, and enhanced with increasing density ratio and Froude number. The mixing rates were also shown to increase with increasing inclination angles when the displaced fluid is also the denser one. Recently, Taghavi *et al.* (2010, 2011) studied the effects of imposed mean flow on a buoyant exchange flow of two miscible fluids in a near horizontal pipe. For very low imposed velocity, they observed an inertial gravity current and KH like instabilities in the interfacial region separating the fluids. The flow becomes stable for higher imposed flow with the absence of KH instabilities and consequent decreased mixing. This behavior is counterintuitive since more energy is injected into the system as the imposed flow is increased. Non-Newtonian effects on miscible displacement flows in vertical narrow eccentric annuli were experimentally studied by Mohammadi *et al.* (2010). They demonstrated that suitable choice of viscosity ratio, density ratio and flow rate results in steady displacement flows. In case of steady flow, they observed that eccentricity drives a strong azimuthal counter-current flow above/below the interface resulting in an advancing spike.

As the above brief review shows, inspite of the large volume of research on the miscible displacement flows, very few studies have been conducted for the displacement flow in immiscible systems. The flow dynamics in immiscible flows are very different from those of the miscible flows due to the presence

of a sharp interface separating the fluids and are associated with interfacial tension. On the other hand, miscible flows are associated with diffusion. Selvam *et al.* (2007) compared the stability of immiscible flows (with zero surface tension) with miscible flows and found that miscible flows are stable for any Reynolds number when the viscosity ratio is less than a critical value, unlike the immiscible flows with zero surface tension, which can be unstable for any Reynolds number for any arbitrarily small viscosity gradient. Also in miscible flows the width of the interfacial region increases with time even when the diffusion coefficient is very small (this rate is proportional to the inverse of Peclet number), which in turn stabilizes the flow [see Hickox (1971); Selvam *et al.* (2007)].

Most numerical studies of displacement flows solved the continuum Navier-Stokes equations using a finite volume/element/spectral method. The lattice Boltzmann method (LBM) is an alternative to solve the Navier-Stokes equations for study of fluid flows. Also very high computational power is necessary to simulate interfacial flows as fine grids and long domains are required for accurate simulation of the interfacial dynamics. LBM could be ideal for studying the interfacial flows because of its low computational cost and its ability to track the interface automatically. The displacement flows of two immiscible liquids were studied by Chin *et al.* (2002), Grosfils *et al.* (2004), Kang *et al.* (2004) and Dong *et al.* (2010) via lattice Boltzmann method. The effects of wettability, surface tension, viscosity ratio and gravity have been included sequentially. Although the recent study of Dong *et al.* (2010) considered all these parameters, the formation of the interfacial instabilities, which are the important characteristics of such flows, was not reported by any of the previous studies. This may be due to the low Reynolds number and smaller computational domain considered in the earlier studies.

In the present thesis, lattice Boltzmann method is used to study the flow dynamics in buoyancy-driven and pressure-driven displacement flows which are discussed in Chapters 3 and 4, respectively. Below, a brief overview of lattice Boltzmann method for multiphase flows is provided.

1.4 Lattice Boltzmann method

Lattice Boltzmann method is originated from lattice gas cellular automata (LGCA) or simply lattice gas automata (LGA). Detailed theory of LGCA can be found in Rothman & Zaleski (1997) and Rivet & Boon (2000). The lattice Boltzmann method (LBM) is the simplified form of lattice-gas automata. This is a mesoscopic model that has its origin in the kinetic theory. The LBM solves discrete density distribution functions and obtains the velocities and density as moments of this distribution function. In comparison with solution of the Navier-Stokes equations, LBM is a simple, efficient and easily parallelizable technique. It involves only three basic steps: (a) collision; (b) streaming; and (c) calculation of the flow variables. It can include mesoscopic flow physics such as velocity slip, surface tension force, and other inter-molecular forces. Chen & Doolen (1998) provide a detailed review of lattice Boltzmann method and the Chapman-Enskog procedure which is used to show that the LBM equations approximately resemble Navier-Stokes equations in compressible form.

The boolean variables in lattice gas automata are replaced by discrete distribution functions in lattice Boltzmann equation (LBE) and the collision rule is replaced by a continuous function called collision operator. The computational domain in the LBM contains a regular lattice of sites on which a set of particle distribution functions can be computed. Each of the particle distribution function is associated with a specific lattice vector. At each time, two steps, collision and streaming takes place. In the collision step, the distribution functions arriving at a node interact and change their velocity directions according to scattering rules. In the streaming step, each distribution function moves to the neighbouring node along

the direction of velocity. If two distribution functions arrive at the same point, they are redistributed so as to conserve mass and momentum.

General form of the lattice Boltzmann equation can be written as:

$$f_\alpha(\mathbf{x} + \mathbf{e}_\alpha \delta t, t + \delta t) = f_\alpha(\mathbf{x}, t) + \Omega_\alpha(\mathbf{x}, t), \quad (1.1)$$

where f_α is the distribution function along the α^{th} lattice direction; the number of lattice directions depends on the lattice. \mathbf{x} is the position vector and \mathbf{e}_α is the lattice vector. $\Omega_\alpha = \Omega_\alpha(\mathbf{x}, t)$ is the collision operator which represents the rate of change of f_α resulting from collision. δt and $\delta \mathbf{x}$ correspond to time and space increments, respectively.

A simplification in the LBM is to approximate the collision operator with the Bhatnagar-Gross-Krook (BGK) relaxation term [Bhatnagar *et al.* (1954), Qian *et al.* (1992)], given by

$$\Omega_\alpha(\mathbf{x}, t) = -\frac{f_\alpha(\mathbf{x}, t) - f_\alpha(\mathbf{x}, t)^{eq}}{\tau}, \quad (1.2)$$

where τ is the relaxation time which is related to viscosity as $\nu = (\tau - 1/2)\delta t c_s^2$, wherein c_s is the velocity of sound. f_α^{eq} is the equilibrium distribution function along the α^{th} lattice direction.

Substituting Eq. 1.2 in Eq. 1.1, one gets the LBM equation with the BGK approximation:

$$f_\alpha(\mathbf{x} + \mathbf{e}_\alpha \delta t, t + \delta t) = f_\alpha(\mathbf{x}, t) - \frac{f_\alpha(\mathbf{x}, t) - f_\alpha(\mathbf{x}, t)^{eq}}{\tau}. \quad (1.3)$$

The density and the momentum density are defined as the moments of the distribution function, f_α as:

$$\rho = \sum f_\alpha \quad \text{and} \quad \rho \mathbf{u} = \sum f_\alpha \mathbf{e}_\alpha. \quad (1.4)$$

1.4.1 LBM approaches for multiphase flows

The LBM equations discussed above are for single phase systems. These are modified by many researchers for multiphase flows. Mainly, there are four different LBM approaches for multiphase flows: (i) the color segregation method [Gunstensen *et al.* (1991)], (ii) method of Shan and Chen [Shan & Chen (1993a); Shan & Doolen (1995)], (iii) free energy approach [Swift *et al.* (1995)] and (iv) the method of He and co-workers [He *et al.* (1999b)]. An extensive review of the work on the first three approaches can be found in Chen & Doolen (1998). A brief overview of these multiphase LBM approaches is presented below.

Color segregation method:

Gunstensen *et al.* (1991) proposed the first LBM approach for immiscible fluids. This method is also called the ‘‘color segregation method’’. In this approach, the particles are colored either red or blue and the collision rules for both phases are modified to obtain surface tension between the two fluids. These collision rules send particles of one color to the neighbouring sites containing other particles of the same color. A perturbation is first added to the particle distribution near an interface. This creates an appropriate surface tension dynamics. In the second step, the mass is recolored to achieve zero diffusivity of one color into the other. Grunau *et al.* (1993) later introduced density and viscosity variations to this

model. However, the color segregation method has some drawbacks like the time consuming color redistribution step, distribution functions causing anisotropic surface tension, etc.

Method of Shan and Chen:

Shan & Chen (1993a) and Shan & Doolen (1995) developed a lattice Boltzmann model that has the capability of simulating multiphase and multi-component immiscible fluids with different densities at constant temperature. This model uses the concept of microscopic interactions to modify the surface tension related collision operator. The model introduces an interparticle potential to account for phase segregation and surface tension. Separation of the phases takes place automatically. The model is suitable for high density contrast, but has difficulty to handle the systems with high viscosity contrast.

Free energy model:

Swift *et al.* (1996, 1995) modified to the above models by defining the equilibrium distributions based on thermodynamics. This model introduces Helmholtz free energy to represent the equation of state of the system. This feature enables the conservation of total energy in the system including surface energy, kinetic energy and internal energy. The method is useful in the systems having variable surface tension, such as thermo-capillary motion.

Method of He and co-workers:

He and co-workers [He *et al.* (1999a,b); Zhang *et al.* (2000)] developed a multiphase lattice Boltzmann model that uses an index fluid to track the interface between the phases. It uses molecular interactions to account for interfacial dynamics and phase segregation. Strong molecular attractions make the index fluid to separate into different phases automatically. A sharp interface can be maintained throughout the simulation and surface tension is also naturally incorporated in the model. Sahu & Vanka (2011) modified this approach to study the buoyancy-driven interpenetration of two immiscible fluids having different viscosities. This method has been used in the present thesis, and discussed in detail in the next chapter.

1.5 LBM on Graphics Processing Unit

Graphics processing unit (GPU) is a new paradigm for computing fluid flows and has become more popular in the recent years. It is a powerful tool for performing parallel computations. It can be thought as a massively parallel computer that is capable of executing instructions, simultaneously on a large number of arithmetic units. The GPU is designed in such a way that it yields very high computational power. The LBM, which itself is a faster and reliable technique for fluid flow simulation, when implemented on GPU gives a very high computational speed-up. The high performance computing and low energy consumption have made GPU more beneficial. Detailed report on GPU architecture and implementation is also presented in Chapter 2.

Several researchers have implemented LBM on GPUs. Li *et al.* (2005) implemented single phase LBM on GPU with Cg and OpenGL as programming model on NVIDIA GeForce FX 5900 Ultra GPU. They achieved 8-15 times speed up than the CPU counterpart. Tolke (2008) implemented two-phase LBM on GPU using CUDA for simulation of flow through porous media. They reported 10 times speed up over the corresponding CPU program. Peng *et al.* (2008) implemented three-dimensional lattice

Boltzmann method on a GPU using CUDA and observed 8.67 times speed-up. The differences in speed-up are mainly caused due to various properties like the CPU compiler, hardware and also the type of CPU core. The GPU based LBM algorithm developed in our research group gives 25 times speed up over the corresponding CPU based code [Sahu & Vanka (2011)]. The same code has been used in the present work.

1.6 Outline of the thesis

In this thesis, the numerical simulation of two immiscible fluids is conducted using a multiphase lattice Boltzmann method. The instability patterns arise in the flow due to a imposed pressure-gradient and gravity have been investigated. A brief background, relevant applications, and a extensive literature survey on the problems considered are discussed in this chapter. The rest of the thesis is organised as follows:

The mathematical formulation of the current multiphase lattice Boltzmann method (LBM) is discussed in Chapter 2. The LBM approaches used for both the two and three-dimensional geometries are discussed. The implementation of the LBM on graphics processing unit (GPU) is also presented in this chapter.

In Chapter 3, the buoyancy-driven flow of two immiscible fluids with different viscosities and densities in a confined tilted channel is presented. The effects of viscosity differential on the flow structures and front velocities are examined. The main findings of this study are as follows. Relatively stable fingers are observed for high viscosity ratios. The intensity of the interfacial instabilities and the transverse interpenetration of the fluids increase with decreasing viscosity differential of the fluids.

Chapter 4 focuses on the study of pressure-driven displacement of two immiscible fluids. A systematic parametric study is conducted to investigate the effects of various dimensionless numbers, such as viscosity ratio, Atwood number, Froude number and surface tension. The effects of angle of inclination on the flow dynamics are also investigated. The results are then compared with the experimental results of Taghavi *et al.* (2012). A three-dimensional extension of this problem is provided in Chapter 5. A two-dimensional-nine velocity ($D2Q9$) lattice model is used in the two-dimensional flow problems, whereas, a three-dimensional-fifteen-velocity ($D3Q15$) lattice model is used in order to simulate the flow in three-dimensions. The effects of channel inclination, viscosity and density contrasts are investigated. The contours of the density and the average viscosity profiles in different planes are plotted and compared with those obtained in a two dimensional channel.

Some other studies which are in the preliminary stage are described in Chapter 6. These include the interpenetration of two immiscible liquids in an oscillating channel, and three-dimensional extension of buoyancy-driven flow of two immiscible liquids in an inclined channel.

Finally, the whole study presented in this thesis is summarised and concluded in Chapter 7.

CHAPTER 2

LBM Formulation

Many numerical methods have been developed in last few decades for solving fluid flow problems. Most of these are based on solving the continuum Navier-Stokes and continuity equations using finite volume/element/spectral methods. In conventional approaches the governing partial-differential equations are discretized in space and time and solved. Depending on the numerical scheme used, an explicit or iterative procedure has been used to update velocities and pressure. For incompressible flows, typically a pressure-Poisson equation is solved iteratively to obtain the pressure field that provides a divergence-free velocity field [Chorin (1967)]. In such methods, the solution of the pressure-Poisson equation is the most time consuming step and requires a large number of iterations to reach a good degree of convergence. In multiphase flows, in addition to the momentum and continuity equations, a concentration transport equation must be solved with an accurate front capturing technique [Ding *et al.* (2007)].

An alternative approach of solving the Navier-Stokes equations is the lattice Boltzmann method (LBM) [Chen & Doolen (1998)] which is a mesoscopic model whose origin is in kinetic theory. The LBM solves discrete density distribution functions and obtains the velocities and density as moments of this distribution function. It is a simple and elegant method that has rapidly evolved as an alternative multi-scale model of fluid flows [Shui *et al.* (2007), Li & Tafti (2009)]. In comparison with solution of the Navier-Stokes equations, LBM is a simple, efficient and easily parallelizable technique. It involves only three basic steps: (a) collision; (b) streaming; and (c) calculation of the flow variables. It can include mesoscopic flow physics such as velocity slip, surface tension forces, and other inter-molecular forces. The LBM has also been extended to simulate multiple phases by the use of multiple distribution functions [Gunstensen *et al.* (1991), Shan & Chen (1993*a,b*), Shan & Doolen (1995), Swift *et al.* (1995), Swift *et al.* (1996), Rakotomalala *et al.* (1997), He *et al.* (1999*a,b*), Zhang *et al.* (2000), Latva-Kokko & Rothman (2005), Lee & Lin (2005), Lishchuk *et al.* (2008), Wu *et al.* (2008*a,b*), Li & Tafti (2009)]. For multiphase flows, intermolecular forces are introduced to make the phases attract and repel each other as required. Four distinctly different LBM approaches for multiphase flows, namely, the color segregation method of Gunstensen *et al.* (1991), method of Shan and Chen [Shan & Chen (1993*a*); Shan & Doolen (1995)], free energy approach [Swift *et al.* (1995), Swift *et al.* (1996), Li & Tafti (2009)] and method of He and co-workers [He *et al.* (1999*a,b*); Zhang *et al.* (2000)] have been proposed and applied to a number of flows. These methods are discussed in Chapter 1.

This chapter describes the approach suggested by He and co-workers [He *et al.* (1999*a,b*); Zhang *et al.* (2000)] which has been used in simulating all the multiphase flow problems reported in this thesis. In order to increase the computational efficiency, the present LBM algorithm has been implemented on Graphics Processing Unit (GPU), which is discussed at the end of this chapter.

2.1 Numerical approach

The numerical approach used in this thesis is similar to the two-phase lattice Boltzmann method previously proposed by He and co-workers [Zhang *et al.* (2000)], and used in the recent study of Sahu & Vanka (2011). The LBM simulates fluid flow problems using discrete distribution functions. In this method, two distribution functions (index distribution function (f) and the pressure distribution function (g)) are used to track the interface and to calculate the macroscopic properties of the fluids.

The evolution equations for the index distribution function (f) and the pressure distribution function (g) are given by:

$$f_\alpha(\mathbf{x} + \mathbf{e}_\alpha \delta t, t + \delta t) - f_\alpha(\mathbf{x}, t) = -\frac{f_\alpha(\mathbf{x}, t) - f_\alpha^{\text{eq}}(\mathbf{x}, t)}{\tau} - \frac{2\tau - 1}{2\tau} \frac{(\mathbf{e}_\alpha - \mathbf{u}) \cdot \nabla \psi(\phi)}{c_s^2} \Gamma_\alpha(\mathbf{u}) \delta t, \quad (2.1)$$

$$g_\alpha(\mathbf{x} + \mathbf{e}_\alpha \delta t, t + \delta t) - g_\alpha(\mathbf{x}, t) = -\frac{g_\alpha(\mathbf{x}, t) - g_\alpha^{\text{eq}}(\mathbf{x}, t)}{\tau} + \frac{2\tau - 1}{2\tau} (\mathbf{e}_\alpha - \mathbf{u}) \cdot \left[\Gamma_\alpha(\mathbf{u}) (F_s + \mathbf{G}) - (\Gamma_\alpha(\mathbf{u}) - \Gamma_\alpha(0)) \nabla \psi(\rho) \right] \delta t. \quad (2.2)$$

In the above equations the left hand side terms represent the advection of the distribution functions on the lattice by the unit vectors. The first term on the right hand side of Eqs. (2.1) and (2.2) represents the collision of the distribution functions with its equilibrium values and a time constant. The last term in Eqs. (2.1) and (2.2) represents the molecular interaction and a deviation from the ideal gas law, respectively. Here \mathbf{u} represents the velocity field; for two-dimensional flows, $\mathbf{u} = (u, v)$ and for three-dimensional flows $\mathbf{u} = (u, v, w)$, where u , v and w denote the velocity components in the streamwise, x , wall-normal, y and spanwise, z , directions, respectively. δt is the time step; τ is the single relaxation time using the Bhatnagar-Gross-Krook (BGK) model [Bhatnagar *et al.* (1954)]. The kinematic viscosity, ν is related to the relaxation time by the expression, $\nu = (\tau - 1/2)\delta t c_s^2$. α is the lattice direction which depend on the lattice model one uses. Various lattice models used in two-dimensional geometries are *D2Q7* (two-dimensional-seven-velocity) and *D2Q9* (two-dimensional-nine-velocity). Similarly for simulating flows in three-dimensional geometries, *D3Q15* (three-dimensional-fifteen-velocity), *D3Q19* (three-dimensional-nineteen-velocity) and *D3Q27* (three-dimensional-twentyseven-velocity) lattice models are widely used. All the simulations presented in this thesis are based on *D2Q9* lattice model for two-dimensional geometries and *D3Q15* for three-dimensional geometries. The structure of these lattices are shown in Fig. 2.1.

In *D2Q9* lattice, the lattice velocities (\mathbf{e}_α) and the weighing coefficients (w_α) are given by:

$$\mathbf{e}_\alpha = \begin{cases} 0, & \alpha = 1, \\ \left[\cos\left(\frac{(\alpha-1)\pi}{2}\right), \sin\left(\frac{(\alpha-1)\pi}{2}\right) \right], & \alpha = 2, 3, 4, 5, \\ \sqrt{2} \left[\cos\left(\frac{(\alpha-5)\pi}{2} + \frac{\pi}{4}\right), \sin\left(\frac{(\alpha-5)\pi}{2} + \frac{\pi}{4}\right) \right], & \alpha = 6, 7, 8, 9, \end{cases} \quad (2.3)$$

and

$$w_\alpha = \begin{cases} 4/9, & \alpha = 1, \\ 1/9, & \alpha = 2, 3, 4, 5, \\ 1/36, & \alpha = 6, 7, 8, 9, \end{cases} \quad (2.4)$$

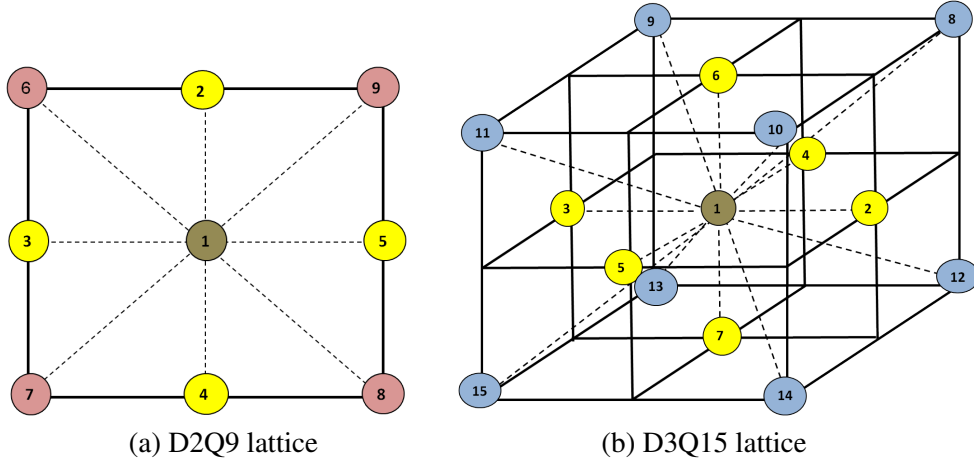


Figure 2.1: Lattice structures in two- and three-dimensional geometries.

respectively. In $D3Q15$ lattice, lattice velocities (\mathbf{e}_α) and the weighing coefficients (w_α) are given by:

$$\left[\mathbf{e}_1, \mathbf{e}_2, \dots, \mathbf{e}_{15} \right] = \begin{bmatrix} 0 & 1 & -1 & 0 & 0 & 0 & 0 & 1 & -1 & 1 & -1 & 1 & -1 & 1 & -1 \\ 0 & 0 & 0 & 1 & -1 & 0 & 0 & 1 & 1 & -1 & -1 & 1 & 1 & -1 & -1 \\ 0 & 0 & 0 & 0 & 0 & 0 & 1 & -1 & 1 & 1 & 1 & 1 & -1 & -1 & -1 \end{bmatrix}, \quad (2.5)$$

and

$$w_\alpha = \begin{cases} 2/9, & \alpha = 1, \\ 1/9, & \alpha = 2, 3, \dots, 7, \\ 1/72, & \alpha = 8, 9, \dots, 15, \end{cases} \quad (2.6)$$

respectively.

$\Gamma_\alpha(\mathbf{u})$ in Eqs. (2.1) and (2.2) is a function of macroscopic velocity \mathbf{u} , which is given by:

$$\Gamma_\alpha(\mathbf{u}) = w_\alpha \left[1 + \frac{\mathbf{e}_\alpha \cdot \mathbf{u}}{c_s^2} + \frac{(\mathbf{e}_\alpha \cdot \mathbf{u})^2}{2c_s^4} - \frac{\mathbf{u}^2}{2c_s^2} \right]. \quad (2.7)$$

The equilibrium distribution functions, f_α^{eq} and g_α^{eq} are given by:

$$f_\alpha^{eq} = w_\alpha \phi \left[1 + \frac{\mathbf{e}_\alpha \cdot \mathbf{u}}{c_s^2} + \frac{(\mathbf{e}_\alpha \cdot \mathbf{u})^2}{2c_s^4} - \frac{\mathbf{u}^2}{2c_s^2} \right] \quad \text{and} \quad (2.8)$$

$$g_\alpha^{eq} = w_\alpha \left[p + \rho c_s^2 \left(\frac{\mathbf{e}_\alpha \cdot \mathbf{u}}{c_s^2} + \frac{(\mathbf{e}_\alpha \cdot \mathbf{u})^2}{2c_s^4} - \frac{\mathbf{u}^2}{2c_s^2} \right) \right], \quad (2.9)$$

respectively, where $c_s^2 = 1/3$, wherein c_s is the velocity of sound in lattice unit.

Calculation of $\nabla\psi(\rho)$ and $\nabla\psi(\phi)$

In non-ideal gases or dense fluids, $\nabla\psi(\phi)$ mimics the physical intermolecular interactions and plays a key role in separating the phases through the term, $\nabla\psi(\rho) \equiv \nabla(p - c_s^2\rho)$. To calculate $\psi(\phi)$, the following expression of the Carnahan-Starling (C-S) equation of state is used [Carnahan & Starling (1969)]:

$$\psi(\phi) = c_s^2\phi \left[\frac{1 + \phi + \phi^2 - \phi^3}{(1 - \phi)^3} - 1 \right] - a\phi^2, \quad (2.10)$$

where a determines the strength of molecular interactions. This equation of state is used by several researchers working on LBM simulation of multiphase flows [Premnath & Abraham (2005), Chang & Alexander (2006), Fakhari & Rahimian (2009), Fakhari & Rahimian (2010)].

He *et al.* (1999b) showed that maximum and minimum values of the index function (ϕ) can be obtained from Eq. (2.10) for which $d(\psi + \phi RT)/d\phi < 0$. The critical value of a , a_c is 3.53374, below which the fluids cannot separate into different phases. Thus in the present study, a is chosen to be 4. By plotting the coexistence curve shown in Fig. 2.2, He *et al.* (1999b) found the minimum (ϕ_1) and maximum (ϕ_2) values of ϕ to be 0.04 and 0.259, respectively.

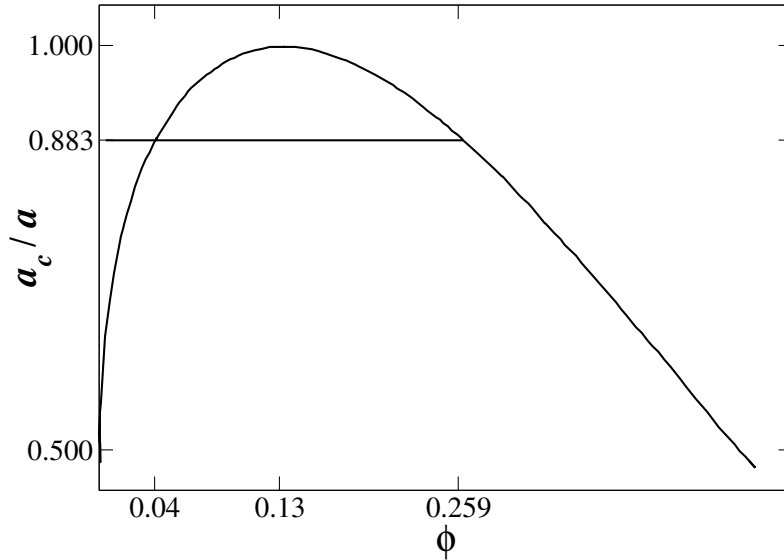


Figure 2.2: Coexistence curve of ϕ [He *et al.* (1999b)]

A fourth order compact scheme is used to discretize $\nabla\psi(\phi)$ and $\nabla\psi(\rho)$ [Lee & Lin (2005)], which are listed below.

For $D2Q9$ model,

$$\left(\frac{\partial\psi}{\partial x} \right)_{(i,j)} = \frac{1}{3} [\psi_{i+1,j} - \psi_{i-1,j}] + \frac{1}{12} [\psi_{i+1,j+1} - \psi_{i-1,j-1}] + \frac{1}{12} [\psi_{i+1,j-1} - \psi_{i-1,j+1}], \quad (2.11)$$

$$\left(\frac{\partial\psi}{\partial y} \right)_{(i,j)} = \frac{1}{3} [\psi_{i,j+1} - \psi_{i,j-1}] + \frac{1}{12} [\psi_{i+1,j+1} - \psi_{i-1,j-1}] + \frac{1}{12} [\psi_{i-1,j+1} - \psi_{i+1,j-1}]. \quad (2.12)$$

For $D3Q15$ model,

$$\begin{aligned} \left(\frac{\partial \psi}{\partial x}\right)_{(i,j,k)} &= \frac{1}{6} [\psi_{i+1,j,k} - \psi_{i-1,j,k}] + \frac{1}{12} [\psi_{i+1,j+1,k} - \psi_{i-1,j-1,k}] + \frac{1}{12} [\psi_{i+1,j-1,k} - \psi_{i-1,j+1,k}] + \\ &\quad \frac{1}{12} [\psi_{i+1,j,k+1} - \psi_{i-1,j,k-1}] + \frac{1}{12} [\psi_{i+1,j,k-1} - \psi_{i-1,j,k+1}], \end{aligned} \quad (2.13)$$

$$\begin{aligned} \left(\frac{\partial \psi}{\partial y}\right)_{(i,j,k)} &= \frac{1}{6} [\psi_{i,j+1,k} - \psi_{i,j-1,k}] + \frac{1}{12} [\psi_{i+1,j+1,k} - \psi_{i-1,j-1,k}] + \frac{1}{12} [\psi_{i-1,j+1,k} - \psi_{i+1,j-1,k}] + \\ &\quad \frac{1}{12} [\psi_{i,j+1,k+1} - \psi_{i,j-1,k-1}] + \frac{1}{12} [\psi_{i,j+1,k-1} - \psi_{i,j-1,k+1}], \end{aligned} \quad (2.14)$$

$$\begin{aligned} \left(\frac{\partial \psi}{\partial z}\right)_{(i,j,k)} &= \frac{1}{6} [\psi_{i,j,k+1} - \psi_{i,j,k-1}] + \frac{1}{12} [\psi_{i+1,j+1,k} - \psi_{i-1,j-1,k}] + \frac{1}{12} [\psi_{i-1,j-1,k} - \psi_{i+1,j+1,k}] + \\ &\quad \frac{1}{12} [\psi_{i,j+1,k+1} - \psi_{i,j-1,k-1}] + \frac{1}{12} [\psi_{i,j-1,k+1} - \psi_{i,j+1,k-1}], \end{aligned} \quad (2.15)$$

where i , j and k are grid indices in the x , y and z directions, respectively. The present methodology slightly differs from that of He *et al.* (1999a,b) and Zhang *et al.* (2000) in which they used third order upwinding to discretize $\nabla\psi$. The fourth order compact scheme is chosen here as it has less dissipation error.

External forces:

The surface tension force (F_s) and gravity force (\mathbf{G}) in Eq. (2.2) are given by

$$F_s = \kappa\phi\nabla\nabla^2\phi \quad \text{and} \quad \mathbf{G} = (\rho - \rho_m)\mathbf{g}, \quad (2.16)$$

respectively, where κ is the magnitude of surface tension, \mathbf{g} is gravity component and $\rho_m \equiv (\rho_1 + \rho_2)/2$.

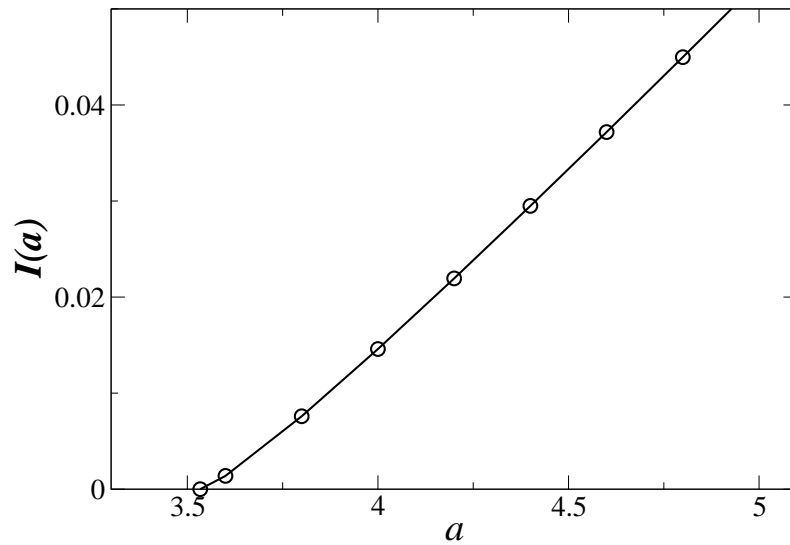


Figure 2.3: Dependence of I on a [Zhang *et al.* (2000)].

The surface tension, σ , in the LBM multiphase model can be obtained by:

$$\sigma = \kappa \int \left(\frac{\partial \phi}{\partial \zeta} \right)^2 d\zeta, \quad (2.17)$$

where ζ is the direction normal to the interface. Using the C-S equation of state, for a given a , and given numerical scheme, the surface tension can be chosen as [Zhang *et al.* (2000)]:

$$\kappa = \frac{\sigma}{I(a)}, \quad (2.18)$$

where

$$I(a) = \int \left(\frac{\partial \phi}{\partial \zeta} \right)^2 d\zeta. \quad (2.19)$$

The dependence of I on a for C-S equation of state is shown in Fig. 2.3, where the fitting curve [Zhang *et al.* (2000)] is given by

$$I(a) = \frac{0.1518(a - a_c)^{1.5}}{1 + 3.385(a - a_c)^{0.5}}. \quad (2.20)$$

The second order derivative in Eq. (2.16) to calculate the surface tension force is evaluated as follows:
For $D2Q9$ model,

$$\nabla^2 \phi = \frac{1}{6} [\phi_{i+1,j+1} + \phi_{i-1,j+1} + \phi_{i+1,j-1} + \phi_{i-1,j-1} + 4(\phi_{i+1,j} + \phi_{i-1,j} + \phi_{i,j+1} + \phi_{i,j-1}) - 20\phi_{i,j}]. \quad (2.21)$$

For $D3Q15$ model,

$$\begin{aligned} \nabla^2 \phi = \frac{1}{6} [& \phi_{i+1,j+1,k} + \phi_{i-1,j-1,k} + \phi_{i+1,j-1,k} + \phi_{i-1,j+1,k} + \phi_{i+1,j,k+1} + \phi_{i-1,j,k-1} + \phi_{i+1,j,k-1} + \\ & \phi_{i-1,j,k+1} + \phi_{i,j+1,k+1} + \phi_{i,j-1,k-1} + \phi_{i,j+1,k-1} + \phi_{i,j-1,k+1} + 2\phi_{i+1,j,k} + \\ & 2\phi_{i-1,j,k} + 2\phi_{i,j+1,k} + 2\phi_{i,j-1,k} + 2\phi_{i,j,k+1} + 2\phi_{i,j,k-1} - 2\phi_{i,j,k}]. \end{aligned} \quad (2.22)$$

Calculation of variables

The index function (ϕ), pressure (p) and the velocity field (\mathbf{u}) are calculated from the distribution functions as:

$$\phi = \sum f_\alpha, \quad (2.23)$$

$$p = \sum g_\alpha - \frac{1}{2} \mathbf{u} \cdot \nabla \psi(\rho) \delta t, \quad (2.24)$$

$$\rho \mathbf{u} c_s^2 = \sum \mathbf{e}_\alpha g_\alpha + \frac{c_s^2}{2} (\mathbf{F}_s + \mathbf{G}) \delta t. \quad (2.25)$$

The fluid density and kinematic viscosity are calculated from the index function using the following equations:

$$\rho(\phi) = \rho_2 + \frac{\phi - \phi_2}{\phi_1 - \phi_2} (\rho_1 - \rho_2), \quad (2.26)$$

$$\nu(\phi) = \nu_2 + \frac{\phi - \phi_2}{\phi_1 - \phi_2} (\nu_1 - \nu_2), \quad (2.27)$$

where ν_1 and ν_2 are the kinematic viscosities of fluid ‘1’ and ‘2’, respectively.

2.2 Boundary conditions

An important issue associated with LBM is the accurate implementation of the boundary conditions. The difficulty arises from the fact that in LBM while macroscopic pressure and velocity fields can be easily computed from the particle distribution functions, the reverse process is not easy. Noble *et al.* (1995) introduced the idea of hydrodynamic boundary conditions as an alternative to previously used bounce-back conditions and proposed use of the no-slip condition itself to find the missing particle distributions. The most straightforward hydrodynamic boundary condition is the equilibrium condition at the walls. Streaming components are not used and all the particle distribution functions are set to their equilibrium values. Equilibrium values can be obtained by using velocity and density values at the walls. Guo *et al.* (2002) proposed an extension of the second order accurate boundary condition suggested by Chen *et al.* (1996) and extrapolated the non-equilibrium parts from the interior nodes to add to the equilibrium values.

In the present work, the hydrodynamic boundary conditions based on the ghost fluid approach are used to simulate the boundaries and equilibrium distribution functions [Sahu & Vanka (2011)]. The non-equilibrium distribution functions are extrapolated and added to get the instantaneous distribution functions. Specifically, the boundary conditions are implemented as follows.

Index function ϕ : A second-order accurate zero derivative condition is used by placing the wall boundary condition between lattice points. This implies:

$$\phi_{1,j,k} = \phi_{2,j,k}; \quad \phi_{nx,j,k} = \phi_{nx-1,j,k}, \quad \text{for } j = 1, ny \text{ and } k = 1, nz; \quad (2.28)$$

$$\phi_{i,1,k} = \phi_{i,2,k}; \quad \phi_{i,ny,k} = \phi_{i,ny-1,k}, \quad \text{for } i = 1, nx \text{ and } k = 1, nz; \quad (2.29)$$

$$\phi_{i,j,1} = \phi_{i,j,2}; \quad \phi_{i,j,nz} = \phi_{i,j,nz-1}, \quad \text{for } i = 1, nx \text{ and } j = 1, ny, \quad (2.30)$$

where nx , ny and nz are number of lattice points in the x , y and z directions, respectively.

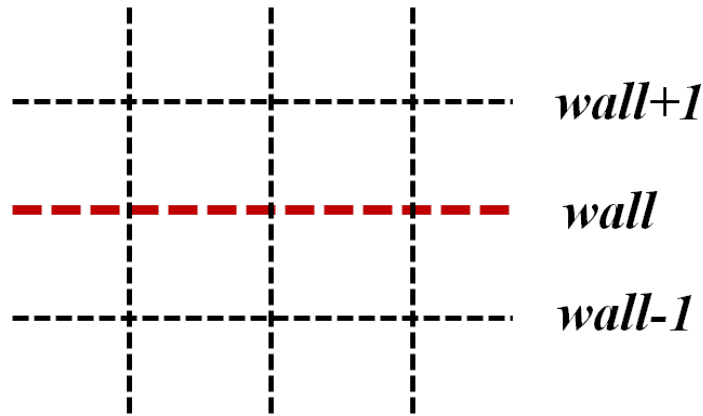


Figure 2.4: Grid near the wall.

Velocities: Velocities are mirror reflected to impose no slip and no penetration conditions. Thus,

$$U_{wall} = \frac{U_{wall+1} + U_{wall-1}}{2}; V_{wall} = \frac{V_{wall+1} + V_{wall-1}}{2}; W_{wall} = \frac{W_{wall+1} + W_{wall-1}}{2}, \quad (2.31)$$

where, subscript “wall” stands for wall node as shown in Fig. 2.4. In the present study, $U_{wall} = V_{wall} = W_{wall} = 0$.

Index distribution function (f):

$$f = f^{eq} + f^{neq}, \quad (2.32)$$

$$f_{1,j,k} = f_{1,j,k}^{eq} + f_{2,j,k}^{neq}; \quad f_{nx,j,k} = f_{nx,j,k}^{eq} + f_{nx-1,j,k}^{neq}, \quad (2.33)$$

$$f_{i,1,k} = f_{i,1,k}^{eq} + f_{i,2,k}^{neq}; \quad f_{i,ny,k} = f_{i,ny,k}^{eq} + f_{i,ny-1,k}^{neq}, \quad (2.34)$$

$$f_{i,j,1} = f_{i,j,1}^{eq} + f_{i,j,2}^{neq}; \quad f_{i,j,nz} = f_{i,j,nz}^{eq} + f_{i,j,nz-1}^{neq}. \quad (2.35)$$

Pressure and pressure function (g): Pressure is extrapolated with zero derivative boundary condition. Thus at walls,

$$P_{wall} = P_{wall\pm 1}. \quad (2.36)$$

This pressure is used to evaluate the equilibrium g value. However, in the expression for the equilibrium g function, the velocity at the grid node is taken to be zero instead of the ghost value. The equilibrium value is added to the extrapolated non-equilibrium value to get the final value of g that is streamed inside.

Density and ψ : The density is evaluated from the value of ϕ , which is extrapolated with zero derivative condition. The value of $\psi (\equiv p - \rho RT)$ is evaluated at all the lattice points including the boundary points using appropriate boundary values of p .

2.3 GPU Implementation

To accelerate the computational efficiency, the algorithm was implemented on a graphics processing unit (GPU). Brief introduction about the graphics processing unit and the review of the previous work conducted using GPU is given in Chapter 1. The architecture of GPU and the implementation of LBM on GPU are discussed below.

2.3.1 GPU Architecture

The architecture of GPU is quite different as compared to that of a CPU. It is designed with more transistors that are dedicated to computation and less resource dedicated to data caching and flow control compared to that of a CPU. The parallel processing in GPU is designed using multiple threads that execute instructions in a program. Each thread is unique and will be assigned to a unique element of data to be processed. The instructions for a GPU are written in a ‘kernel’ which is similar to a ‘function’ in ‘C’ programming. When a kernel is executed on a GPU, each thread executes the statements in that kernel and map to different elements of data. The threads are organized into ‘blocks’ and the blocks are

organized into ‘grid’ (see Fig. 2.5). The threads within a block share data through some ‘shared memory’ and synchronize their execution to coordinate memory accesses. The number of threads per block and the number of blocks depend on the data size to be processed. CPU executes the main program and the GPU can be utilized by launching the kernels from the main program. Therefore the CPU and GPU act simultaneously.

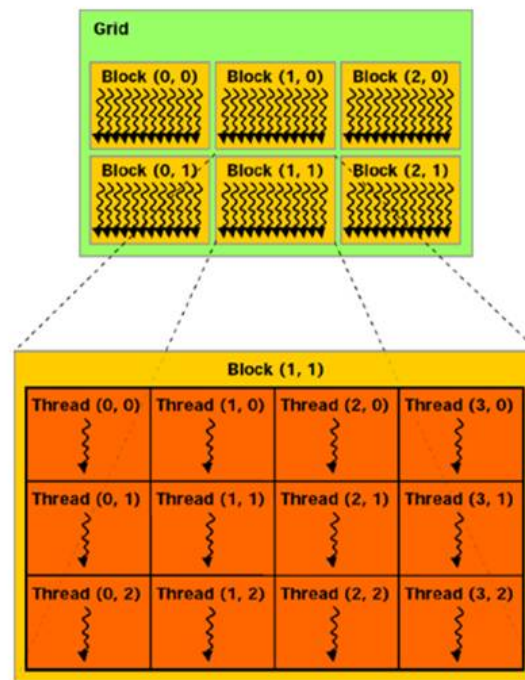


Figure 2.5: Thread hierarchy of GPU [Vanka *et al.* (2011)]

The memory spaces (RAM) of the CPU and GPU are separate. The GPU has multiple memory spaces; global memory, local memory, shared memory, constant memory and texture memory. Global memory is the largest memory space on the GPU. Each thread contains local memory to store the variables declared in the kernel. Blocks have the shared memory and the threads within the block have access to this memory. Detailed report on these memory spaces can be found in NVIDIA (2010).

2.3.2 GPU Programming

The structure of a program for a GPU is different than that of a CPU program. In a CPU code, the instructions given by a program are executed by a single CPU thread whereas in a GPU code, the instructions are executed in parallel by a batch of threads. GPU program eliminates the ‘for’ loops written in a CPU code and allows it to be executed in parallel. Other than the usual programming languages like C/C++ or FORTRAN, GPU algorithms are built on special programming languages that can provide parallel computing platform. In the present study, CUDA (Compute Unified Device Architecture), a parallel programming model developed by Nvidia Corporation is used. OpenCL, HLCL, Cg etc. are some other GPU programming languages. CUDA is available as CUDA C/C++ and CUDA FORTRAN depending on the compilers the programmers prefer to use. The high level languages are used with CUDA extensions to express parallelism, data locality and thread cooperation. CUDA programming model assumes that the CUDA threads execute on a physically separate ‘device’ (GPU) that operates as

a co-processor to the ‘host’ (CPU). That means when the kernels execute on a GPU rest of the program executes on CPU. The model assumes that both the ‘host’ and the ‘device’ maintain their own RAM, referred to as ‘host memory’ and ‘device memory’, respectively. Therefore, the program manages the global, constant and texture memory spaces visible to kernels through calls to the CUDA runtime. This includes device memory allocation and deallocation, as well as data transfer between the host and the device memory. The algorithm written in CUDA and implemented on GPU should be optimized carefully so as to get maximum performance. Minimum memory copies from host-to-device and device-to-host and the optimal block size and grid size would give higher throughput.

In the present work, the two-phase lattice Boltzmann method discussed above is implemented on graphics processing unit to perform the two-dimensional and three-dimensional simulations. Various graphic cards like the Tesla 1060, Tesla 2070 developed by the Nvidia corporation are used. The new Tesla Kepler K10, which is the fastest and most efficient high performance processor released by Nvidia most recently is also used to perform the three- dimensional simulations. The Kepler compute architecture gives three times higher performance than the Fermi compute architecture. Tesla K10 accelerator board features two Kepler GPUs each of 8GB onboard memory. Thus two GPU based programs can be run at a time. The GPU based LBM algorithm developed in our research group gives 25 times speed up over the corresponding CPU based code [Sahu & Vanka (2011)]. As all the steps in LBM are of explicit in nature, the error doesnot accumulate like in case of implicit code. The results obtained from single and double precision calculations are compared. It is found that the difference in the residual occurs only in the 4th decimal place, but the speed-up decreases to 8 times as compared to that of CPU based code.

A simple algorithm that shows the programing structure in CUDA is shown below. For the calculation of the fluid density using Eq. (2.26), the subroutine in FORTRAN can be written as:

```
do i=1,nx
  do j=1,ny
    do k=1,nz
      rho(i,j,k) = rho1+((phi(i,j,k)-phi1)/(phi2-phi1))*(rho2-rho1)
    end do
  end do
end do
```

When the subroutine is called, the density is estimated at all the grid points.

In a GPU program, a one-dimensional array is defined as $ijk = i + (j - 1) \times nx + (k - 1) \times nx \times ny$. Thus the total number of grids, ‘ntotal’ becomes $nx \times ny \times nz$. The above subroutine in CUDA kernel can be written as follows:

```
__global__ void
findvar_kernel (float *rho_d, float rho1, float rho2,
               float *phi_d, float phi1, float phi2)
{
  int ijk;
  float phit;
  int tx = threadIdx.x + blockIdx.x * blockDim.x;
  ijk    = tx + 1;
```



```

    phit = phi_d[ijk];

    rho_d[ijk] = rho1 + ((phit - phi1) / (phi2 - phi1)) * (rho2 - rho1);

    __syncthreads();
}

```

Kernel is defined using global declaration specifier. The variables in the kernel are declared using the syntax ‘kernelname ()’. Here the variable stated as ‘rho_d’ correspond to variable ‘rho’ on the device. Each variable is allocated memory on host and device in the main program before calling the kernel. This is implemented as:

```

rho = (float *) malloc(memsize_all);
float *rho_d; cudaMalloc((void**) &rho_d, memsize_all);

```

where ‘memsize all’ is the dynamic memory allocated on the host. Enough memory is allocated to reach the largest index. ‘cudaMalloc’ allocates memory on the device.

Each thread is given a unique thread ID which can be accessible within the kernel through threadIDx. ThreadIDx is a three-component vector so that either a one-dimensional or two-dimensional or three-dimensional thread block can be used. Although we use one-dimensional thread block, in general, one could have three-dimensional thread block. The total number of threads is equal to the number of threads per block times the number of blocks. For more details, the reader is referred to the cuda manual [NVIDIA (2010)].

Multiple blocks are organized into grids. The dimension of the grid is specified in the main program. The grid and the block dimension for the kernel execution are specified when calling the kernel using the ‘<<<, >>>’ syntax. This part in the main is shown below:

```

dim3 grid(ntotal/bx);
findvar_kernel<<<grid, block>>> (rho_d, rho1, rho2, phi_d, phi1, phi2);
cutilCheckMsg("Kernel execution failed");

```

Here ‘bx’ is the block size. The execution of each kernel is checked using ‘cutilCheckMsg’. Once the calculation is done on the device, the results are copied from device to host in the main. This is done as:

```

cudaMemcpy(rho_d, rho, memsize_all, cudaMemcpyHostToDevice);

```

After performing the simulation the allocated memory is deallocated which can be done using the following syntax:

```

free(rho);

```

The simulation time in CUDA can be recorded using the syntax given below.

```
CUDA_SAFE_CALL( cudaThreadSynchronize() );  
CUT_SAFE_CALL(cutStopTimer(timerApp));  
printf("GPU Kernel Time: %f (seconds)\n",  
       cutGetTimerValue(timerApp) / 1000.0);  
CUT_SAFE_CALL(cutDeleteTimer(timerApp));
```

This gives the simulation time using GPU. This time is compared with the corresponding time for the CPU based code. The comparison of the time taken by both codes reveals that GPU code is 25 times faster than our CPU based LBM code.

CHAPTER 3

Buoyancy-driven flow

In this chapter, the buoyancy-driven interpenetration of two immiscible fluids in a tilted channel (also commonly known as the lock-exchange problem [Debacq *et al.* (2003); Hallez & Magnaudet (2008); Séon *et al.* (2007a,b)] is discussed. It refers to the situation where the two fluids are initially separated by a partition and suddenly allowed to mix. The mixing occurs as a result of the interpenetration of the two fluids by the action of the gravitational force. As discussed in the introduction, this phenomenon plays an important role in the design of chemical and petroleum engineering processes [Benjamin (1968); Joseph *et al.* (1997)].

Séon *et al.* (2004, 2005) and Séon *et al.* (2007a,b) performed experiments to study the buoyancy-induced mixing of two miscible fluids in a tilted channel. They observed various flow regimes and mixing patterns for different tilt angles. All these studies considered the case of two fluids having equal kinematic viscosities. The fluids used in the experiments of Debacq *et al.* (2003) were water and glycerol solutions with the heavier fluid generated by adding CaCl_2 . The viscosity of the two fluids were changed by varying the concentration of glycerol, but both the fluids were selected to be of the same viscosity. However, the dynamics of the unsteady mixing can be quite different if the viscosities of the two fluids differed significantly from each other. Numerical studies of this flow have been carried out by few researchers. Hallez & Magnaudet (2008) used a finite volume method to study the buoyancy-induced mixing of two fluids in circular, rectangular and square geometries. Recently, Sahu & Vanka (2011) used a two-phase lattice Boltzmann method (LBM) to simulate the interpenetration of two immiscible fluids of same viscosities in a tilted channel. They investigated the effects of Atwood number, Reynolds number, tilt angle and surface tension in terms of flow structures, front velocities and velocity profiles.

To the best of my knowledge, no previous studies exist in literature in which the case of unequal fluid viscosities have been considered in the “lock-exchange” problem. In this work, the “mixing” of two immiscible fluids in a tilted channel is investigated with viscosity ratios, $10 \leq m \leq 0.1$ between the heavier and the lighter fluids. The main objective of this work has been to study the effects of a differential viscosity on the flow evolution in a tilted channel. The two-phase lattice Boltzmann method (see Chapter 2) using the two-dimensional-nine-velocity ($D2Q9$) model is used to simulate the problem. The effects of viscosity differential on the flow structures, average density profiles and front velocities are studied. Relatively stable fingers are observed for high viscosity ratios. The intensity of the interfacial instabilities and the transverse interpenetration of the fluids are seen to increase with decreasing viscosity differential of the fluids.

3.1 Problem definition

The buoyancy-driven flow in a tilted planar channel, as shown in Fig. 3.1 is considered, wherein fluid ‘1’ (dynamic viscosity μ_1 and density ρ_1) and fluid ‘2’ (dynamic viscosity μ_2 and density ρ_2) occupy the upper and the bottom halves of the channel, respectively. θ is the angle of inclination measured with

the horizontal. g is the acceleration due to gravity; the two components of gravity, $g \sin \theta$ and $g \cos \theta$ act in the axial and the transverse directions, respectively. The two fluids are considered to be Newtonian, incompressible and immiscible with varying viscosities and densities. The viscosity ratio, m , and the Atwood number, At , are defined as μ_1/μ_2 and $(\rho_1 - \rho_2)/(\rho_1 + \rho_2)$, respectively. A two-dimensional rectangular coordinate system, (x, y) , is used to model this flow, where x and y denote the axial and the transverse coordinates, respectively. The rigid and impermeable channel side walls are located at $y = 0$ and $y = H$, respectively; the sharp interface, which separates the immiscible fluids is at $x = L/2$, L being the length of the channel. The aspect ratio of the channel, L/H , is 40. As the flow is a balance between gravity and inertial forces, we used $V \equiv \sqrt{Hg}$ as the characteristic velocity with the width of the channel, H and $t \equiv \sqrt{H/g}$ as length and time scales, respectively; the Reynolds number is defined as $Re \equiv (H^{3/2}g^{1/2}\rho_1/\mu_1)$. In the present simulations, gravity is chosen such that $\sqrt{Hg} = 0.08$. The numerical method used in this study is discussed in the previous chapter.

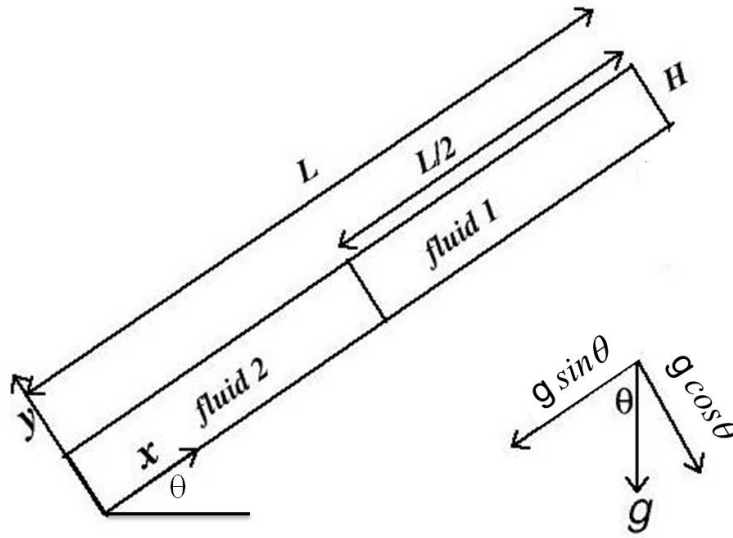


Figure 3.1: Schematic diagram of the initial equilibrium configuration of the system. Aspect ratio of the confined channel is 1 : 40.

3.2 Results and discussion

Grid Convergence test

First, the effect of grid resolution is investigated by considering three different grids. In Fig. 3.2 (a), (b) and (c), the spatio-temporal diagrams (time vs x plane) of $\int_0^H \phi dy$ obtained using 2562×66 , 3842×98 and 5122×130 lattice points, respectively are plotted. The rest of the parameter values used to generate this figure are $Re = 500$, $At = 0.1$, $m = 5$, $\kappa = 0.005$ and $\theta = 30^\circ$. Using these diagrams, one can study the movement of the “blue” and “red” fronts. The slopes of the left and right white dashed lines in each panel represent the front velocities of the heavier (V_r) and lighter (V_b) fluids, respectively. The velocities of the fingers obtained using different sets of lattice points are then compared in Table 1. In view of this observed small effect of the grid, we have chosen the 2562×66 grid for the rest of the parametric calculations. The results obtained using the present code agree with those obtained using

another home made finite volume code and also the experimental results of Seon and co-workers. The detailed validation of the present solver is reported by Sahu & Vanka (2011).

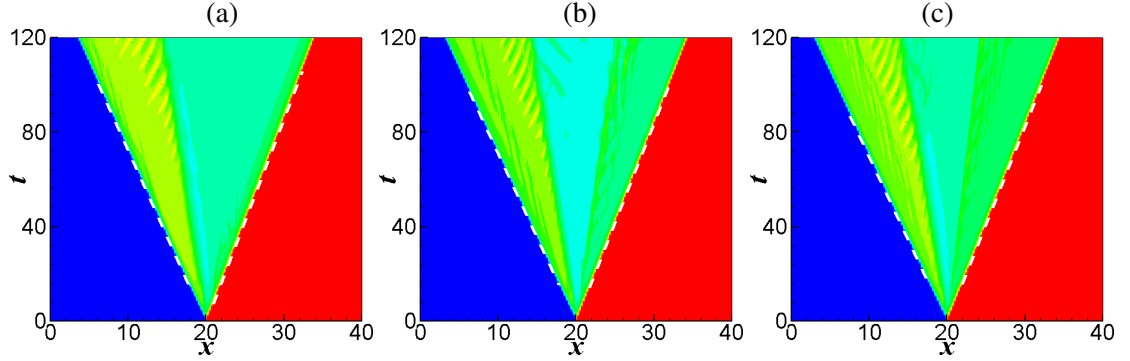


Figure 3.2: (a) Spatio-temporal diagram of $\int_0^H \phi dy$ obtained using (a) 2562×66 (b) 3842×98 and (c) 5122×130 grid points. The slope of the white dashed lines represent the front velocities. The rest of the parameter values are $Re = 500$, $At = 0.05$, $m = 5$, $\kappa = 0.005$ and $\theta = 30^\circ$.

Table 3.1: The velocities of the “red” (V_r) and “blue” (V_b) fingers for different grid densities. The rest of the parameter values are $Re = 500$, $At = 0.05$, $m = 5$, $\kappa = 0.005$ and $\theta = 30^\circ$.

Grid	V_r	V_b
2562×66	-0.1375	0.1159
3842×98	-0.1401	0.1189
5122×130	-0.1414	0.1202

The main objective of this work has been to study the effects of a differential viscosity on the flow evolution in a tilted channel. To this end, we begin the presentation of our results by first studying the effects of viscosity ratio on the spatio-temporal evolutions of the density contours for $At = 0.05$. Fig. 3.3 shows the density contours and velocity vector-fields at $t = 40$ and $t = 100$ for three viscosity ratios $m = 0.1$, 1 and 10. The rest of the parameter values are $Re = 500$, $\kappa = 0$ and $\theta = 60^\circ$. It can be seen that the component of the gravitational force in axial direction, proportional to $g \sin \theta$, induces a downward motion of the heavier fluid which in turn, by mass conservation, displaces the lighter fluid to move into the region of the heavier fluid. Thus both the heavier and lighter fluids are accelerated into the lower and upper parts of the channel, respectively. On the other hand, the component of the gravitational force in the transverse direction, proportional to $g \cos \theta$, acts to segregate the two fluids. For viscosity ratio, $m = 0.1$, the interface between the fluids becomes quite unstable, giving rise to the development of the interfacial instabilities as shown in Fig. 3.3(a). These instabilities manifest themselves in the form of vortical structures which entrain the fluids into each other, as shown by the velocity vector-fields in Fig. 3.3. For $m = 10$ (shown in Fig. 3.3(c)), which corresponds to a case when fluid ‘1’ is ten times more viscous than fluid ‘2’, it can be seen that the fingers of the heavier and lighter fluids are less unstable as they move towards the bottom and top parts of the channel, respectively. Inspection of Fig. 3.3 reveals that the flow dynamics and interpenetration of the fluids for $m = 1$ (shown in Fig. 3.3(b)) lies in an intermediate level to those for $m = 0.1$ and $m = 10$, as shown in Fig. 3.3(a) and (c), respectively. The intensity of the interfacial instabilities and small-scale structures increases with decreasing viscosity ratio. Close inspection of Fig. 3.3 reveals that the velocity of the fingers increases with decreasing viscosity ratio. By conducting linear stability analyses in pressure-driven displacement flow and flow through porous

media, many authors [Sahu *et al.* (2009a); Tan & Homsy (1986)] shown that if the displacing fluid is less viscous than the displaced one, the interface separating them becomes unstable and fingering pattern develops at the interface. In the present study, $m = 0.1$ corresponds to a situation when the less viscous fluid induces into the region of high viscous fluid, which can be related to an unstable configuration of displacement flows. However, $m = 10$ is fundamentally different for $m = 0.1$, although both represent 10 times difference in viscosity between two fluids. For $m = 10$, the highly viscous fluid displaces the less viscous fluid which is known to be a stable configuration.

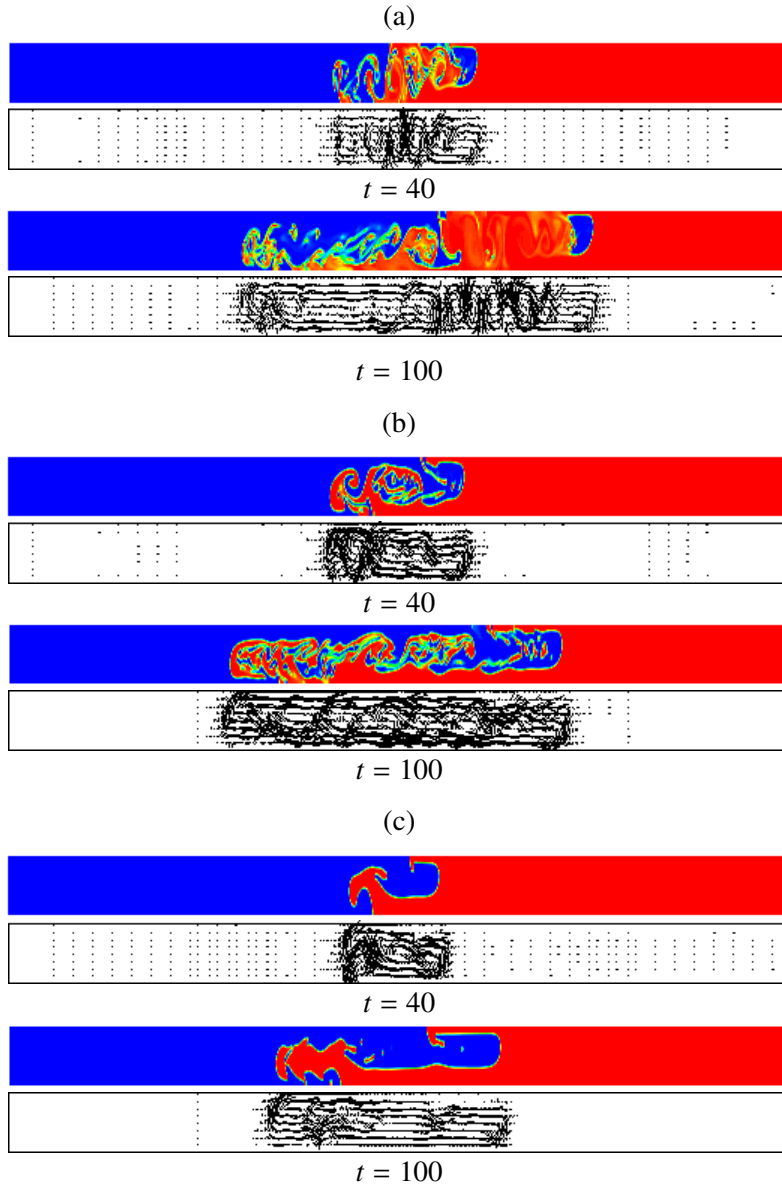


Figure 3.3: Spatio-temporal evolutions of the density contours and velocity vector-fields for (a) $m = 0.1$, (b) $m = 1$ and (c) $m = 10$. The rest of the parameter values are $Re = 500$, $At = 0.05$, $\kappa = 0$ and $\theta = 60^\circ$.

In Fig. 3.4, we compare the axial variation of the depth-averaged c ($\bar{c}_x = \int_0^H c dy/H$) and the transverse variation of the axially-averaged c ($\bar{c}_y = \int_0^L c dx/L$) for the parameter values the same as those used to generate Fig. 3.3. Here $c \equiv (\rho - \rho_2)/(\rho_1 - \rho_2)$. It can be seen in Fig. 3.4(a), (c) and (e) that the variation of \bar{c}_x along the axial direction is complex for this set of parameters. However, in the

experimental study of lock-exchange flow of two miscible fluids in a vertical tube, Debacq *et al.* (2003) found that the flow dynamics is diffusive in nature. In Fig. 3.4(b), (d) and (f), it can be seen that profiles of \bar{c}_y are asymmetrical in the y -direction. This is due to the effect of segregation of the fluids due to the transverse gravitational force. Close inspection of the figure also reveals that the \bar{c}_y profile for $m = 1$ (Fig. 3.4(b)) is less asymmetrical as compared to those for $m = 10$ and $m = 0.1$.

Next, in Fig. 3.5, the effect of surface tension on the density contours is investigated by considering three values of the surface tension parameter (κ) at $t = 80$. The rest of the parameter values are the same as those used to generate Fig. 3. It can be seen that the surface tension makes the flow dynamics coherent by stabilizing the flow; increasing κ value, which corresponds to increase in surface tension, increases the stabilizing influence. Close inspection of Fig. 3.5 also reveals that for the same κ value the flow with higher viscosity ratio is more coherent than that with lower viscosity ratios. For example, the flow dynamics for $\kappa = 0.005$ and $m = 10$ (shown in the third panel of Fig. 3.5(c)) is more stable than that for $\kappa = 0.005$ and $m = 0.1$ (shown in the third panel of Fig. 3.5(a)). It can also be seen in Fig. 3.5 (c) that for $\kappa = 0.005$ and $m = 10$ both the fingers are always attached to the walls, but for other cases considered ($m = 1$ and $m = 0.1$) the fingers propagate nearly at the centerline of the channel surrounded by the opposite fluid. The effect of κ on the axial variation of \bar{c}_x and the transverse variation of \bar{c}_y are shown in Fig. 3.6. It can be seen in Fig. 3.6(a), (b) and (c) that the complexity in the variation of \bar{c}_x is significantly reduced with increasing κ value. This is also evident from Fig. 3.5 as increasing κ stabilizes the density contours.

In Fig. 3.7, the evolution of the density contours and velocity vector-fields are shown for a tilt angle of 30° for the same three viscosity ratios. The rest of the parameter values are the same as those for $\theta = 60^\circ$ (Fig. 3.3). In this case, as the channel is tilted closer to the vertical compared to the $\theta = 60^\circ$ case, the transverse gravitational force (proportional to $g\cos\theta$) segregating the two fluids is stronger, thus resulting in decreased interpenetration of the fluids in the transverse direction (Fig. 3.7). The two fluids now move more parallel to each other quite coherently and expectedly interpenetration in the transverse direction is reduced as shown by the velocity vectors in Fig. 3.7. It can also be seen that unlike the previous case of $\theta = 60^\circ$ (Fig. 3.3), both the fingers are attached to the walls for all the three viscosity ratios considered. This is primarily a consequence of the increased transverse gravitational force at the larger tilt angles. The axial variation of the depth-averaged c ($\bar{c}_x = \int_0^H c dy/H$) and the transverse variation of the axially-averaged c ($\bar{c}_y = \int_0^L c dx/L$) are also studied with the parameter values the same as those for Fig. 3.7. A similar conclusion as for Fig. 3.4 can be drawn from Fig. 3.8 as well. The variation of \bar{c}_x in the axial direction in Fig. 3.8(e) is smooth as the density contours obtained in this case are free from the instabilities (see Fig. 3.7(c)). It can be seen in Fig. 3.8(a) and (c) that the variation of \bar{c}_x is complex for smaller viscosity ratios. In Fig. 3.8(b), (d) and (f), it can be seen that profiles of \bar{c}_y are asymmetrical in the y -direction.

The density contours and velocity vector-fields at $t = 80$ for different values of κ are shown in Fig. 3.9(a), (b) and (c) for $m = 0.1$, $m = 1$ and $m = 10$, respectively. The rest of the parameter values are the same as those used to generate Fig. 3.7. As expected, it can be seen that for this case also surface tension makes the structures more coherent with increasing κ value. This behavior is also evident in Fig. 3.10. For $m = 1$ case (Fig. 3.9(b)), a third finger of the heavier fluid propagate in the same direction (towards the upper part of the channel) as that of the lighter fluid. This finger is not observed for $m \neq 1$ cases.

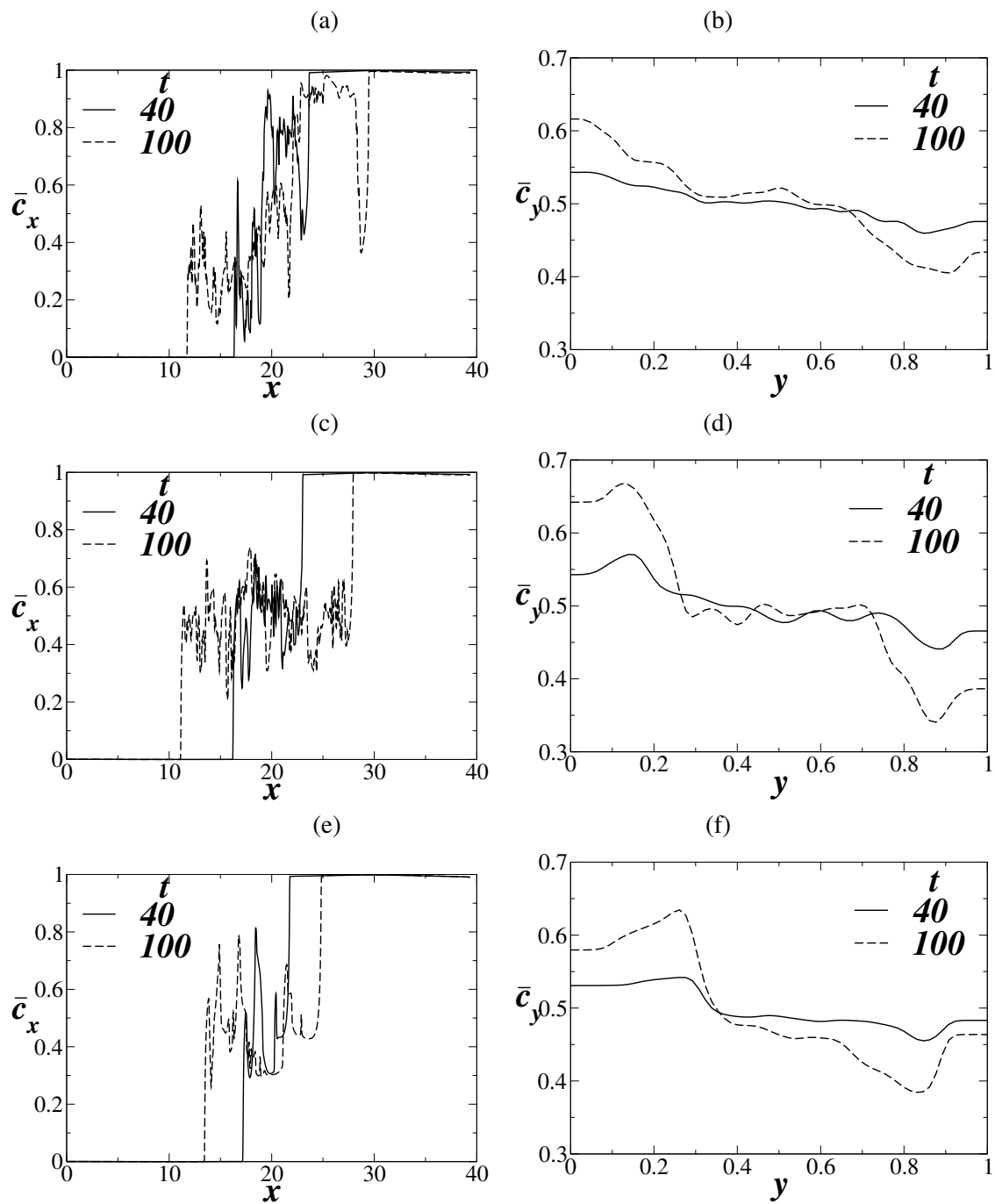


Figure 3.4: Evolution of the axial variation of the depth-averaged c (\bar{c}_x) and the transverse variation of the axial-averaged c (\bar{c}_y) for (a,b) $m = 0.1$, (c,d) $m = 1$ and (e,f) $m = 10$, respectively. The rest of the parameter values are $Re = 500$, $At = 0.05$, $\kappa = 0$ and $\theta = 60^\circ$.

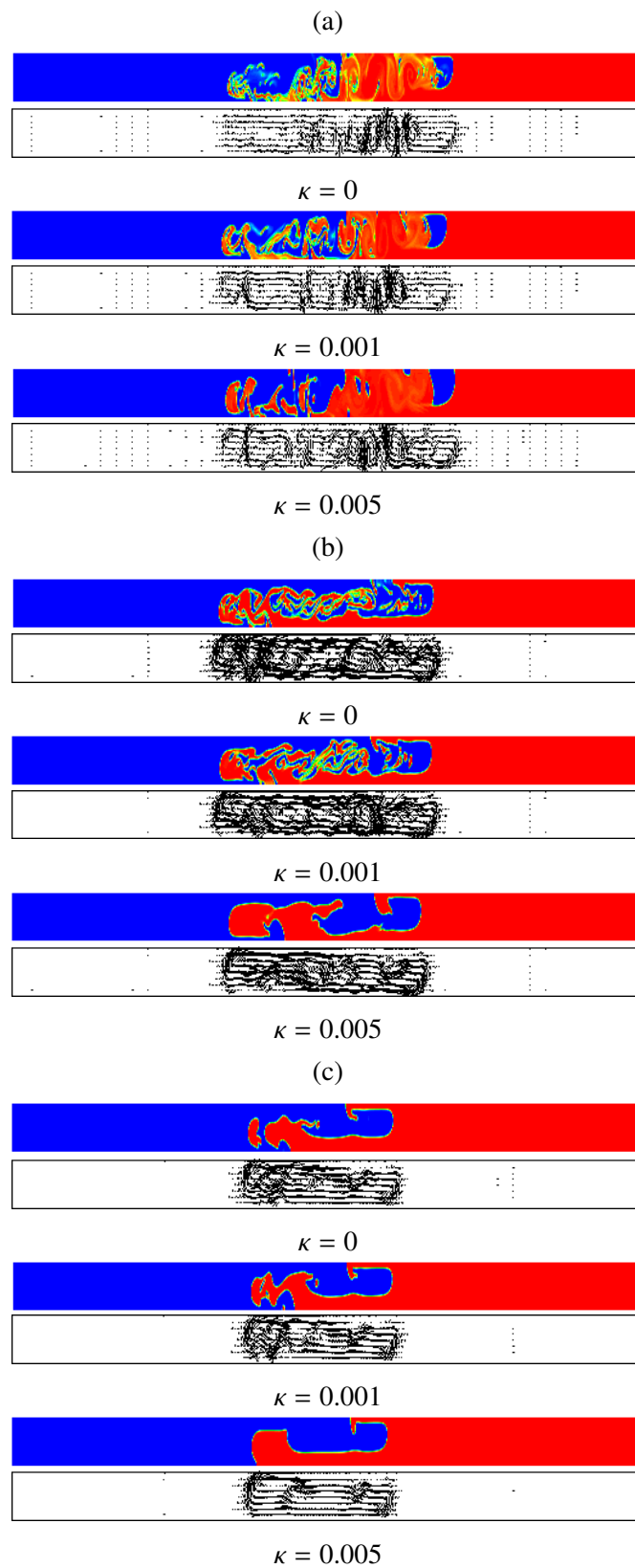


Figure 3.5: Effects of surface tension parameter (κ) on the density contours and velocity vector-fields at $t = 80$ for (a) $m = 0.1$, (b) $m = 1$ and (c) $m = 10$. The rest of the parameter values are $Re = 500$, $At = 0.05$ and $\theta = 60^\circ$.

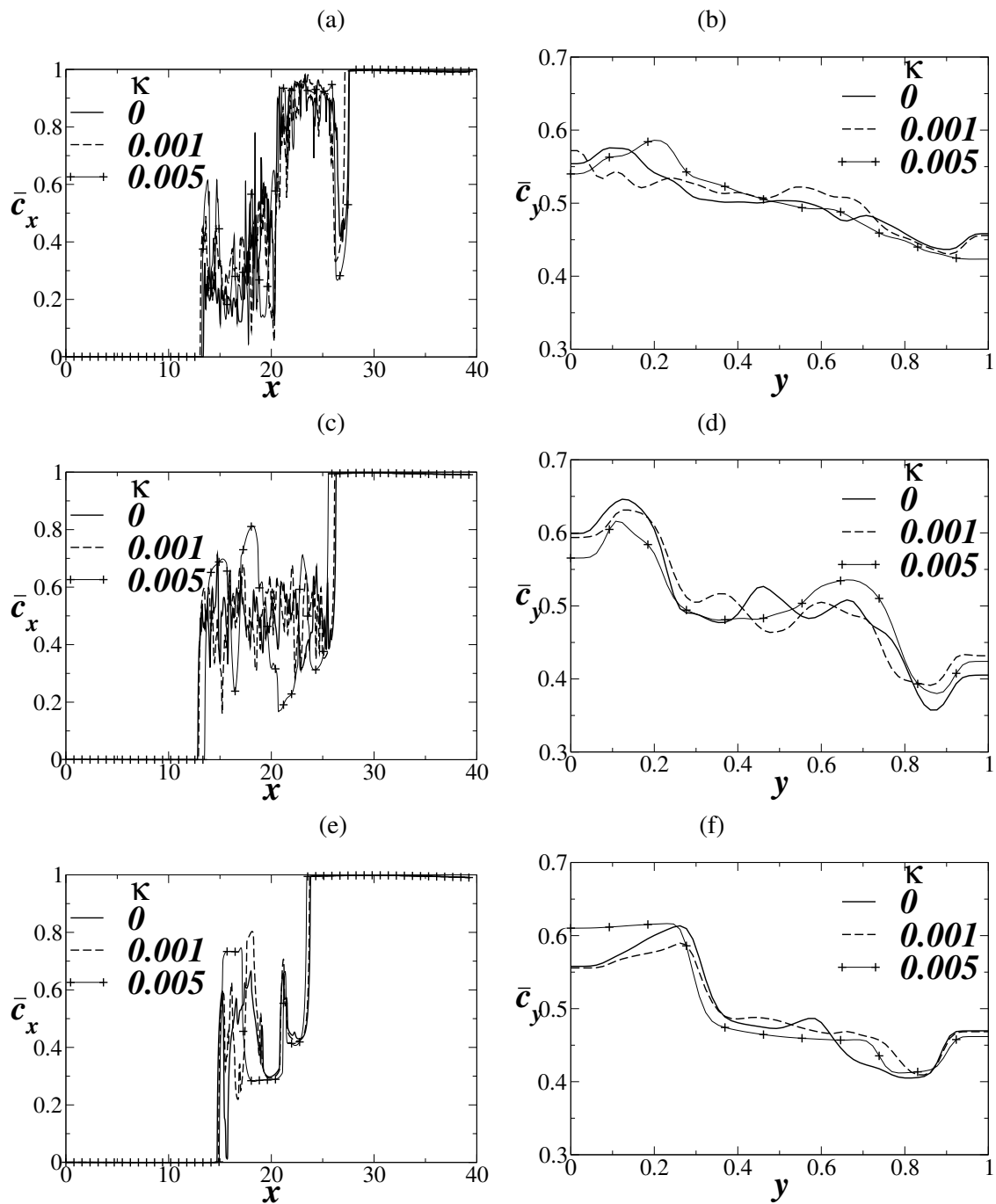


Figure 3.6: Effects of surface tension parameter (κ) on the axial variation of the depth-averaged c (\bar{c}_x) and the transverse variation of the axial-averaged c (\bar{c}_y) at $t = 80$ for (a,b) $m = 0.1$, (c,d) $m = 1$ and (e,f) $m = 10$, respectively. The rest of the parameter values are $Re = 500$, $At = 0.05$ and $\theta = 60^\circ$.

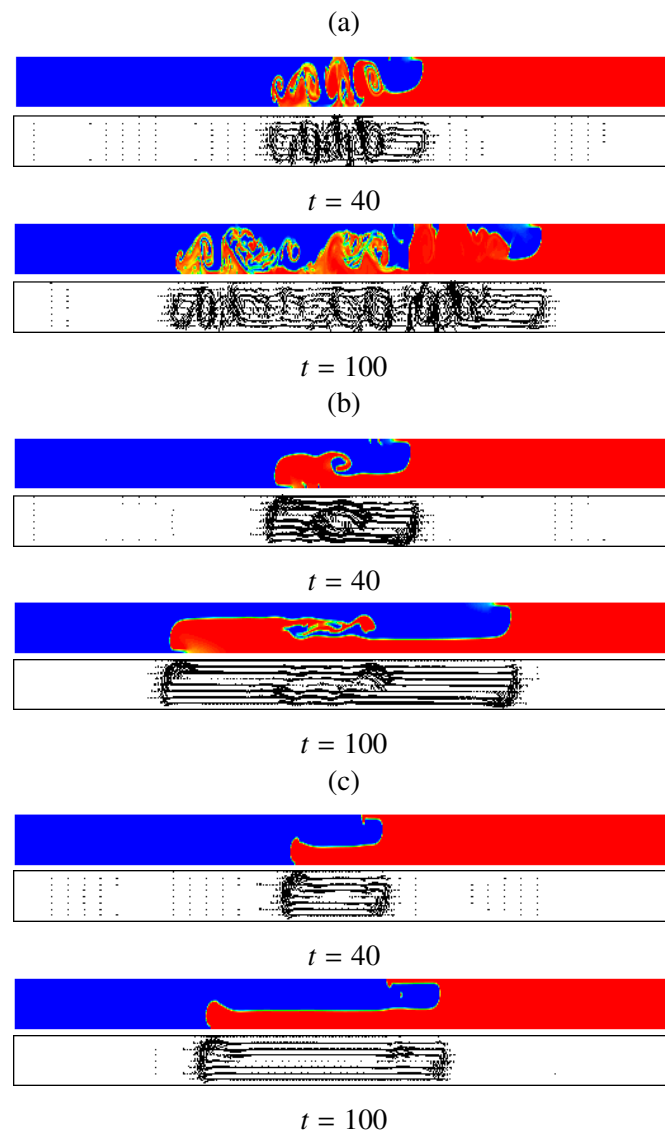


Figure 3.7: Spatio-temporal evolutions of the density contours and velocity vector-fields for (a) $m = 0.1$, (b) $m = 1$ and (c) $m = 10$. The rest of the parameter values are $Re = 500$, $At = 0.05$, $\kappa = 0$ and $\theta = 30^\circ$.

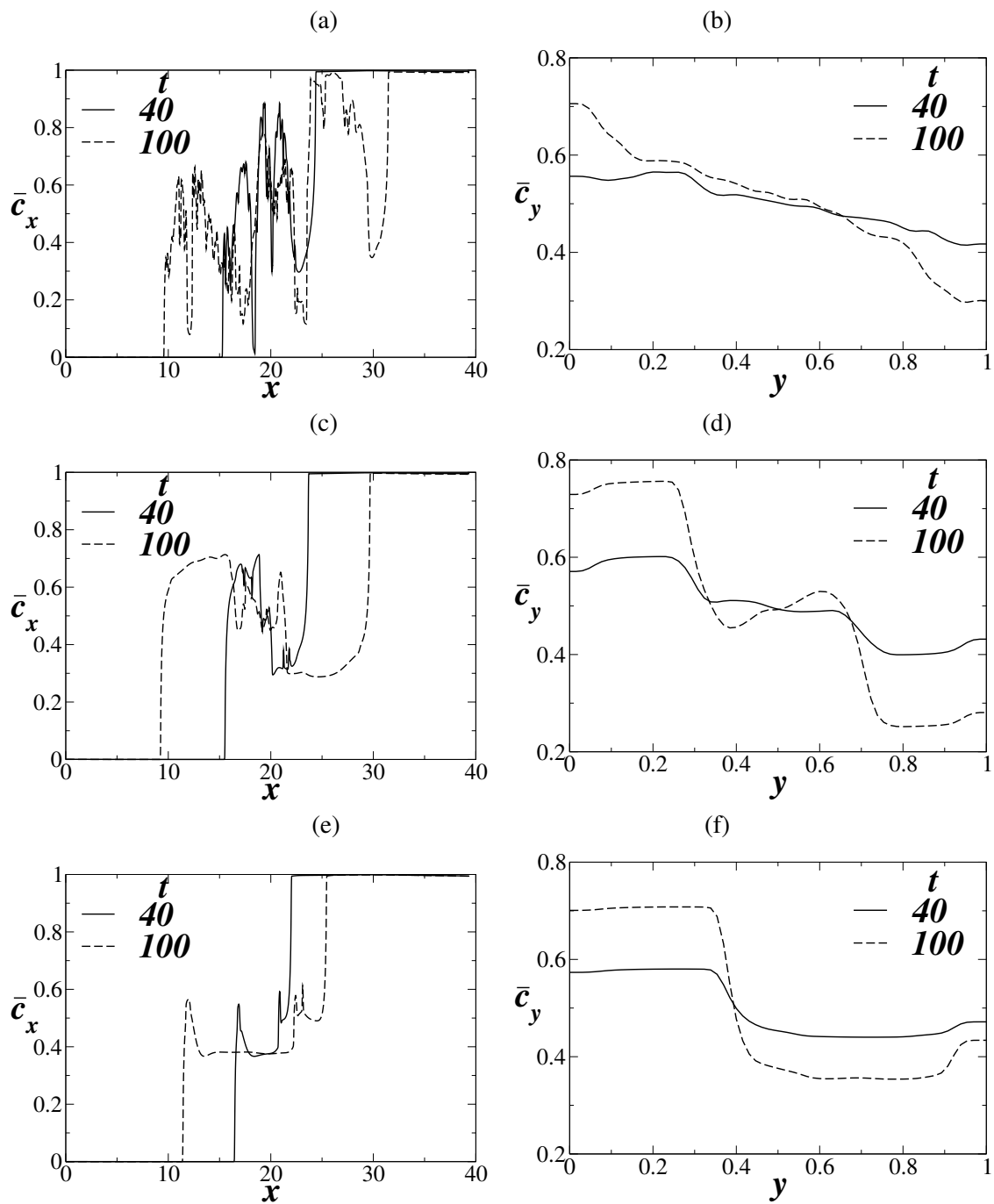


Figure 3.8: Evolution of the axial variation of the depth-averaged c (\bar{c}_x) and the transverse variation of the axial-averaged c (\bar{c}_y) for (a,b) $m = 0.1$, (c,d) $m = 1$ and (e,f) $m = 10$, respectively. The rest of the parameter values are $Re = 500$, $At = 0.05$, $\kappa = 0$ and $\theta = 30^\circ$.

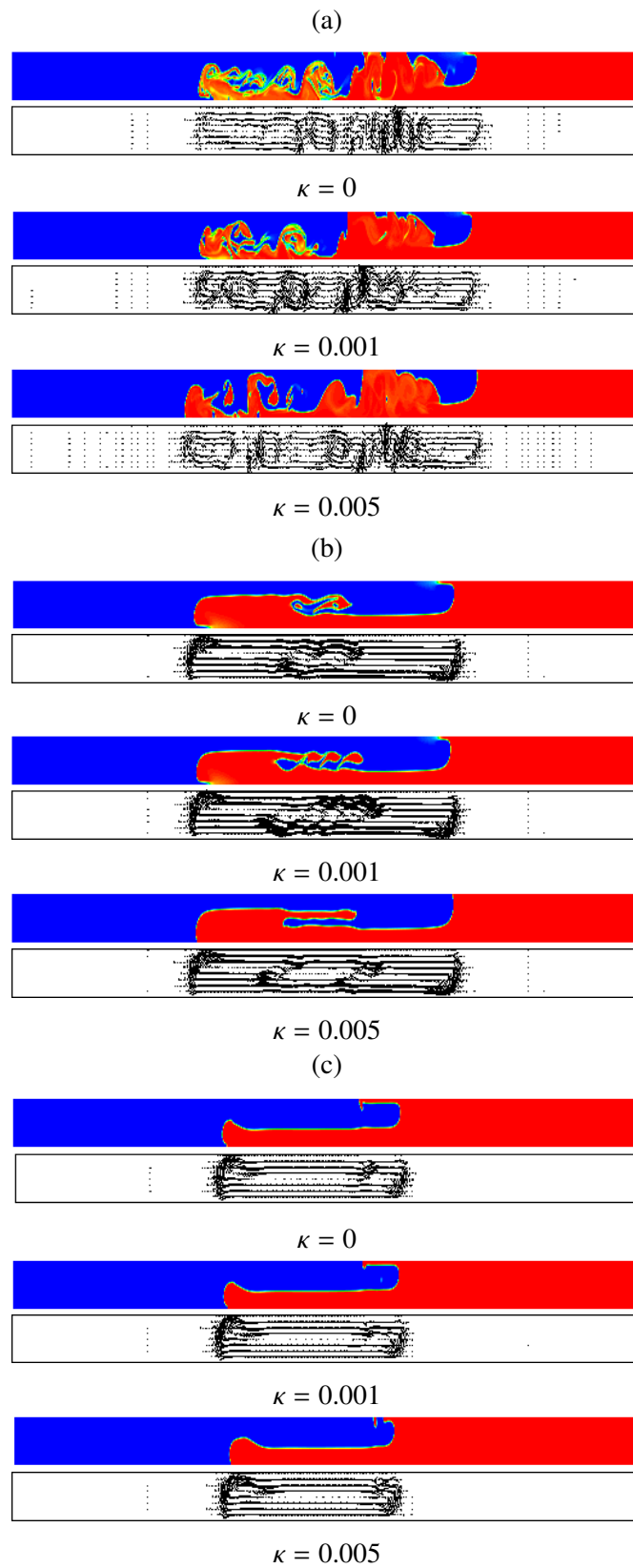


Figure 3.9: Effects of surface tension parameter (κ) on the density contours and velocity vector-fields at $t = 80$ for (a) $m = 0.1$, (b) $m = 1$ and (c) $m = 10$. The rest of the parameter values are $Re = 500$, $At = 0.05$ and $\theta = 30^\circ$.

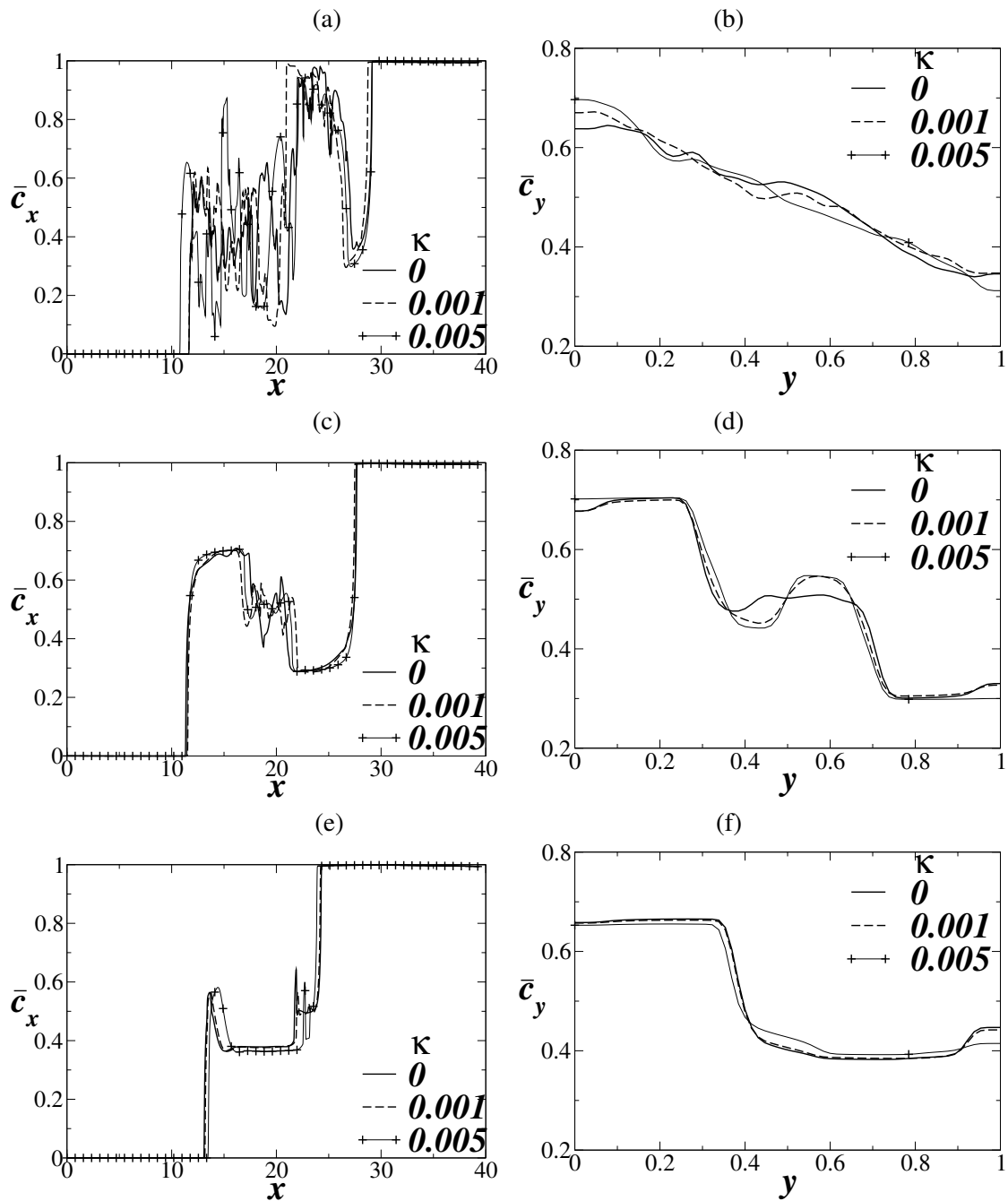


Figure 3.10: Effects of surface tension parameter (κ) on the axial variation of the depth-averaged c (\bar{c}_x) and the transverse variation of the axial-averaged c (\bar{c}_y) at $t = 80$ for (a,b) $m = 0.1$, (c,d) $m = 1$ and (e,f) $m = 10$, respectively. The rest of the parameter values are $Re = 500$, $At = 0.05$ and $\theta = 30^\circ$.

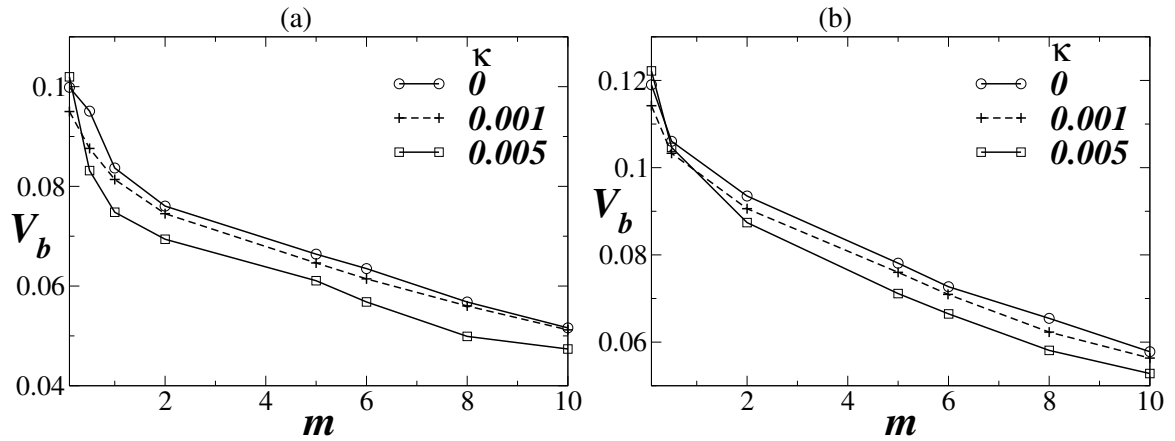


Figure 3.11: Variation of the front velocity of the “blue” fluid, V_b with m for (a) $\theta = 60^\circ$ and (b) $\theta = 30^\circ$. The rest of the parameter values are $Re = 500$ and $At = 0.05$.

Finally, the variation of the front velocities of the “blue” fluid (V_b) with viscosity ratio (m) are studied for three κ values. This is shown in Fig. 3.11 (a) and (b) for $\theta = 60^\circ$ and $\theta = 30^\circ$, respectively. The rest of the parameter values are the same as those used to generate Fig. 3.3. It is seen that V_b decreases with increase in m for both values of the tilt angle considered. This behavior can also be observed in the spatio-temporal evolutions of the density contours (in Figs. 3.3 and 3.7). A similar trend is observed (not shown) for the “red” fluid as well. It is also observed that at low At , the two fronts move with an almost equal velocity for this set of parameters. However, there is small difference between the velocity of the finger tips at the higher Atwood numbers.

In the next section, buoyancy driven flow in an three-dimensional inclined channel is presented. The results obtained from the three-dimensional simulation are compared with those of the 2D simulations.

3.3 Buoyancy driven flow in a three-dimensional inclined channel

In this section, two-phase lattice Boltzmann simulation of three-dimensional buoyancy-driven flow of two immiscible liquids in a confined square duct is discussed. The length, height and width of the channel are L , H and W , respectively, as shown in Fig. 3.12. A three-dimensional rectangular coordinate system (x, y, z) is used to model the flow dynamics. We considered $W = H$ and the aspect ratio of the channel L/H to be 32. θ is the angle of inclination measured with the horizontal. The three components of gravity $g_x (= g \sin \theta)$, $g_y (= g \cos \theta)$ and $g_z (= 0)$ act in the negative axial, negative transverse and the azimuthal directions, respectively. The grid size considered here is $(32 \times 64) \times 64 \times 64$.

The spatio-temporal evolution of the iso-surface of ϕ at the interface is shown in Fig. 3.13 at different times. The parameters that are used to generate the contours are $Re = 500$, $m = 1$, $At = 0.05$, $\kappa = 0$ and the angle of inclination, $\theta = 60^\circ$ measured with the horizontal. As the time progresses, the heavier fluid occupying the upper part of the channel move into the region of the lighter fluid at the bottom part of the channel. This downward motion is caused by the axial component of gravity, $g \sin \theta$. The transverse component of gravity, $g \cos \theta$ induces segregating effect. It can be seen that the interface between the fluids become unstable and the instabilities develop in the form of small structures.

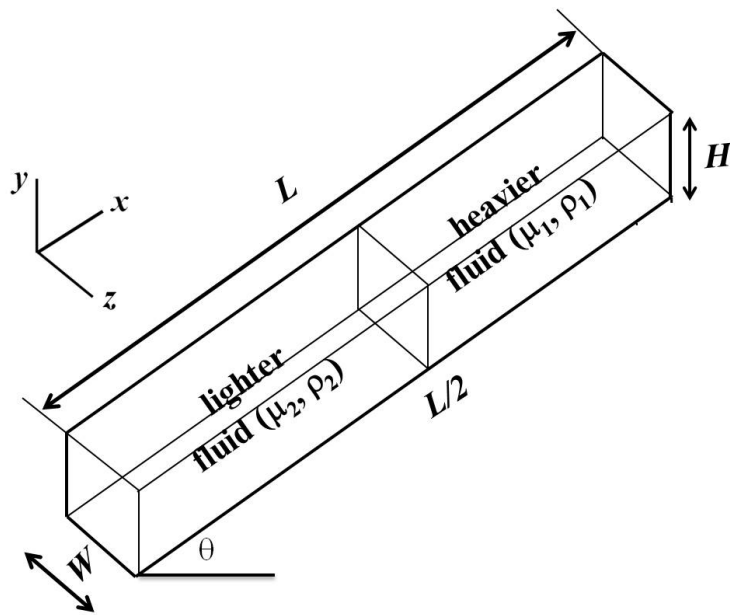


Figure 3.12: Schematic diagram of the initial equilibrium configuration of the system. Aspect ratio of the confined channel is 1 : 32.

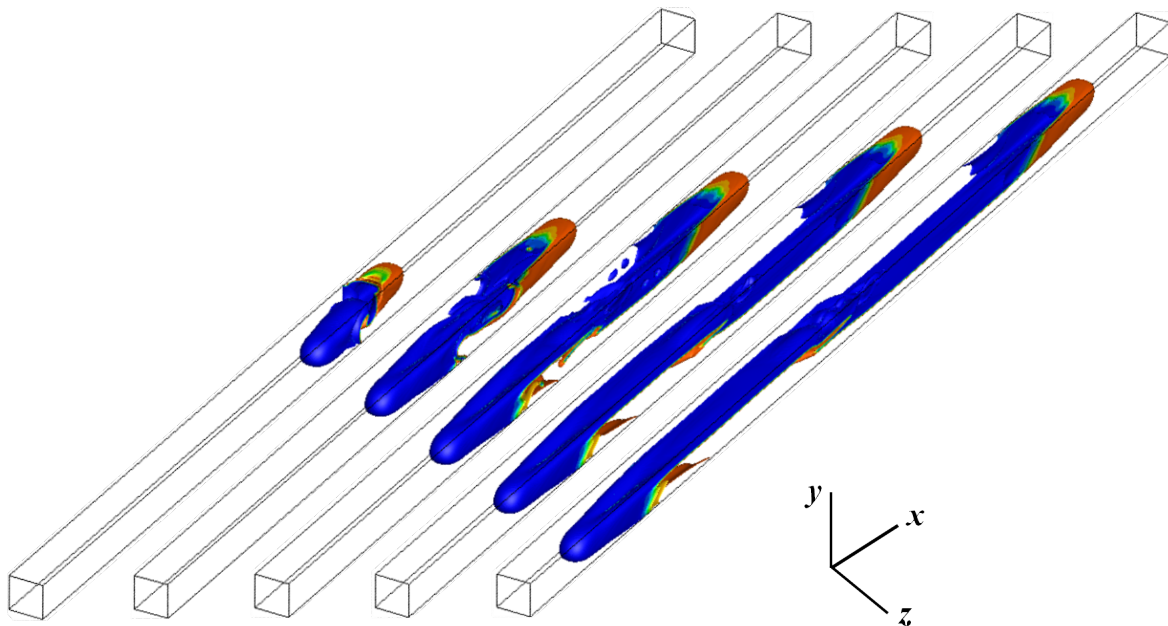


Figure 3.13: Evolution of the isosurface of ϕ at the interface at different times (from left to right: $t = 20, 40, 60, 80$ and 100). The parameters are $Re = 100, m = 1, At = 0.05, \kappa = 0$ and $\theta = 60^\circ$.

The x - y cross-section of the three-dimensional channel is considered and the contours obtained in this plane are shown in Fig. 3.14(a). For the same parameters, two-dimensional simulation is carried out and the results obtained is shown in Fig. 3.14(b). Therefore, comparing Fig. 3.14(a) and 3.14(b), it is observed that the two-dimensional simulation gives the contours with more small scale structures which are not seen in 3D. One can say that the structure of the instabilities is different in 3D and a more stable mixing is seen for this set of parameters. The instabilities appear more at the central portion of the channel and smooth fingers are seen towards the both ends. It is also evident from the figure that the three-dimensional instabilities are more coherent than that of the two-dimensional counterparts as found by Hallez & Magnaudet (2008) previously. Longer finger lengths are observed in 3D than that in 2D at the same instant of time. This is in agreement with the findings of Oliveira & Meiburg (2011).

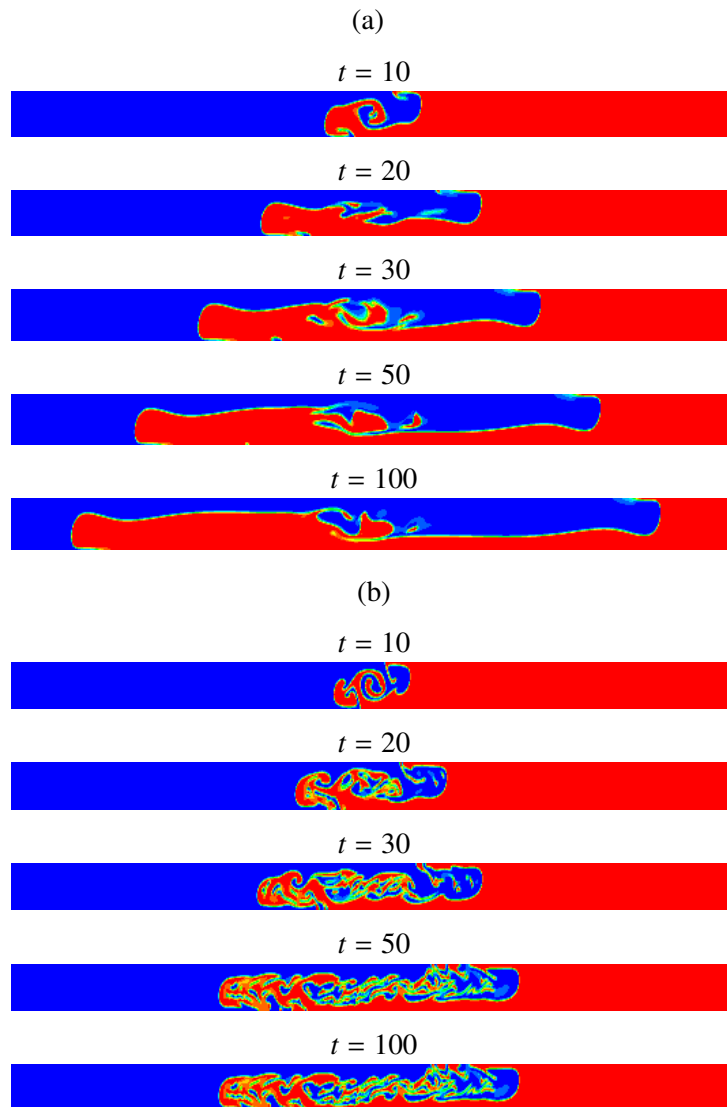


Figure 3.14: Spatio-temporal evolution of the contours of the index function ϕ at different times in (a) x - y plane of the 3D channel, and (b) 2D channel. The parameters are the same as that of Fig.3.13.

3.4 Summary

In this chapter, the effects of viscosity differential on a buoyancy-driven flow in tilted planar two- and three-dimensional channels are studied using a multiphase lattice Boltzmann method implemented on a graphics processing unit. The effects of viscosity differential on the flow structures, average density profiles and front velocities are investigated. Relatively stable fingers are observed for high viscosity ratios; the flow becomes essentially like two individual Poiseuille flows. The intensity of the interfacial instabilities and the transverse interpenetration of the fluids increase with decreasing viscosity differential of the fluids. Plots of the average density profiles show that the flow becomes progressively more complex with decreasing viscosity ratio. As expected, surface tension stabilizes the flow by reducing the small-scale structures. In three-dimensional simulations we found that the flow is more stable than that observed in two-dimensional channel. The length of the ‘finger’ is also found to be longer in three-dimensional buoyancy-driven flow than that in two-dimensional simulations.

CHAPTER 4

Pressure-driven displacement flow

In this chapter, the pressure-driven displacement of two immiscible fluids in an inclined channel in the presence of viscosity and density gradients is investigated. A systematic parametric study is conducted to investigate the effects of viscosity ratio (m), Atwood number, (At), Froude number, (Fr) and surface tension, which is characterized by capillary number (Ca). As Selvam *et al.* (2007) found that in core-annular flows beyond a critical viscosity ratio the flow is unstable even when the less viscous fluid is at the wall, the situation when a high viscous fluid displaces a less viscous one (a classically stable system) at high viscosity ratio is also investigated in the present study. The effects of angle of inclination on the flow dynamics are also investigated, which have not been studied earlier in the context of immiscible fluids. A linear stability analysis similar to the one of Sahu & Matar (2010) for a three-layer system is compared with the LBM simulations. The pressure-driven displacement flow of one fluid by another fluid is common in many industrial processes, such as transportation of crude oil in pipelines [Joseph *et al.* (1997)], oil recovery, food-processing, coating, flow of lava inside the earth [Whitehead & Helfrich (1991)], etc. In the latter case the temperature gradient also plays an important role in the flow dynamics. In porous media or in a Hele-Shaw cell, the displacement of a highly viscous fluid by a less viscous one becomes unstable forming various instability patterns widely known as viscous fingering [Homsy (1987)].

The rest of the chapter is organized as follows. The problem is formulated in Section 4.1, and the results of the lattice Boltzmann simulations are presented in Section 4.2. In Section 4.3, we discuss the results of the linear stability analysis, and provide concluding remarks in Section 4.4.

4.1 Problem description

Consider a two-dimensional channel of length L and height H , initially filled with a stationary, Newtonian, incompressible fluid of viscosity μ_2 and density ρ_2 (fluid ‘2’). Through an imposed pressure-gradient, this initially filled liquid is displaced by another immiscible liquid of viscosity μ_1 and density ρ_1 (fluid ‘1’), as shown in Fig. 4.1. A rectangular coordinate system (x, y) is used to model the flow dynamics, where x and y denote the coordinates in axial and the wall normal directions, respectively. The aspect ratio of the channel, L/H , is 48. The channel inlet and outlet are located at $x = 0$ and L , respectively. The rigid and impermeable walls of the channel are located at $y = 0$ and H , respectively. The initial configuration is arranged such that fluid ‘1’ and fluid ‘2’ occupy the channel from $0 \leq x \leq 5$ and $5 \leq x \leq L$, respectively. The prescribed boundary conditions are such that fluid can only enter and leave the channel through the inlet and outlet, respectively. θ is the angle of inclination measured with the horizontal. g is acceleration due to gravity; the two components of the gravity $g\sin\theta$ and $g\cos\theta$ act in the axial and transverse directions, respectively.

The hydrodynamic boundary conditions based on the ghost fluid approach are used to simulate the boundaries and equilibrium distribution functions [Sahu & Vanka (2011)]. A Neumann boundary

condition for pressure is used at the outlet, while a constant pressure-gradient obtained from the constant volumetric flow rate condition is imposed at the inlet. In addition, the non-equilibrium distribution functions are extrapolated and added to get the instantaneous distribution functions. Various dimensionless parameters describing the flow characteristics are the Atwood number, $At(\equiv (\rho_2 - \rho_1)/(\rho_2 + \rho_1))$, the Reynolds number, $Re(\equiv Q\rho_1/\mu_1)$, the Froude number, $Fr(\equiv Q/H\sqrt{AtgH})$, the capillary number, $Ca(\equiv Q\mu_1/\sigma H)$ and the viscosity ratio, $m = \mu_2/\mu_1$. Here, Q is the volumetric flow rate per unit length in the spanwise direction; in the present study the characteristic velocity is chosen such that the value of Q is 1.92. The dimensionless time is defined as $t = H^2/Q$.

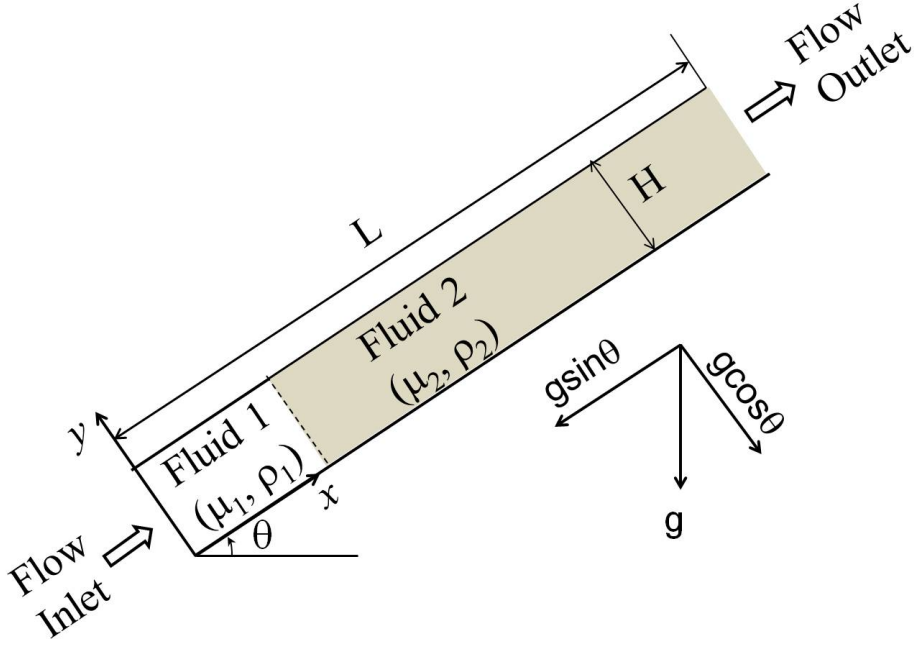


Figure 4.1: Schematic showing the geometry (not to scale) and initial flow configuration. The inlet and outlet are located at $x = 0$ and $x = L$, respectively. The aspect ratio of the channel, L/H , is 48. Initially the channel is filled with fluids ‘1’ and ‘2’ from $0 \leq x \leq 5$ and $5 \leq x \leq L$ of the channel, respectively.

In order to demonstrate the dynamics, a flow configuration (displacing and displaced fluids with leading and trailing edges) at a typical time is shown in Fig. 4.2(a). In Fig. 4.2(b), the spatio-temporal diagram of $\int_0^H \phi dy$ is plotted, which provides the location of the leading and trailing fronts at all times.

4.2 Results and discussion

4.2.1 Grid independency test

We begin presenting our results in Fig. 4.3(a) by first plotting the temporal variation of the dimensionless volume of fluid ‘2’, M_t/M_0 , for $At = 0.2$, $m = 2$, $Fr = 2.236$, $Re = 100$, $Ca = 0.263$ and $\theta = 45^\circ$. Here, M_t is defined as $\int_0^L \int_0^H \frac{\phi - \phi_1}{\phi_2 - \phi_1} dx dy$. Thus, M_0 denotes the volume of fluid ‘2’ initially occupying the channel ($M_0 \equiv \frac{\phi_2 - \phi_1}{\phi_2 - \phi_1} LH$). The parameter values are chosen to correspond to a situation where a heavier fluid is displaced by a fluid of lower density and viscosity. In this case, one would expect

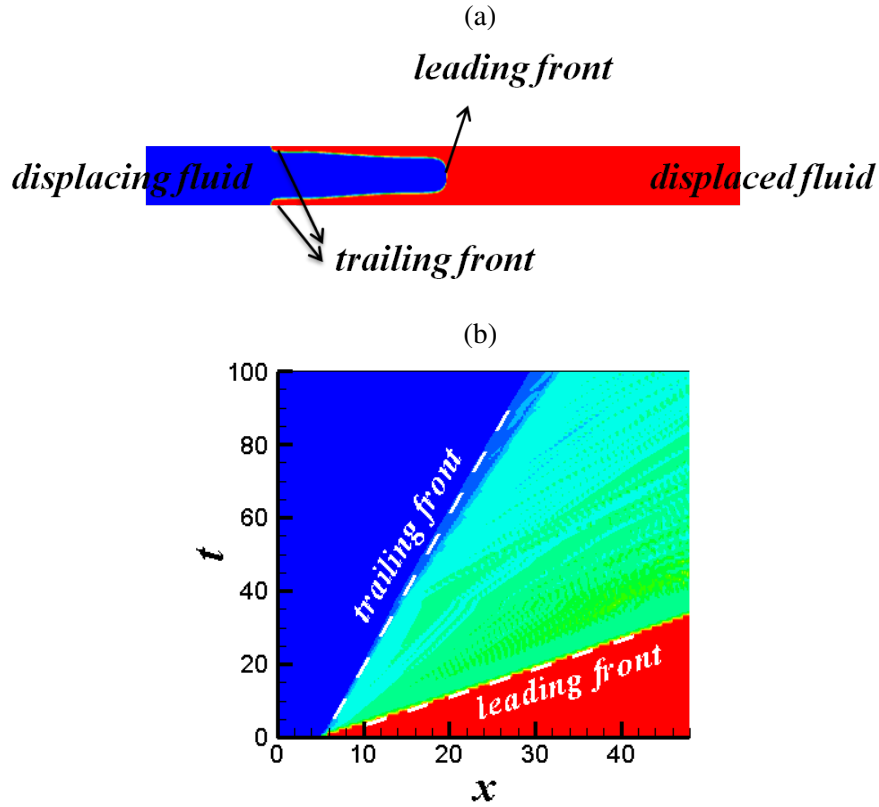


Figure 4.2: (a) Contour showing the penetrating finger and the leading and trailing fronts, (b) the spatio-temporal diagram of $\int_0^H \phi dy$ in time versus x plane showing the leading and the trailing front regimes. The plots are for a particular set of parameters.

the flow to be destabilized because of viscosity contrast and via a Rayleigh-Taylor (RT) instability. Inspection of Fig. 4.3(a) reveals that M_t/M_0 undergoes an almost linear decrease at the earlier stages of the flow due to its displacement by fluid ‘1’. The slope of the curve during this linear stage is close to that of the line represented by $1 - tH/L$ corresponding to a plug flow displacement of fluid ‘2’ with a sharp interface separating the fluids. This is expected due to the conservation of mass of the fluids entering and leaving the channel. Previously in a miscible system, Sahu *et al.* (2009b) observed that slope of M_t/M_0 versus time plot is steeper than that of the plug flow line ($1 - tH/L$), i.e the actual displacement rate is higher than that of the plug flow. This is attributed to the miscibility effects. In miscible system along with the removal of fluid from the outlet, the flow is associated with phase change of fluid ‘2’ to fluid ‘1’ (which does not occur in immiscible flows). Thus, the displacement rate in the present study is slower than that of miscible flows [Sahu *et al.* (2009b)]. At approximately $t = 38$ when the ‘front’ of the displacing fluid ‘1’ reaches the end of simulation domain, as shown in Fig. 4.4, a transition to a different linear regime occurs; the slope of the M_t/M_0 variation in this regime is much smaller than in the first period, indicating slower displacement process. Also shown in Fig. 4.3(a) are results with different grids, which demonstrate convergence upon mesh refinement.

The spatio-temporal diagram of $\int_0^H \phi dy$ in time versus x plane is plotted in Fig. 4.3(b) for 4608×98 grid. The spatio-temporal diagrams generated using 3072×66 and 6144×130 grids look the same as that shown in Fig. 4.3(b). It can be seen that the positions of the leading and the trailing ‘fronts’ separating the two fluids exhibit a linear dependence on time. The slopes of the bottom and top white dashed lines

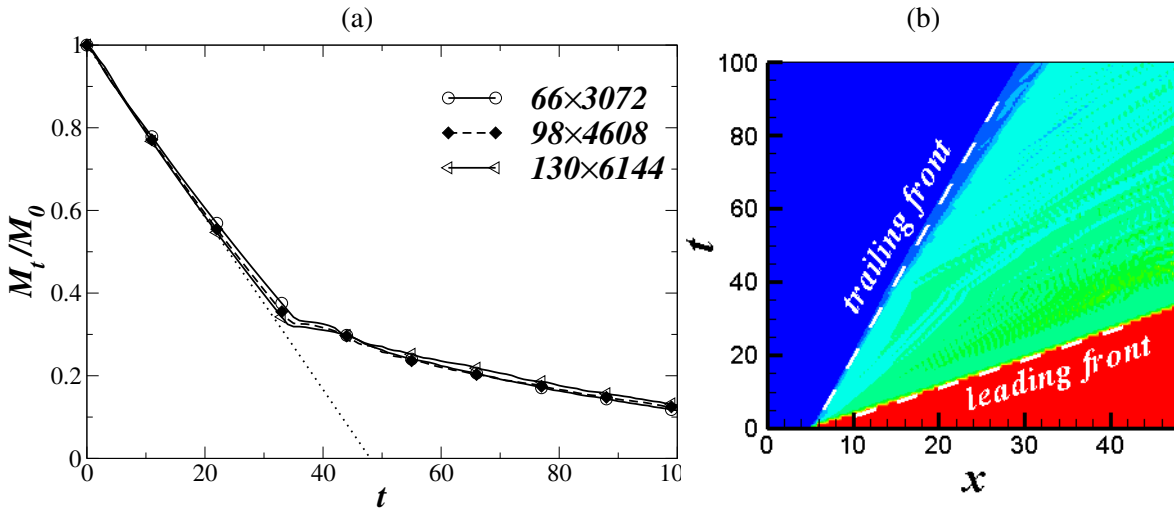


Figure 4.3: (a) Variation of volume fraction of the displaced fluid (M_t/M_0) with time obtained using different mesh densities, and (b) the spatio-temporal diagram of $\int_0^H \phi dy$ in time versus x plane for $At = 0.2$, $m = 2$, $Fr = 2.236$, $Re = 100$, $Ca = 0.263$ and $\theta = 45^\circ$. The dotted line in panel (a) represents the analytical solution of the plug-flow displacement, given by $M_t/M_0 = 1 - tH/L$.

represent the velocity of leading (V_l) and trailing (V_t) fronts, respectively. The front velocities obtained using different sets of lattice points are then compared in Table 4.1. It is evident upon inspection of Table 4.1 that the results of the three grids are nearly the same. Therefore for the rest of the calculations, the 4608×98 grid is chosen, balancing accuracy and computational time.

Table 4.1: The velocity of the leading (V_l) and trailing (V_t) fronts for different grid densities. The rest of the parameter values are $At = 0.2$, $m = 2$, $Fr = 2.236$, $Re = 100$, $Ca = 0.263$ and $\theta = 45^\circ$.

Grid	V_l	V_t
3072×66	1.3141	0.2444
4608×98	1.3139	0.2441
6144×130	1.3132	0.2440

The flow dynamics is illustrated in Fig. 4.4, which shows the spatio-temporal evolution of the ϕ contours for the parameters as in Fig. 4.3. The observed flow dynamics is a result of the competition between the imposed pressure-gradient and the axial component of gravity. For the positive angle of inclination considered in this case, these two forces act in opposite directions. The pressure-driven flow induces motion of fluid ‘1’ into the channel, which is opposed by the acceleration of fluid ‘2’ by the $g \sin \theta$ component of the gravity. On the other hand, the component of the gravitational force in the transverse direction, proportional to $g \cos \theta$, acts to segregate the two fluids. This force therefore counteracts the effects caused by the pressure-gradient and the component of the gravitational force in the axial direction. For the set of parameter values considered in this figure, the effects of the gravity component in the transverse direction ($g \cos \theta$) is quite less as compared to the imposed flow. In other words, as the Fr is relatively larger, the gravitational effects are dominated by the inertial force. Thus, the remnants of fluid ‘2’ left behind by the penetrating finger form thin layers adjacent to the upper and lower walls. The lower layer is thicker than the upper one since the denser fluid ‘2’ expectedly settles on the lower channel wall. However, for smaller value of Fr (i.e., for significant gravity effects) it is shown

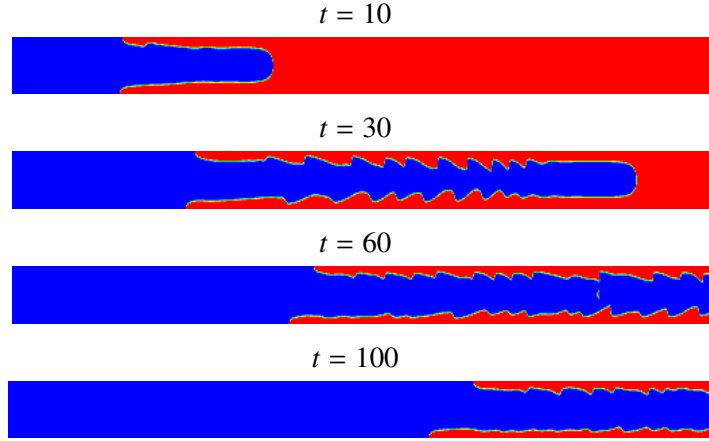


Figure 4.4: Spatio-temporal evolution of the contours of the index function, ϕ for $At = 0.2$, $m = 2$, $Fr = 2.236$, $Re = 100$, $Ca = 0.263$ and $\theta = 45^\circ$.

later that a two-layer flow develops, where the top and bottom parts of the channel are filled with the lighter and heavier fluids, respectively. It can be seen in Fig. 4.4 that the flow is accompanied by the development of the interfacial instabilities of sawtooth-like shape for $t > 10$. It is also observed that the top layer moves faster than the bottom layer.

The effects of viscosity contrasts (m), Atwood number (At) and Froude number (Fr) in a horizontal channel (setting $\theta = 0$) are discussed in the next section.

4.2.2 Horizontal channel

In this section, the effects of viscosity contrast on the flow dynamics for the case of a horizontal channel is discussed first. In Fig. 4.5(a) and (b), the temporal evolutions of the dimensionless measure of the volume of fluid ‘2’, M_t/M_0 for different values of m , are plotted for $At = 0$, $Fr = \infty$ (i.e., in the absence of density contrast and gravity), and $At = 0.3$, $Fr = 0.577$, respectively. The rest of the parameter values are $Re = 100$, $Ca = 0.263$ and $\theta = 0^\circ$. It can be seen in Fig. 4.5(a) and (b) that increasing the value of m decreases the displacement rate. The dotted lines in Fig. 4.5(a) and (b) represent the analytical solution (given by $M_t/M_0 = 1 - tH/L$) which is obtained when fluid ‘1’ displaces fluid ‘2’ as a plug, without forming a finger-like structure. Inspection of Fig. 4.5 reveals that for low viscosity ratio the slope of the curve in the linear region (for $t < 35$ for this set of parameter values) is nearly the same as that of the plug-flow displacement. At approximately $t = 35$, a transition to another linear regime occurs. The displacement rate for $t \geq 35$ decreases significantly as the thin layers of the remnants of fluid ‘2’ at the top and bottom of the channel take longer time to be displaced.

The variations of velocity of the leading (V_l) and trailing (V_t) fronts with viscosity contrasts are shown in Fig. 4.6 (a) and (b), respectively. The rest of the parameter values are the same as those used to generate Fig. 4.5. It can be seen in Fig. 4.6 (a) and (b) that m has a non-monotonic effect on the velocity of the leading front, i.e., increasing m increases V_l for $m \leq 5$, a further increase in m leads to a decrease in the value of V_l . This is in contrast to the miscible system, where the velocity of the leading front increases with increasing m (see Sahu *et al.* (2009a)). It can be seen in Fig. 4.6 (b) that the velocity of the trailing front (V_t) decreases with increasing the viscosity contrasts. This is similar to the finding of my study [Redapangu *et al.* (2012)] in buoyancy-driven flow of two immiscible fluids

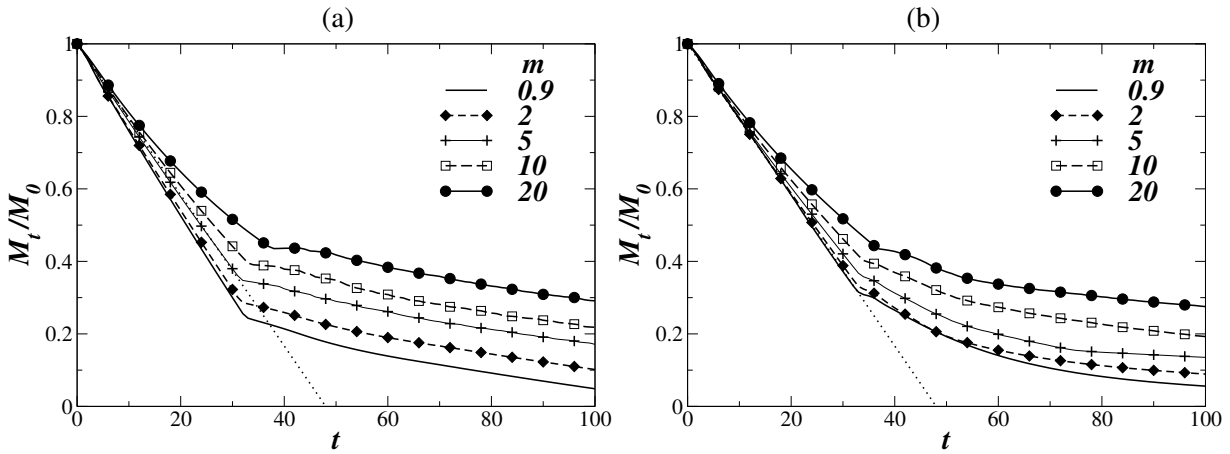


Figure 4.5: Variation of volume fraction of the displaced fluid (M_t/M_0) with time for different values of viscosity ratio, m for (a) $At = 0$ and $Fr = \infty$, and (b) $At = 0.3$, $Fr = 0.577$. The rest of the parameters are $Re = 100$, $Ca = 0.263$ and $\theta = 0^\circ$. The dotted lines in panels (a) and (b) represent the analytical solution of plug-flow displacement, given by $M_t/M_0 = 1 - tH/L$.

which is discussed in Chapter 3. Close inspection of Fig. 4.6 also reveals that the velocity of the leading front in the presence of density contrasts and gravity is higher than that of the no gravity case. However, the velocity of the trailing front (V_t) is smaller in the presence of density contrasts and gravity. This is expected as the gravity acting in the downward direction settles the remnants of fluid ‘2’ at the bottom part of the channel and opposes the motion in the positive axial direction.

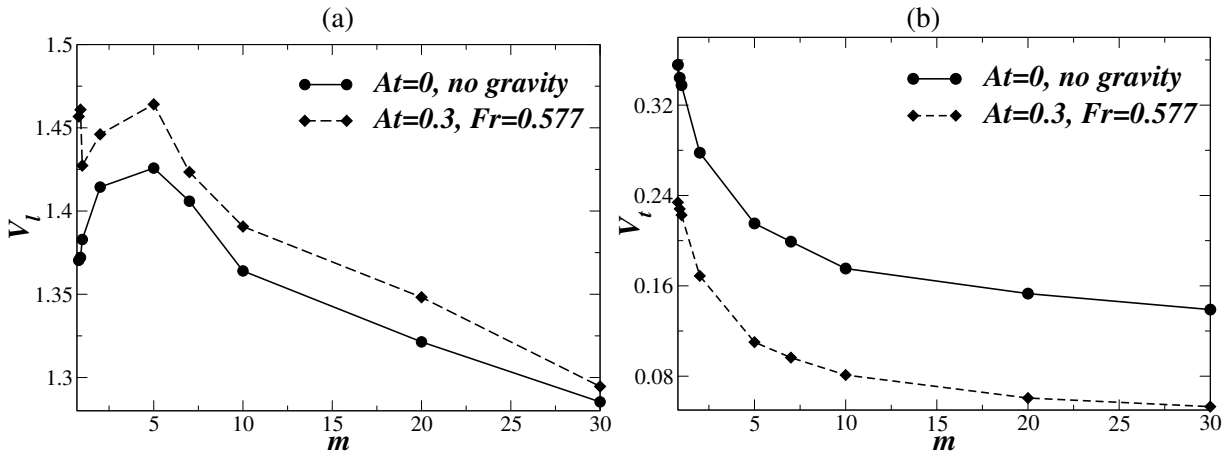


Figure 4.6: Variations of velocities of (a) the leading (V_l) and (b) the trailing (V_t) fronts with viscosity ratio, m . The rest of the parameter values are $Re = 100$, $Ca = 0.263$ and $\theta = 0^\circ$.

The evolution of the ϕ contours for different values of m is plotted in Fig. 4.7 at $t = 15$ and $t = 50$. These two instances of time are considered in order to understand the flow dynamics in the two distinct linear regimes shown in Fig.4.5. In the absence of density contrast, it can be seen in Fig. 4.7(a) that for $m = 0.9$ the flow is fairly stable as in this case a high viscous fluid displaces a less viscous one. $m = 20$ which represents a situation where less viscous fluid displaces a high viscous fluid, the flow becomes considerably unstable accompanied by a wavy interface. This is purely due to the viscosity stratification.

As expected, it can also be seen that the ‘finger’ of the displacing fluid is axially symmetrical in the absence of gravity (see Fig. 4.7(a)). On the other hand, for $Fr = 0.577$ the ‘finger’ of fluid ‘1’ penetrates into the region of fluid ‘2’ with a blunt ‘nose’ (see Fig. 4.7(b)). Unlike in Fig. 4.7(a), it can be seen in Fig. 4.7(b) that the flow becomes unstable due to the RT mechanism even for $m = 0.9$. This ‘finger’ becomes asymmetric: the thickness of the remnants of fluid ‘2’ adjoining the lower wall is larger than that near the upper wall. For $m = 0.9$ the remnants of fluid ‘2’ completely move to the bottom part of the channel at the later times destroying the finger-like structure. The observed asymmetry is brought about by the density contrasts characterized by $At = 0.3$.

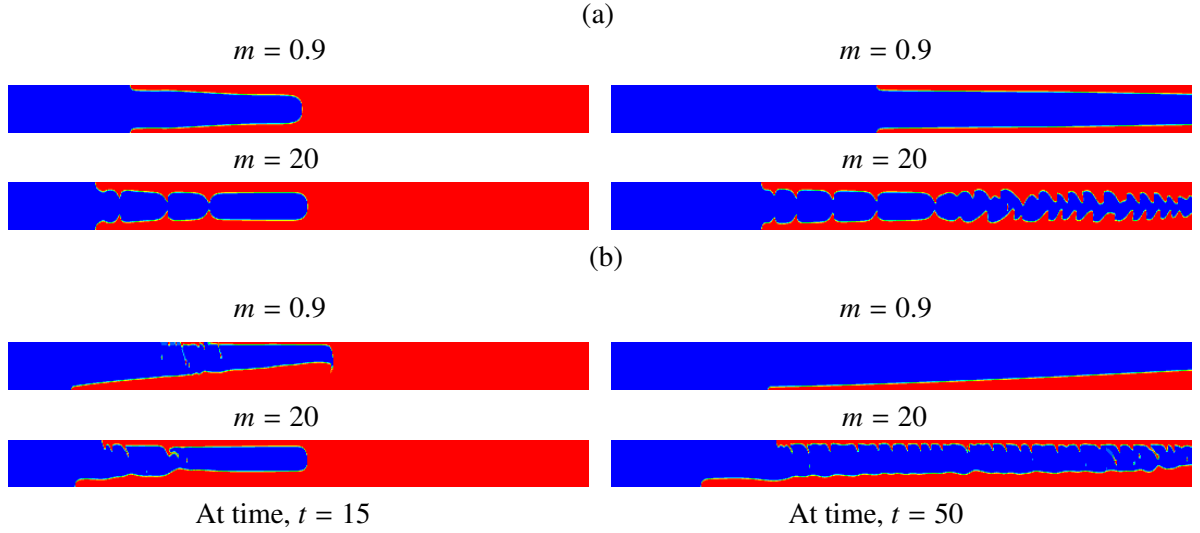


Figure 4.7: The contours of the index function, ϕ at $t = 15$ and $t = 50$ in a horizontal channel ($\theta = 0^\circ$) for two different values of viscosity ratio, m for (a) $At = 0$ and $Fr = \infty$ and (b) $At = 0.3$ and $Fr = 0.577$. The rest of the parameter values are $Re = 100$ and $Ca = 0.263$.

4.2.3 Inclined channel

Next, the effect of the inclination angle (θ) on the displacement process is investigated. In Fig. 4.8, the ϕ field at $t = 30$ is plotted for different angles of inclinations. The rest of the parameter values are $m = 10$, $At = 0.2$, $Fr = 1$, $Re = 100$ and $Ca = 0.263$. The gravity is acting in the vertical direction; thus the two components of the gravity $g\sin\theta$ and $g\cos\theta$ act in the negative axial and negative transverse directions, respectively. It can be seen that the pressure-driven flow induces motion of a ‘finger’ of the less dense and less viscous fluid (fluid ‘1’) into the more dense and more viscous fluid (fluid ‘2’). This is opposed by the flow due to gravitational force in axial direction, which accelerates fluid ‘2’ into fluid ‘1’ in the downward direction. At the same time, the component of the gravitational force in the transverse direction segregates the two fluids. As the ‘finger’ of fluid ‘1’ penetrates into fluid ‘2’, the remnants of fluid ‘2’ left behind form thin layers adjacent to the upper and lower walls, and a two-layer structure is obtained. The interface separating the two fluids becomes unstable forming Yih-type instabilities. The linear stability characteristics of this two-layer flow is discussed in Section 4.3.

In a horizontal channel ($\theta = 0^\circ$), the transverse component of gravity becomes maximum and the axial penetration is only due to the imposed pressure-gradient. In this case, the high density fluid

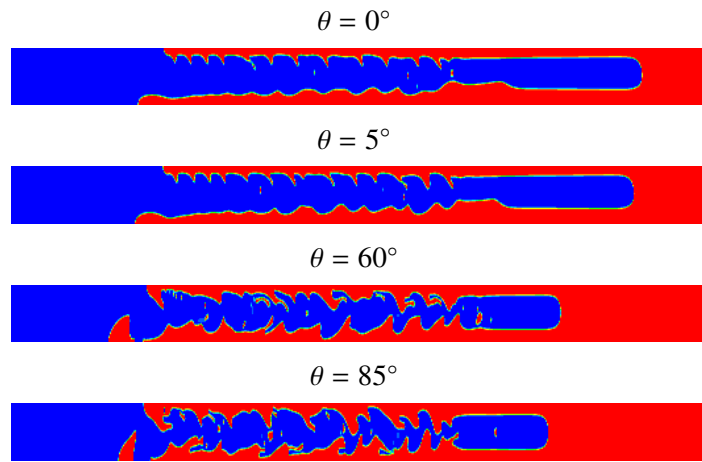


Figure 4.8: The contours of the index function, ϕ at $t = 30$ for different inclination angles. The rest of the parameter values are $m = 10$, $At = 0.2$, $Fr = 1$, $Re = 100$ and $Ca = 0.263$.

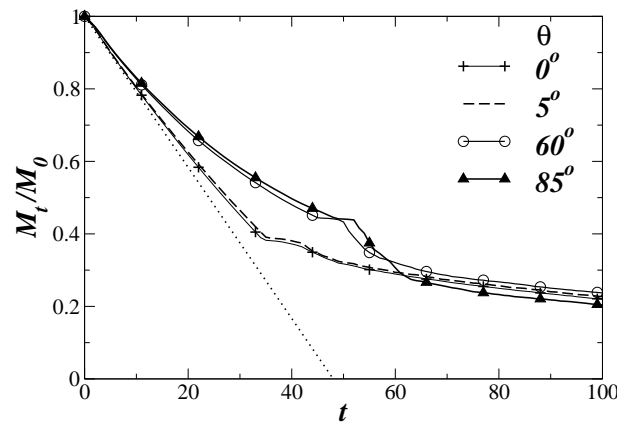


Figure 4.9: The effects of angle of inclination on the variation of the volume fraction of the displaced fluid, (M_t/M_0) with time. The parameters used are $m = 10$, $At = 0.2$, $Fr = 1$, $Re = 100$ and $Ca = 0.263$. The dotted line represents the analytical solutions of the variation of M_t/M_0 for plug-flow displacement, given by $M_t/M_0 = 1 - tH/L$.

(remnants of fluid ‘2’) tries to segregate from the less dense fluid (fluid ‘1’) by moving in the transverse direction into the bottom part of the channel. As a result the lower layer becomes thicker than the upper layer, resulting in an asymmetric ‘finger’ moving in the axial direction. Comparison with Fig. 4.7, which corresponds to a smaller value of Fr , reveals that the thickness of the lower layer increases with decreasing Fr . This is expected as decreasing Fr for a given inclination increases the gravitational influence in the transverse direction, which increases the segregation of the fluids. It can be seen in Fig. 4.8 that increasing θ for a given value of Fr also decreases fluid segregation due to the diminishing role of the gravitational force. Therefore the finger becomes increasingly symmetrical with increasing the angle of inclination (see Fig. 4.8). This also increases the intensity of the interfacial instabilities, which in turn increases the removal rate of fluid ‘2’ in later times (for $t > 60$ for this set of parameter values), as shown in Fig. 4.9.

The spatio-temporal diagrams of $\int_0^H \phi dy$ in time versus x plane are plotted in Fig. 4.10 for different angles of inclination, with the rest of the parameter values kept the same as Fig.4.8 . It can be seen that the speed of the trailing front decreases with increasing the value of θ . This happens because increasing θ

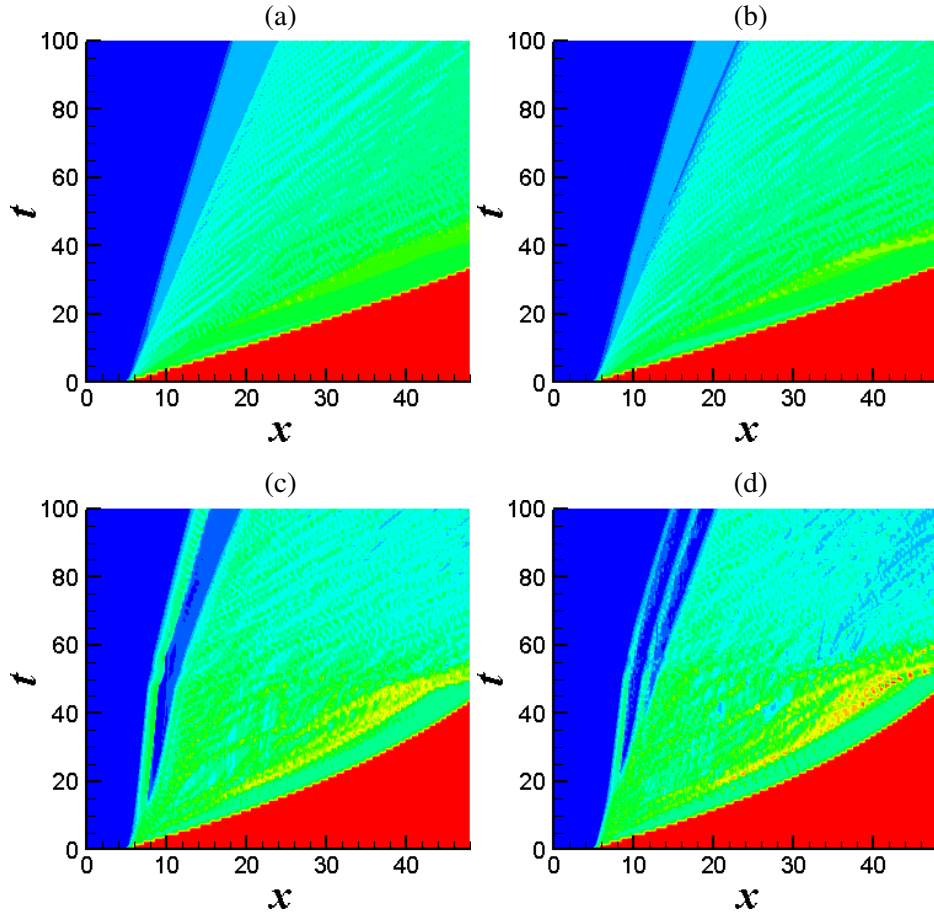


Figure 4.10: The spatio-temporal diagram of $\int_0^H \phi dy$ in time versus x plane for (a) $\theta = 0^\circ$, (b) $\theta = 5^\circ$, (c) $\theta = 60^\circ$ and (d) $\theta = 85^\circ$. The rest of the parameter values the same as those in Fig. 4.8.

increases the gravitational influence ($g \sin \theta$) in the negative axial direction. We found later that a further increase in the gravitational force by decreasing the value of Fr (shown in Section 4.2.4) leads the heavier fluid in the lower layer to move in the opposite direction. It can also be seen that the variation of the location of the leading front tip (boundary separating the red and green regions in Fig. 4.10) is nonlinear for larger angles of inclination, and this nonlinearity is predominant at later times. In contrast, Sahu *et al.* (2009b) observed a constant slope in the x_{rip} (location of the leading front) versus time plot. However, their study was associated with miscible fluids, in which diffusion may have played a role to reduce the nonlinearity as observed in the present study.

Fig. 4.11 shows the vorticity (first panel) and velocity vector (second panel) fields for the parameter values the same as those used to generate Fig. 4.8. It can be seen that the central region contains strong vortical activity. Inspection of Fig. 4.11 also reveals that the level of vortical structures in the central region increases with increasing the angle of inclination as the flow accelerates due to the combined action of the pressure-gradient and the components of the gravity.

The effect of viscosity contrast is investigated in Fig. 4.12, where the contours of the index function, ϕ are shown at different times for different viscosity ratios. It can be seen in Fig. 4.12(a) that the flow for $m < 1$ is associated with the formation of small scale structures. It is well known that the flow for $m < 1$ is stable without density contrast and gravity [Joseph *et al.* (1997); Saffman & Taylor (1958)] (also see Fig. 4.7). Thus instabilities in this case are due to the RT mechanism as the high dense fluid

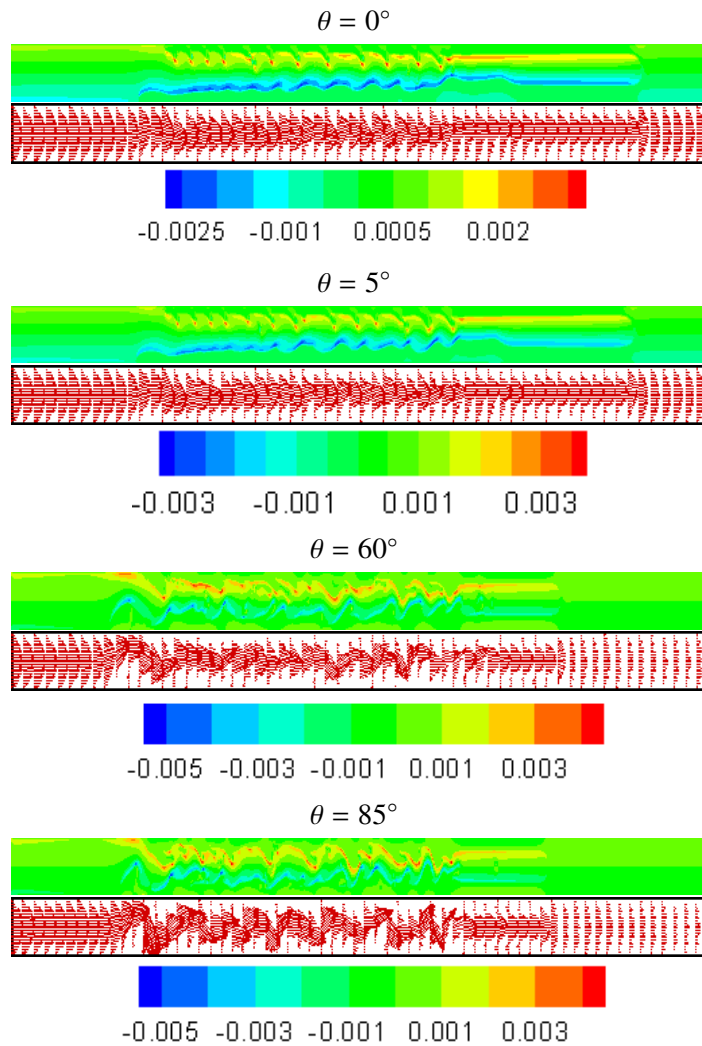


Figure 4.11: The vorticity (first panel) and velocity vectors (second panel) fields for the same parameter values as those used to generate Fig. 4.8. The color-maps for the vorticity contours are shown as third panel.

moves in the negative axial direction while the finger of fluid ‘1’ penetrates inside the channel due to the imposed pressure gradient. The back flow of the denser fluid is clearly evident in Fig. 4.13(a), where the spatio-temporal diagram of $\int_0^H \phi dy$ is plotted in time versus x plane. It can be seen in Fig. 4.12 that the flow becomes more coherent with increasing viscosity ratio. Inspection of Fig. 4.13(b) and (c) also reveals that there is no back flow for higher viscosity ratio. This is due to the increase in wall shear stress with increasing viscosity ratio, which prevents the motion of the layer of fluid ‘2’ in the backward direction. Thus, the rate of displacement of fluid ‘2’ also decreases with increase in viscosity ratio, as shown in Fig. 4.14.

In Fig. 4.15, the effect of surface tension on the ϕ fields is investigated by considering three values of capillary number, Ca at $t = 30$. The rest of the parameter values used to generate this plot are $m = 5$, $At = 0.2$, $Fr = 1$, $Re = 100$ and $\theta = 45^\circ$. Inspection of Fig. 4.15 reveals that the surface tension makes the flow dynamics coherent by stabilizing the short wavelength waves [Yih (1967)], and decreasing value of Ca (which corresponds to increase in surface tension), increases the stabilizing influence of the flow.

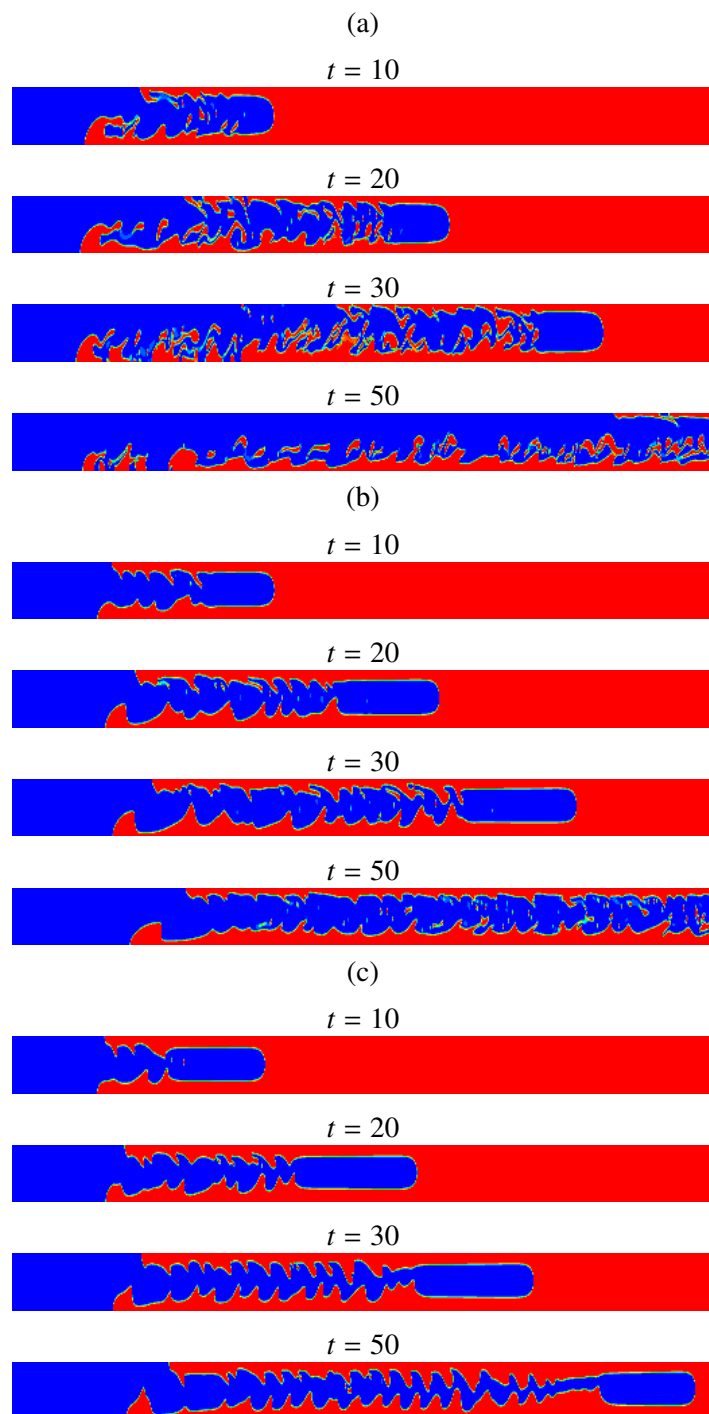


Figure 4.12: Spatio-temporal evolution of contours of the index function, ϕ for (a) $m = 0.8$, (b) $m = 10$ and (c) $m = 30$. The rest of the parameters are $At = 0.2$, $Fr = 1$, $Re = 100$, $\theta = 45^\circ$ and $Ca = 0.263$.

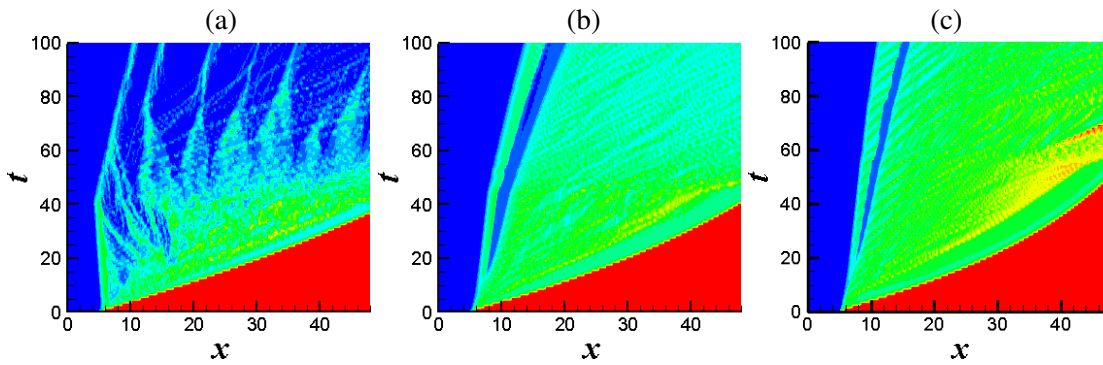


Figure 4.13: The spatio-temporal diagram of $\int_0^H \phi dy$ in time versus x plane for (a) $m = 0.8$, (b) $m = 10$ and (c) $m = 30$. The rest of the parameter values are the same as those used to generate Fig. 4.12.

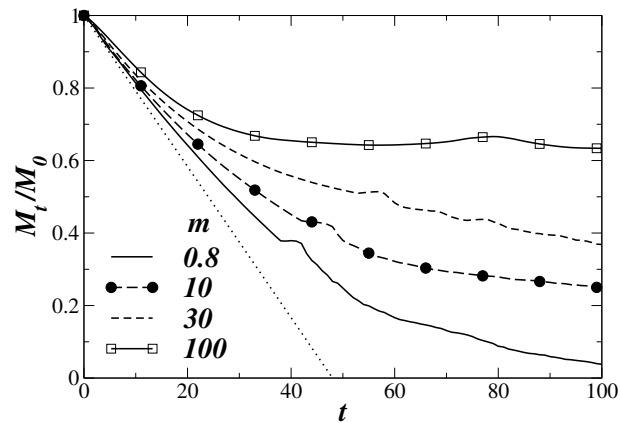


Figure 4.14: Effects of viscosity ratio, m on variation of the volume fraction of the displaced fluid, (M_t/M_0) with time. The rest of the parameter values are the same as those used to generate Fig. 4.12. The dotted line represents the analytical solution for plug-flow displacement, given by $M_t/M_0 = 1 - tH/L$.

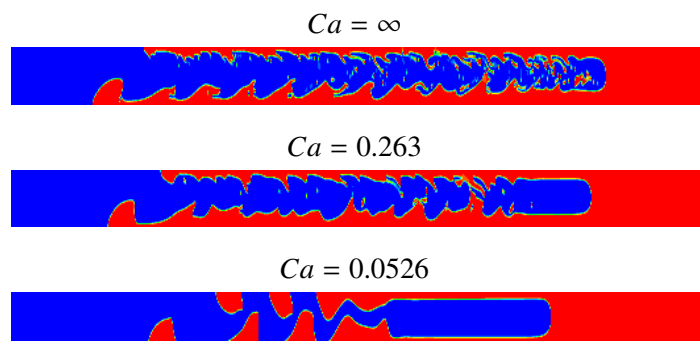


Figure 4.15: The contours of the index function, ϕ for different values of capillary number at $t = 30$. The rest of the parameter values are $m = 5$, $At = 0.2$, $Fr = 1$, $Re = 100$ and $\theta = 45^\circ$.

4.2.4 Near horizontal channel

In this section, the effects of Froude number in a near horizontal channel ($\theta = 5^\circ$) are presented. Fig. 4.16(a) and (b) show the variation of the normalized front velocity, FrV_l with Froude number, Fr for $m = 1$ and $m = 10$, respectively. Two values of Atwood number, $At = 0.2$ and 0.04 are considered. The rest of the parameter values are $Re = 100$ and $Ca = 0.263$. It can be seen in Fig. 4.16(a) and (b) that the results for both the values of At collapse on a single curve; these are also independent of viscosity ratio. This suggests that for the parameter values considered, the velocity of the leading front can be obtained by balancing the buoyancy (proportional to $(\rho_2 - \rho_1)g$) and imposed pressure force with the inertial force. The dashed lines in Fig. 4.16(a) and (b) represent the best fitted polynomial, given by $FrV_l = 0.38 + 0.665Fr + 0.3534Fr^2$. The first and second terms on the right hand side correspond to the buoyancy and imposed pressure forces, respectively. The leading term in the best fit curve compares well with that of Sahu & Vanka (2011), who studied the buoyancy-driven “lock-exchange flow” of two immiscible fluids in an inclined channel and that of Taghavi *et al.* (2012) for miscible displacement flow in a near horizontal channel. However, in a purely buoyancy-driven flow of two miscible fluids in an inclined pipe, Séon *et al.* (2005) determined the leading term ($= 0.7$) by balancing the buoyancy with the inertial force. This difference in the value of the leading term is attributed to the cylindrical geometry considered by Séon *et al.* (2005).

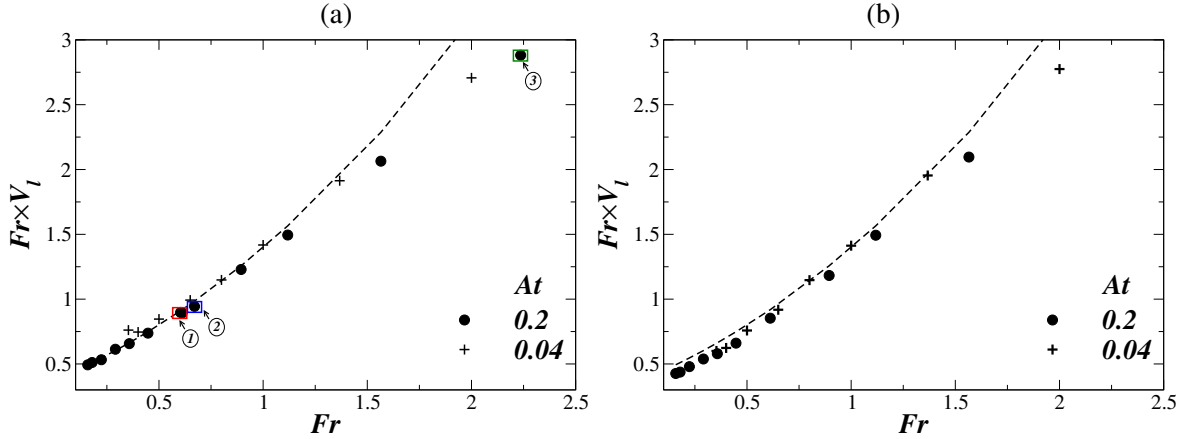


Figure 4.16: Variation of the normalized front velocity, FrV_l with Froude number, Fr for (a) $m = 1$ (b) $m = 10$. The rest of the parameter values are $Re = 100$, $Ca = 0.263$ and $\theta = 5^\circ$. The dashed line is the best fitted polynomial, given by $FrV_l = 0.38 + 0.665Fr + 0.3534Fr^2$. The red, blue and green square boxes in panel (a) correspond to $Fr = 0.604$, $Fr = 0.671$ and $Fr = 2.24$, respectively.

Next, the three points marked with points 1, 2 and 3 in Fig. 4.16(a), are considered which correspond to $Fr = 0.604$, $Fr = 0.671$ and $Fr = 2.24$, respectively. The spatio-temporal diagrams of $\int_0^H \phi dy$ in $x-t$ plane are plotted for $Fr = 0.604$, $Fr = 0.671$ and $Fr = 2.24$ in Figs. 4.17(a), (b) and (c), respectively. The rest of the parameter values are the same as Fig. 4.16. It can be seen in Fig. 4.17(a) that the trailing front moves upstream for $0 \leq t \leq 60$ and then moves in the downstream direction for $t > 60$. This is termed as “temporary back flow” by Taghavi *et al.* (2011). For $Fr = 2.24$, it can be seen that the trailing front move in the downstream direction for any $t > 0$ (“instantaneous displacement”). It can be observed that $Fr = 0.671$ is a marginal state, where the trailing front remains stationary for some time before moving in the downstream direction. This is termed as “stationary back flow” by Taghavi *et al.* (2011). Thus for $Fr > 0.671$, a temporary lock-exchange type of flow is observed for this set of parameter values.

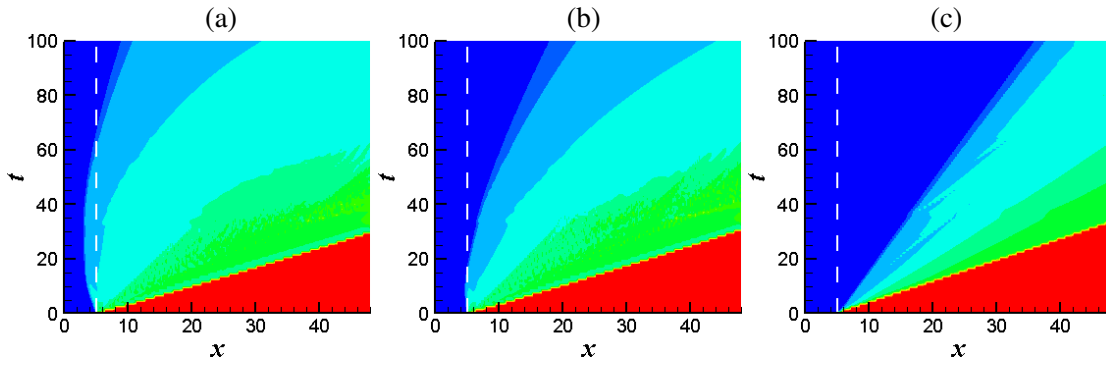


Figure 4.17: The spatio-temporal diagram of $\int_0^H \phi dy$ in time versus x plane for (a) $Fr = 0.604$, (b) $Fr = 0.671$ and (c) $Fr = 2.24$ for the parameters $At = 0.2$, $m = 1$, $Re = 100$, $\theta = 5^\circ$ and $Ca = 0.263$. The white dashed lines represent the initial location of the interface ($x = 5$).

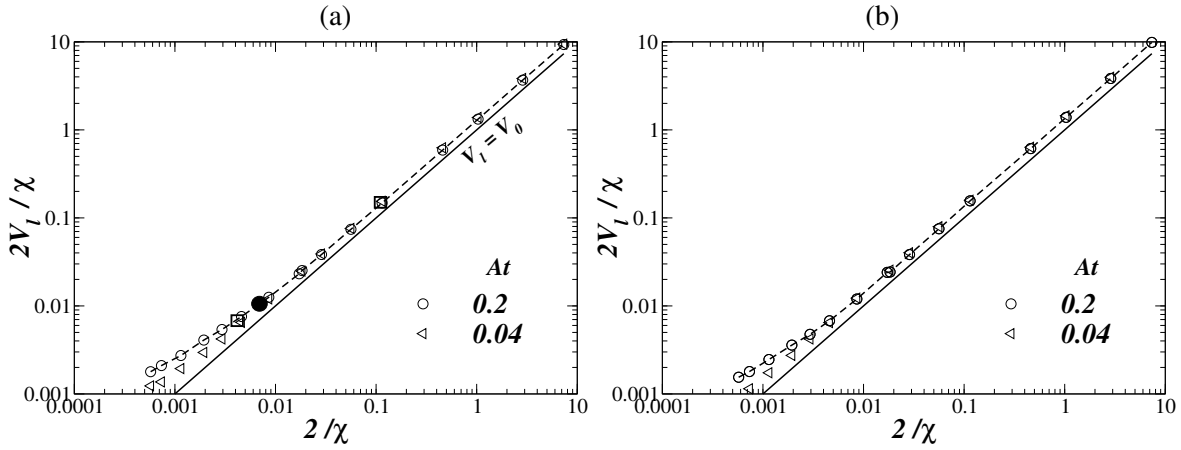


Figure 4.18: Normalized front velocity as a function of normalized Fr , for (a) $m = 1$ and (b) $m = 10$ where $\chi = 2Re \sin \theta / At Fr^2$. The rest of the parameters are $Re = 100$, $\theta = 5^\circ$ and $Ca = 0.263$. The solid line represents the line $V_l = V_0$. The filled circle in (a) corresponds to $Fr = 0.671$, the squares to the left and the right of this filled circle correspond to $Fr = 0.604$ and $Fr = 2.24$, respectively.

As suggested by Taghavi *et al.* (2012), in the exchange flow dominated regime, it is possible to derive a single dimensionless parameter, $\chi (\equiv 2Re \sin \theta / At Fr^2)$ by balancing the buoyancy force in the axial direction with the imposed pressure force. The normalized front velocity ($2V_l/\chi$) is plotted against $2/\chi$ in Fig. 4.18(a) and (b) for $m = 1$ and 10, respectively. The filled circle in (a) corresponds to $\chi = 193.6$, and the squares below and above this filled circle correspond to $\chi = 293.1$ and $\chi = 17.4$, respectively. It can be seen that for $\chi > \chi_{cr} (= 193.6)$ the results are diverged from the $V_l = V_0$ line, which corresponds to pure displacement flow. For the set of parameter values considered, the value of χ_{cr} corresponds to $Fr = 0.671$ (see Fig. 4.17(b)). Thus, the trailing front has a tendency to move in the downstream direction (back flow) for $\chi > \chi_{cr}$, whereas it moves only in the positive axial direction for $\chi < \chi_{cr}$ (no back flow). In case of miscible displacement flows in a near horizontal pipe, Taghavi *et al.* (2012) found the value of χ_{cr} to be 116.32. This difference is also due to the cylindrical geometry considered by these authors. The result seems to be invariant for $m = 10$.

4.3 Linear stability analysis

The linear stability analysis of the three-layer channel flow which can be obtained when the elongated ‘finger’ of fluid ‘1’ penetrates into the bulk of fluid ‘2’ (as discussed in Chapter 1) is considered. The base state whose linear stability characteristics will be analyzed corresponds to a parallel, fully-developed flow in which the two fluids are separated by flat interfaces, with fluid ‘1’ located in the region $-h^0 \leq y \leq h^0$, as shown in Fig. 4.19. We assume $P_1 = P_2 \equiv P$ and the pressure distribution is linear in x .

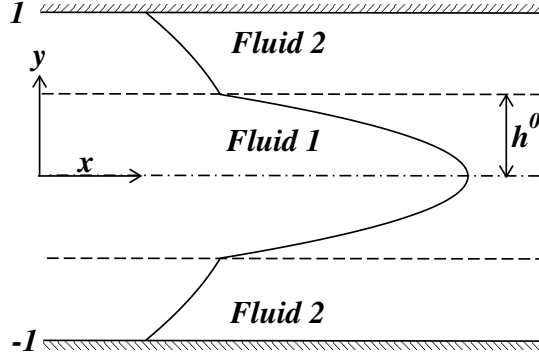


Figure 4.19: Schematic showing the geometry and initial condition of the flow. Also shown here is profile of the steady, streamwise velocity component generated with $m = 10$ and $h^0 = 0.5$.

By assuming symmetry in the wall-normal direction, the bottom part of the channel is considered for the linear stability analysis. The velocity distribution is given by:

$$U_1 = \frac{1}{2} \frac{dP}{dx} y^2 + c_1 y + c_2, \quad (4.1)$$

$$U_2 = \frac{1}{2m} \frac{dP}{dx} y^2 + \frac{c_3 y}{m} + c_4. \quad (4.2)$$

$$\text{and } \int_0^h U_1 dy + \int_h^1 U_2 dy = 1. \quad (4.3)$$

The pressure gradient, dP/dx and the integration constants, c_1 , c_2 , c_3 , and c_4 are obtained using the no-slip condition at the lower wall, symmetric boundary conditions across the channel centerline, and demanding continuity of velocity and stress at the interface. Eq. (4.3) represents a condition of constant volumetric flow rate, Q , chosen to be one, and the half channel width has been used as a length scale in this section. A typical velocity profile for $m = 10$ and $h^0 = 0.5$ is shown in Fig. 4.19.

The stability of the base state characterized by U_1 and U_2 to infinitesimal, two-dimensional (2D) disturbances are investigated using a normal mode analysis by expressing each flow variable as the sum of a base state and a 2D perturbation:

$$u_k(x, y, t) = U_k(y) + \hat{u}_k(x, y, t) \quad (4.4)$$

$$v_k(x, y, t) = \hat{v}_k(x, y, t) \quad \text{and} \quad (4.5)$$

$$p_k(x, y, t) = P + \hat{p}_k(x, y, t), \quad (4.6)$$

with $(k = 1, 2)$. Similarly h can be expanded as follows

$$h(x, t) = h^0 + \hat{h}(x, t), \quad (4.7)$$

where the superscript ‘0’ designates base state quantities. Substitution of Eqs. (4.4) to (4.7) into the Navier-Stokes and continuity equations, subtraction of the base state equations and subsequent linearisation yields the linear stability equations in terms of primary variables. These equations are then re-expressed in terms of the stream-function, $(u_k, v_k) = (\partial\Psi_k/\partial y, -\partial\Psi_k/\partial x)$ ($k = 1, 2$) and the decomposition $\Psi(x, y, t) = \Phi(y)e^{i(\beta x - \omega t)}$ is imposed, whence,

$$\hat{u}_k(x, y, t) = \Phi'_k(y)e^{i(\beta x - \omega t)}, \quad (4.8)$$

$$\hat{v}_k(x, y, t) = -i\beta\Phi_k(y)e^{i(\beta x - \omega t)}, \quad (4.9)$$

$$\hat{p}_k(x, y, t) = p_k(y)e^{i(\beta x - \omega t)}, \quad \text{and} \quad (4.10)$$

$$\hat{h}(x, t) = \eta e^{i(\beta x - \omega t)}. \quad (4.11)$$

Then eliminating the pressure perturbations from the resultant equations, yields the following coupled Orr-Sommerfeld-type equations.

$$i\beta Re \left[(\Phi'_1 - \beta^2\Phi_1)(U_1 - c) - \Phi_1 U''_1 \right] = [\Phi''''_1 - 2\beta^2\Phi''_1 + \beta^4\Phi_1] \quad (4.12)$$

$$i\beta Re \left(\frac{1 + At}{1 - At} \right) \left[(\Phi''_2 - \beta^2\Phi_2)(U_2 - c) - \Phi_2 U''_2 \right] = m [\Phi''''_2 - 2\beta^2\Phi''_2 + \beta^4\Phi_2]. \quad (4.13)$$

Here, the prime represents differentiation with respect to y , and Φ_k and η denote the amplitudes of the streamfunction and interfacial perturbation, respectively; β is a axial real wavenumber, $\omega (\equiv \beta c)$ is a complex frequency, wherein c is a complex phase speed of the disturbance. Note that $(1 + At)/(1 - At)$ represents the density ratio, ρ_1/ρ_2 . In the temporal stability analysis considered in this section, $\omega_i > 0$ indicates the presence of a linear instability.

The eigenvalue c and the eigenfunctions Φ_1 and Φ_2 are obtained via solution of Eqs. (4.12) and (4.13) subject to the following boundary conditions: the no-slip and no-penetration conditions at the upper wall:

$$\Phi_2 = \Phi'_2 = 0, \quad \text{at } y = -1; \quad (4.14)$$

and either

$$\Phi'_1 = \Phi''''_1 = 0 \quad \text{or} \quad \Phi_1 = \Phi'_1 = 0 \quad \text{at } y = 0 \quad (\text{centerline}), \quad (4.15)$$

which are appropriate for symmetric and anti-symmetric modes, respectively. Our results (not shown) reveal that the symmetric mode is dominant for the range of parameters considered in the present work. Consequently, all of the results presented below correspond to symmetric mode exclusively. Using the continuity of the velocity and stress components for the disturbance in the axial and the wall-normal directions at the interface, along with the kinematic boundary condition, we obtained:

$$\Phi_1 = \Phi_2, \quad (4.16)$$

$$\Phi'_1 - \Phi'_2 + \eta(U'_1 - U'_2) = 0, \quad (4.17)$$

$$m(\Phi''_2 + \beta^2\Phi_2) - (\Phi''_1 + \beta^2\Phi_1) + \frac{(U''_1 - mU''_2)}{(U_1 - c)} = 0, \quad (4.18)$$

$$\begin{aligned} & -i\beta Re \left[\Phi'_1(c - U_1) + \Phi_1 U'_1 \right] + i\beta \left(\frac{1 + At}{1 - At} \right) Re \left[\Phi'_2(c - U_2) + \Phi_2 U'_2 \right] - (\Phi''''_1 - \beta^2\Phi'_1) + \\ & m(\Phi''''_2 - \beta^2\Phi'_2) + 2\beta^2\Phi'_1 - 2m\beta^2\Phi'_2 = \left(\frac{\beta^2}{Ca} + \mathcal{G} \right) i\beta \frac{(\Phi'_1 - \Phi'_2)}{(U'_2 - U'_1)}, \end{aligned} \quad (4.19)$$

where η is given by

$$\eta = \Phi_1 / (c - U_1)|_h = \Phi_2 / (c - U_2)|_h. \quad (4.20)$$

Here, $\mathcal{G} \equiv 2ReAt^2 / Fr^2(At - 1)$. The stability analysis conducted here is similar to the one given in Sahu *et al.* (2007), Sahu & Matar (2010, 2011). We recover Eqs. (4.12) - (4.20) from the stability equations and boundary conditions given in Sahu & Matar (2010) for Newtonian fluids.

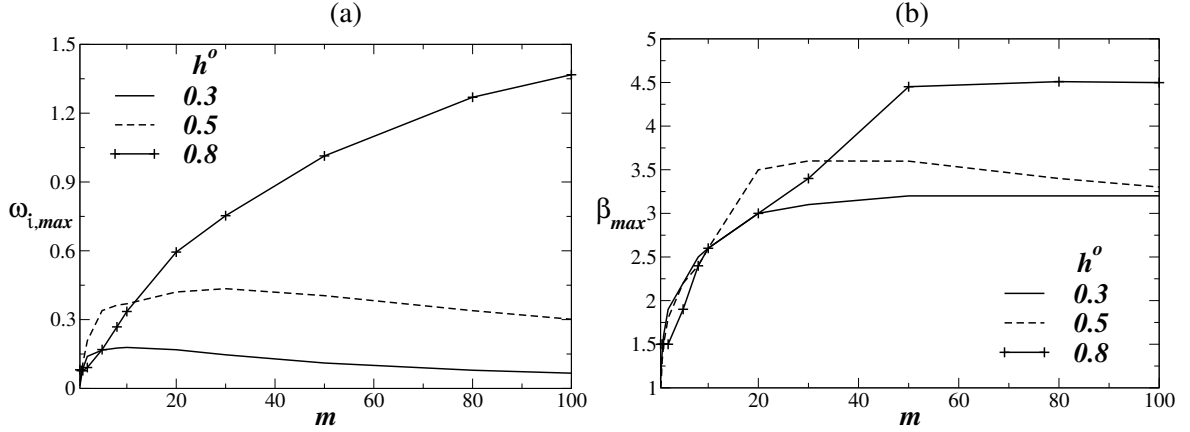


Figure 4.20: Variation of (a) maximal growth rate, $\omega_{i,max}$ (a) axial wavenumber associated with the most dangerous mode, β_{max} with viscosity ratio, m . The rest of the parameter values are $Re = 100$, $At = 0.1$, $Fr = 1$, $\theta = 0^\circ$ and $Ca = 0.263$.

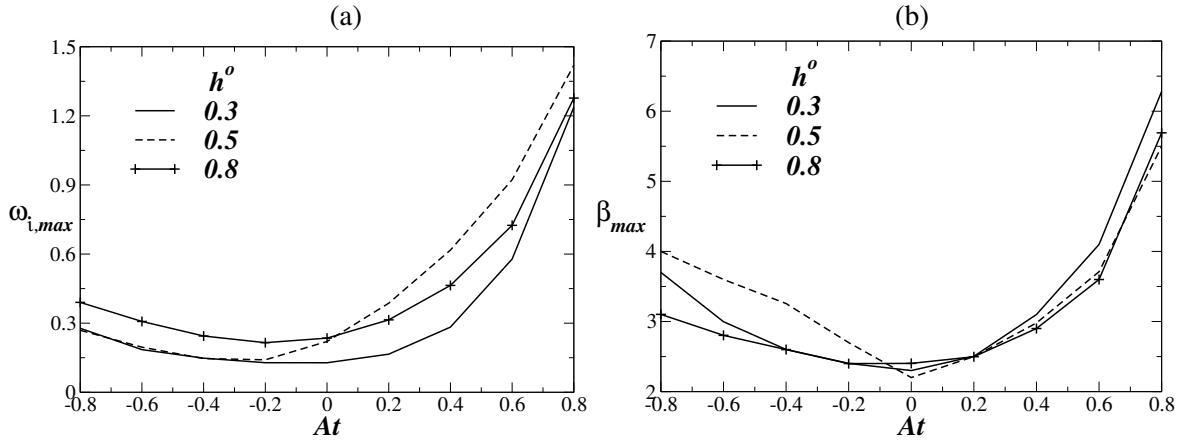


Figure 4.21: Variation of (a) maximal growth rate, $\omega_{i,max}$ (a) axial wavenumber associated with the most dangerous mode, β_{max} with Atwood number At . The rest of the parameter values are $Re = 100$, $m = 10$, $Fr = 1$, $\theta = 0^\circ$ and $Ca = 0.263$.

The effects of varying the viscosity ratio (m), Atwood number (At), Froude number (Fr) and capillary number (Ca) on the linear stability characteristics are discussed next. In Fig. 4.20(a) the variation of the maximal growth rate, $\omega_{i,max}$, and axial wavenumber associated with the most dangerous mode, β_{max} are plotted against the viscosity ratio. It can be seen in Fig. 4.20(a) that $\omega_{i,max}$ increases and then decreases with increasing the value of viscosity ratio, m . It can be seen in Fig. 4.20(b) that the axial wavenumber associated with the most dangerous mode, β_{max} increases with increasing the viscosity ratio. This prediction from the linear stability analysis is in agreement with our numerical simulation results plotted in Figs. 4.7 and 4.12. Similarly, the variation of $\omega_{i,max}$ and β_{max} with Atwood number, At are plotted in Fig. 4.21(a) and (b), respectively. Inspection of this figure reveals that the disturbance

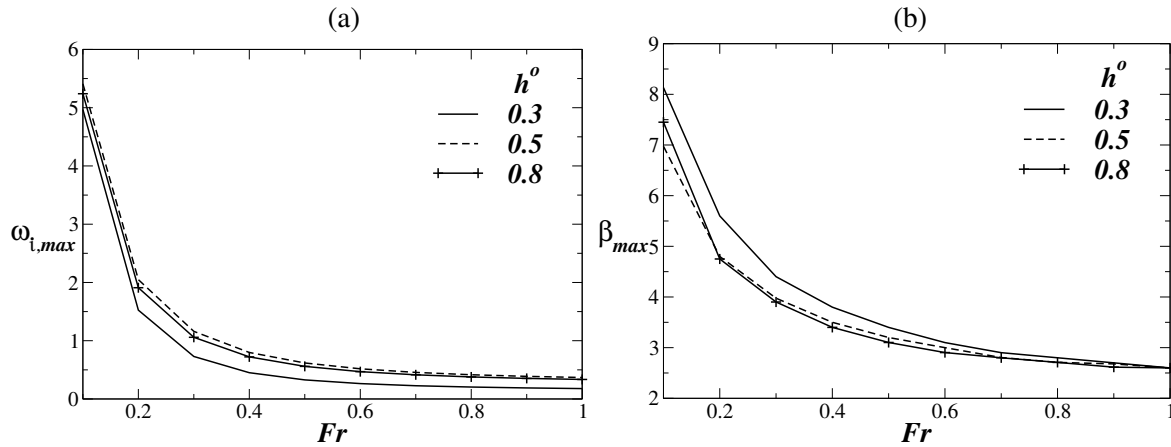


Figure 4.22: Variation of (a) maximal growth rate, $\omega_{i,max}$ (a) axial wavenumber associated with the most dangerous mode, β_{max} with Froude number, Fr . The rest of the parameter values are $Re = 100$, $m = 10$, $At = 0.1$, $\theta = 0^\circ$ and $Ca = 0.263$.

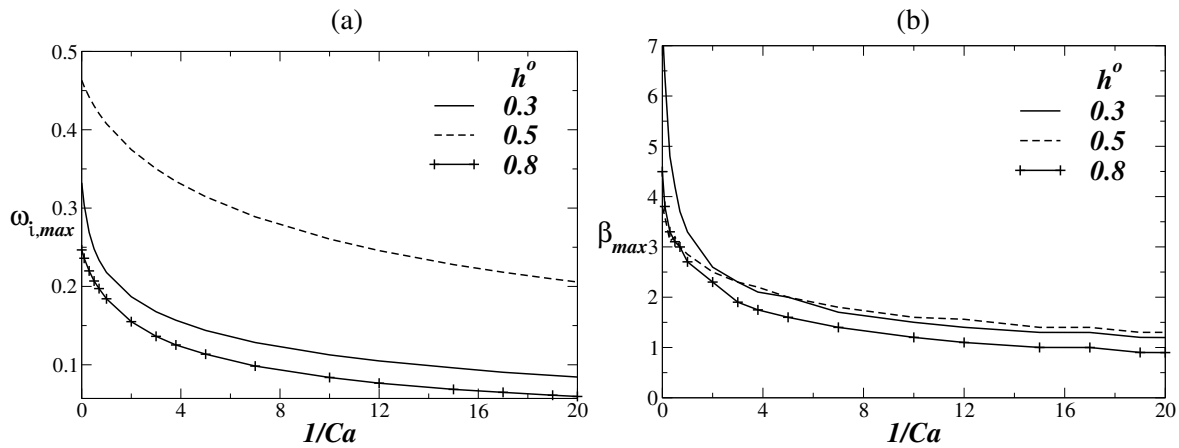


Figure 4.23: Variation of (a) maximal growth rate, $\omega_{i,max}$ (a) axial wavenumber associated with the most dangerous mode, β_{max} with capillary number, Ca . The rest of the parameter values are $Re = 100$, $m = 10$, $At = 0.1$, $\theta = 0^\circ$ and $Fr = 1$.

growth rate is minimum when there is no density contrast, and increasing or decreasing the ratio of the density of the annular to the core fluid increases the growth rate. A similar behavior is also observed for the variation of axial wavenumber of the most dangerous mode with At . It can be seen in Figs. 4.22 and 4.23 that $\omega_{i,max}$ and β_{max} monotonically decrease with increasing Froude number and inverse capillary number. The decrease in β_{max} with the inverse capillary number, suggests that the wavelength of the most dangerous mode increases with increasing surface tension. A similar result was also obtained by several researchers (e.g. Selvam *et al.* (2007)). This behavior can be clearly evident in Fig. 4.15 where we can see that decreasing Ca (increasing surface tension) reduces the shortwave length small scale structures. An energy budget analysis similar to that given in Sahu & Matar (2010) (not shown) predicts that the most dangerous modes are interfacial ones. Thus these instabilities are of Yih-type as we do not see any 'roll-up' phenomenon in the present study.

4.4 Summary

The pressure-driven displacement flow of two immiscible fluids in an inclined channel in the presence of viscosity and density gradients is investigated by using a multiphase lattice Boltzmann method. The effects of viscosity ratio, density ratio characterized by Atwood number, gravity characterized by Froude number and surface tension characterized by capillary number are examined. The effect of channel inclination is investigated in terms of flow structures, front velocities and displacement rates. Our results indicate that increasing viscosity ratio decreases the displacement rate, and has a non-monotonic effect on the velocity of the leading front. However, the velocity of the trailing edge decreases with increasing the viscosity ratio. We found that the displacement rate of the thin-layers (after the leading front crossed the simulation domain) increases with increasing the angle of inclination. This is due to the increase in the intensity of the interfacial instabilities with increasing the inclination angle, which helps in cleaning the channel. Our results predict the front velocity of the “lock-exchange flow” of two immiscible fluids in the exchange flow dominated regime. This is also consistent with the finding of Séon *et al.* (2005); Taghavi *et al.* (2012) for exchange flow of miscible fluids at high Peclet number. A linear stability analysis of a three-layer system predicts the behavior of the numerical simulation qualitatively. We also observe that the instabilities are of Yih-type.

CHAPTER 5

Pressure-driven displacement flow in a square duct

In this chapter, the displacement flow of a liquid originally occupying a square duct by another immiscible liquid of different density and viscosity, which is injected from the inlet of the channel is investigated. This is an extension of our previous work of the displacement flow in a two-dimensional (2D) channel which was presented in Chapter 4. As the three-dimensional simulations are computationally very demanding, we used our GPU based LBM solver, which is 25-times faster than the corresponding CPU based code on a single core. A three-dimensional-fifteen-velocity ($D3Q15$) lattice model is used. The effects of channel inclination, viscosity and density contrasts are investigated. The contours of the density and the average viscosity profiles in different planes are plotted and compared with those obtained in a two dimensional channel. This study provides the complete picture of the instabilities; a new screw-type instability is seen in the three-dimensional channel which can not be observed in two-dimensional channel. Previously, Riaz & Meiburg (2003) and Oliveira & Meiburg (2011) numerically studied three-dimensional displacement flow of two miscible fluids in porous media and Hele-Shaw cell, respectively. They found that some of the flow features in 3D are qualitatively different from those obtained in 2D simulation. Similarly, Hallez & Magnaudet (2008) investigated the effects of buoyancy in inclined channel/pipe, and found that the vortical structures are more coherent in two-dimensional geometry than those in three-dimensional geometry.

In this chapter, the details of the problem formulation are given in section 5.1 and the results of this study are provided in section 5.2.

5.1 Problem description

The pressure-driven displacement of one liquid (liquid ‘2’: viscosity μ_2 and density ρ_2) by an another liquid (liquid ‘1’: viscosity μ_1 and density ρ_1) in a square duct is considered. The liquids are immiscible and are assumed to be incompressible Newtonian. The schematic of the geometry is shown in Fig. 5.1. A three-dimensional rectangular coordinate system (x, y, z) , is used to model the flow dynamics where x , y and z denote the axial, vertical and the azimuthal coordinates, respectively. The inlet and the outlet of the channel are located at $x = 0$ and L , respectively. The rigid and impermeable walls of the channel are located at $y = 0, H$ and $z = 0, W$, where in this study, we chose $W = H$. The aspect ratio of channel, L/H is 32. θ is the angle of inclination measured with the horizontal. \mathbf{g} is the acceleration due to gravity. The components of gravity $\mathbf{g}_x(\equiv g\sin\theta)$ and $\mathbf{g}_y(\equiv g\cos\theta)$ act in the negative axial and negative vertical directions, respectively. The gravity component in the azimuthal direction, \mathbf{g}_z equals to zero. In the initial configuration, the channel portions from $0 \leq x \leq H/4$ and $H/4 \leq x \leq L$ are filled with liquid ‘1’ and liquid ‘2’, respectively.

At $t = 0$, the liquids inside the channel are stationary when a fully-developed flow due to a pressure-

gradient is imposed at the inlet. This is given by

$$\frac{\partial^2 u}{\partial y^2} + \frac{\partial^2 u}{\partial z^2} = Re \frac{dp}{dx}, \quad (5.1)$$

where u is the velocity component in the axial direction and p is the pressure. The velocity components in the vertical (v) and azimuthal (w) directions are zero at the inlet. The pressure-gradient is obtained from the constant volumetric flow rate condition (in the present study, the volumetric flow rate Q is 89.38). The no-slip and no penetration boundary conditions are imposed at the walls and the Neumann condition is prescribed at the outlet ($x = L$). The Reynolds number is defined as $Re \equiv Q\rho_1/W\mu_1$. Viscosity ratio, m , is the ratio of viscosity of liquid '2' to the viscosity of liquid '1', i.e. $m \equiv \mu_2/\mu_1$. The density contrasts between the liquids are measured by Atwood number $At (\equiv (\rho_2 - \rho_1)/(\rho_2 + \rho_1))$. The gravity effects can be characterized by Froude number (Fr), defined as $Fr \equiv Q/HW \sqrt{AtgH}$. The magnitude of surface tension is measured by κ , which we kept constant in the present study. The dimensionless time scale is represented as $t (\equiv H^2W/Q)$.

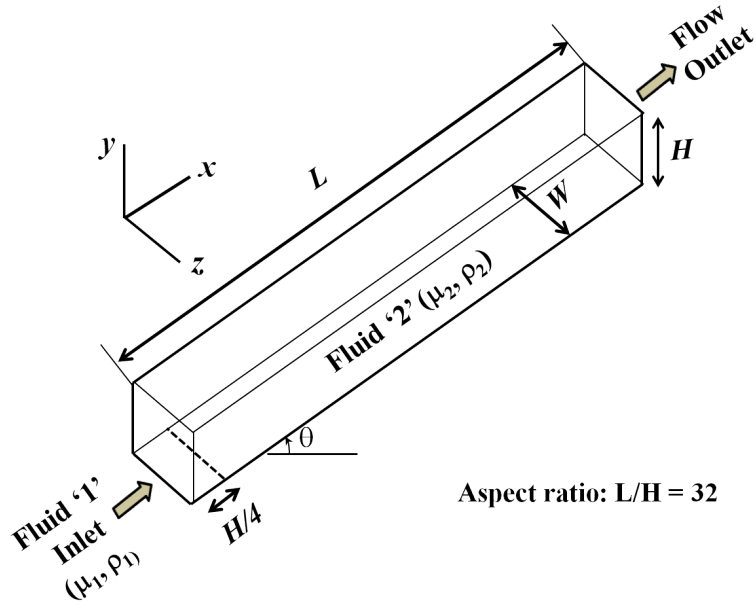


Figure 5.1: Schematic describing the geometry and the initial configuration. The inlet and outlet are located at $x = 0$ and $x = L$, respectively. The aspect ratio of the channel, L/H , is 32. Initially the channel portions from $0 \leq x \leq H/4$ and $H/4 \leq x \leq L$ are filled with liquid '1' and liquid '2', respectively.

5.2 Results and discussion

We start presenting our results by first showing the results of grid independency tests. The temporal variation of the dimensionless mass of liquid '2', M_t/M_0 , is plotted for different grids in Fig. 5.2. Here M_t represents the instantaneous mass of liquid '2', and is defined as $M_t = \rho_2 \int_0^W \int_0^H \int_0^L \frac{\phi - \phi_1}{\phi_2 - \phi_1} dx dy dz$. $M_0 (\equiv \rho_2 \frac{\phi - \phi_1}{\phi_2 - \phi_1} LHW)$ is the mass of liquid '2' initially occupying the channel at $t = 0$. The parameters used to generate this plot are $Re = 100$, $m = 10$, $At = 0.2$, $Fr = 5$, $\kappa = 0.005$ and $\theta = 45^\circ$. In Fig. 5.2, it can be seen that M_t/M_0 decrease monotonically with time as liquid '2' is displaced by

liquid ‘1’. The dotted line represents the analytical expression for plug-flow displacement (given by $M_t/M_0 = 1 - tH/L$). It can be seen that during the early times ($t < 10$) the displacement rate is close to that of the analytical solution. However at latter times, the actual displacement is slower than that of the plug-flow displacement process. Similar behavior is observed in the two-dimensional simulation shown in Chapter 4, but for miscible fluids, Sahu *et al.* (2009b) found that the displacement rate is much faster than that of the plug flow displacement. This difference is attributed to the phase change associated with the miscible systems. In Fig. 5.2 it can be seen that the results obtained using different grids are nearly the same (with a maximum absolute error less than 1%). The contours of ϕ in the x - y plane obtained from the three-dimensional simulation for the parameter values same as Fig. 5.2 are shown in Fig. 5.3 for $t = 10$ and 30 for different grids considered. It can be seen that the flow dynamics are qualitatively similar for all the grids considered; however close inspection of these results reveals that there is a slight increase in the velocity of the finger tip for the coarsest grid, which tends to converge as we increase the grid points. Therefore for rest of the simulations, $2112 \times 66 \times 66$ grid is used.

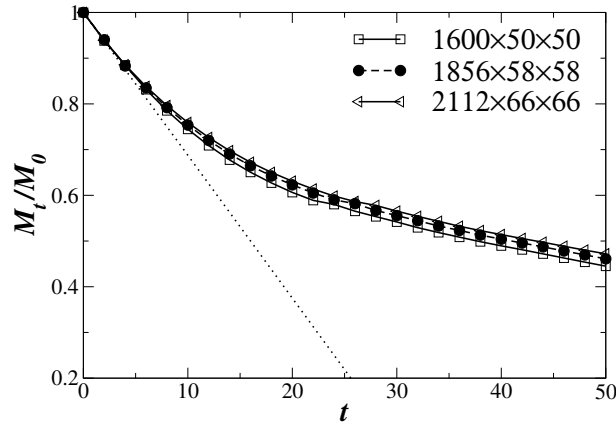


Figure 5.2: Variation of mass fraction of the displaced liquid (M_t/M_0) with time for different grids. The rest of the parameters are $Re = 100$, $m = 10$, $At = 0.2$, $Fr = 5$, $\kappa = 0.005$ and $\theta = 45^\circ$. The dotted line represents the analytical solution of the plug-flow displacement, given by $M_t/M_0 = 1 - tH/L$.

The spatio-temporal evolution of the isosurface of ϕ in the range 0.023 – 0.25 (which represents the interface between the fluids) is shown in Fig. 5.4 for the parameter values the same as those used to generate Fig. 5.2. This set of parameter values represents a situation when a less viscous and less dense liquid displaces a highly viscous and highly dense liquid. In this system, due to the imposed pressure-gradient at the inlet, a ‘finger’ of liquid ‘1’ penetrates into the region of liquid ‘2’. As the channel is inclined at an angle $\theta = 45^\circ$, the motion induced by the imposed pressure-gradient is opposed by the flow due to the gravitational force (proportional to g_x) in the negative axial direction. Therefore the flow dynamics is due to the competition between the imposed pressure-gradient and the gravity force. At the same time, the component of the gravitational force in the vertical direction (proportional to g_y) acts to segregate the two liquids. The finger becomes asymmetrical because of this force. We observed that for $t \geq 10$ the interface separating the two liquids becomes unstable forming nonlinear interfacial waves which grow in time. At later times ($t > 18$ for this set of parameter values) the instabilities of corkscrew pattern are observed. This pattern is the consequence of the Yih-type instabilities [Yih (1967)] in the linear regime. By conducting a linear stability analysis in a miscible core-annular flow configuration, Selvam *et al.* (2007) found that, at low diffusivity, the corkscrew mode becomes more unstable than the axisymmetric mode. The corkscrew-type pattern was also observed by Scoffoni *et al.* (2001) in miscible displacement flow in a vertical pipe.

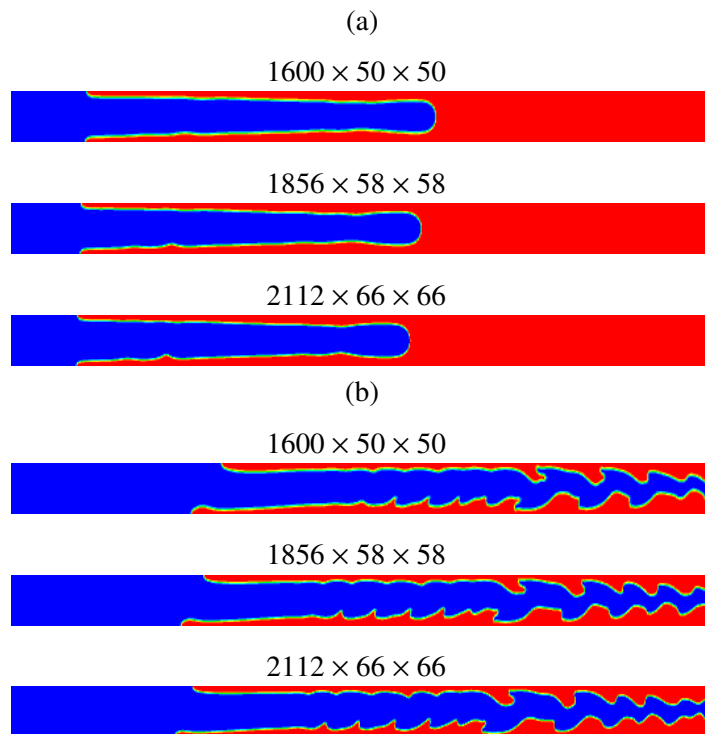


Figure 5.3: Contours of the index function, ϕ at (a) $t = 10$ and (b) $t = 30$ in the x - y plane at $z = W/2$ for different grids. The parameters are the same as those of Fig. 5.2 .

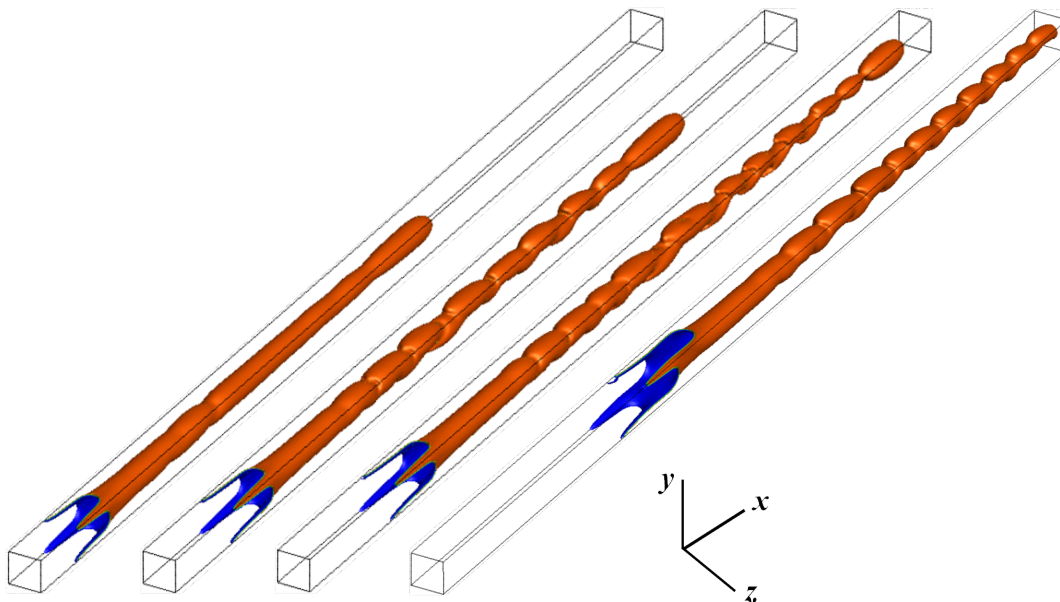


Figure 5.4: Evolution of the isosurface of ϕ at the interface at different times (from left to right: $t = 12, 18, 30$ and 50) for the simulation domain of $2112 \times 66 \times 66$ grid. The parameters are $Re = 100$, $m = 10$, $At = 0.2$, $Fr = 5$, $\kappa = 0.005$ and $\theta = 45^\circ$. The flow is in the positive x -direction.

Next, the effects of angles of inclination, θ is discussed by plotting the contours of ϕ at $t = 20$ in the x - y plane at $z = W/2$, and in x - z plane at $y = H/2$ in Fig. 5.5(a) and (b), respectively. The rest of the parameter values are $Re = 100$, $At = 0.2$, $m = 10$, $Fr = 1$ and $\kappa = 0.005$. The plots in panel (a) of this figure are the views in the z -direction. It can be seen that the intensity of the instabilities increases with increasing the angle of inclination. Also due to the decrease in the gravitational force in the y -direction, for higher angles of inclination core-annular structures form as the finger penetrates downstream. However, the gravitational force in the negative axial direction increases with increasing θ , which makes the trailing fingers asymmetrical in the upstream regime. We observe that the fingers have blunt “nose” separating the two fluids in these cases. For largest angle of inclination considered ($\theta = 85^\circ$), the droplet of fluid ‘1’ is detached from the main finger at $t = 20$. As the gravitational force in the y -direction decreases with increase in θ , for higher angles of inclination it is dominated by the effects created due to the imposed pressure-gradient; thus leaving patches of the heavier fluid near the top wall at $y = H$. This is shown in Fig. 5.5(b) when one looks from the top in the y -direction.

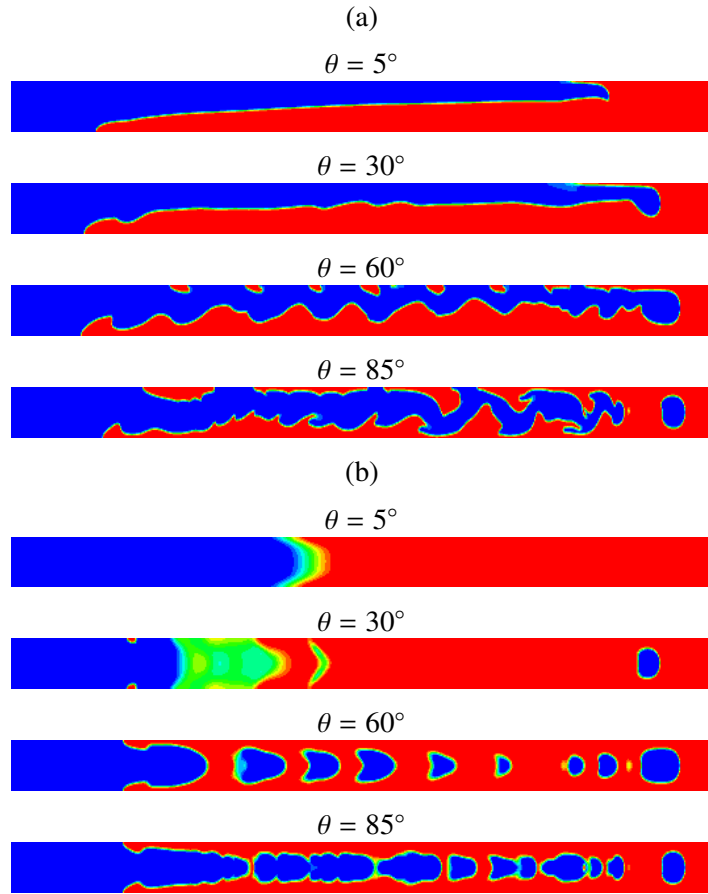


Figure 5.5: Contours of the index function, ϕ at $t = 20$ in (a) x - y plane at $z = W/2$, and (b) x - z plane at $y = H/2$. The parameters are $Re = 100$, $At = 0.2$, $m = 10$, $Fr = 1$ and $\kappa = 0.005$.

The contours of ϕ in the y - z plane at $x = L/2$ are shown in Fig. 5.6 for different angles of inclination. The parameter values are the same as those used to generate Fig. 5.5. This is a view of a cross-section at the mid-length of the channel in the x -direction. For smaller angles of inclination, the gravitational force in the negative y -direction is stronger which tries to settle the heavier fluid in the bottom part of the channel. This can be observed for $\theta \leq 30^\circ$ in Fig.5.6. However as discussed above for higher angles of inclination the pressure-gradient dominates the flow dynamics creating a core-annular configuration as

shown in Fig. 5.6 for $\theta > 60^\circ$.

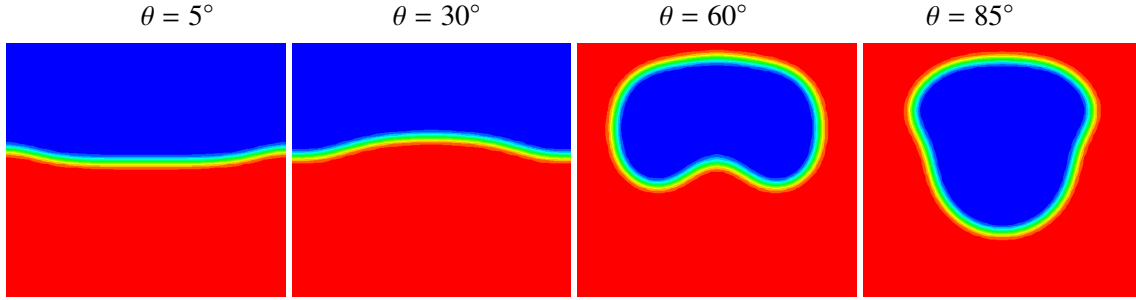


Figure 5.6: Contours of the index function, ϕ at $t = 20$ in the y - z plane at $x = L/2$. The parameters are $Re = 100$, $At = 0.2$, $m = 10$, $Fr = 1$ and $\kappa = 0.005$.

In Fig. 5.7(a) and (b), the axial variation of normalized average viscosity, $\bar{\mu}_{yz} (\equiv \mu_{yz}/\mu_{yz}^0)$ is plotted at different times for $\theta = 30^\circ$ and $\theta = 85^\circ$, respectively. Here $\mu_{yz} = \frac{1}{HW} \int_0^W \int_0^H \mu dy dz$ and μ_{yz}^0 is the value of μ_{yz} at $x = 0$. The rest of the parameters are the same as those in Fig. 5.5. It can be seen that as expected from the discussion of Fig. 5.5(a) the variation becomes increasingly complex with increase in θ . Similarly, the vertical variation of normalized average viscosity, $\bar{\mu}_{xz} (\equiv \mu_{xz}/\mu_{xz}^0)$, where $\mu_{xz} = \frac{1}{LW} \int_0^W \int_0^L \mu dx dz$, is plotted in Fig. 5.8 for different times. The value of μ_{xz} at $y = 0$ is designated by μ_{xz}^0 . It can be seen that for higher angles of inclination a core-annular structure is formed, which was also discussed in Fig. 5.6. On the other hand, for lower angles of inclination a two-layer structure is formed as the heavier fluid settles in the lower part of the channel.

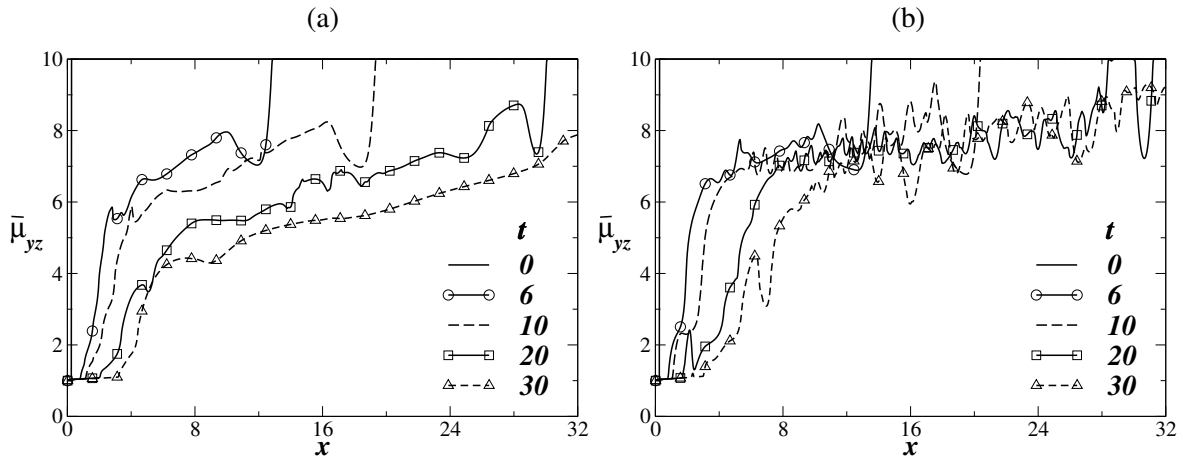


Figure 5.7: Axial variation of normalized average viscosity, $\bar{\mu}_{yz} (\equiv \mu_{yz}/\mu_{yz}^0)$ for (a) $\theta = 30^\circ$ and (b) $\theta = 85^\circ$. The rest of the parameters are $Re = 100$, $At = 0.2$, $m = 10$, $Fr = 1$ and $\kappa = 0.005$. Here $\mu_{yz} = \frac{1}{HW} \int_0^W \int_0^H \mu dy dz$, and μ_{yz}^0 is the value of μ_{yz} at $x = 0$.

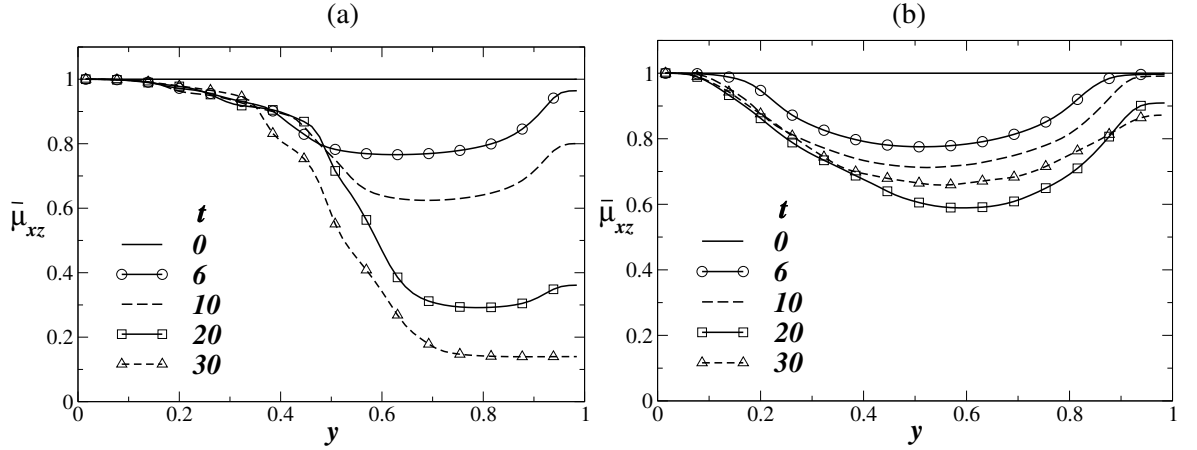


Figure 5.8: Vertical variation of normalized average viscosity, $\bar{\mu}_{xz} (\equiv \mu_{xz}/\mu_{xz}^0)$ for (a) $\theta = 30^\circ$, and (b) $\theta = 85^\circ$. The rest of the parameters are the same as those used in Fig. 5.5. Here $\mu_{xz} = \frac{1}{LW} \int_0^W \int_0^L \mu dx dz$, and μ_{xz}^0 is the value of μ_{xz} at $y = 0$.

The three-dimensional results are next compared with those obtained from the two-dimensional simulations. For this, the axial and the vertical variation of $\bar{\mu}_y (\equiv \mu_y/\mu_y^0)$ and $\bar{\mu}_x (\equiv \mu_x/\mu_x^0)$ are plotted in Figs. 5.9 and 5.10, respectively, for $\theta = 5^\circ$ and $\theta = 85^\circ$. Here $\mu_y = \frac{1}{H} \int_0^H \mu dy$ and $\mu_x = \frac{1}{L} \int_0^L \mu dx$. μ_y^0 and μ_x^0 are the values of μ_y at $x = 0$ and μ_x at $y = 0$, respectively. It can be seen in Fig. 5.9 that the axial variation of $\bar{\mu}_y$ is more chaotic in the two-dimensional channel as compared to that in three-dimensional channel (shown in Fig. 5.7). This is due to the stabilizing effects of the azimuthal walls to the disturbances of smaller-wavelength. This behavior is similar to the surface-tension effects in two-dimensional channel [Hooper & Grimshaw (1985)]. Inspection of the vertical variation of $\bar{\mu}_x$ reveals that the two-dimensional flow remains core-annular even for small angles of inclination. This is in contrast with the phenomena observed in three-dimensional computations (Fig. 5.8).

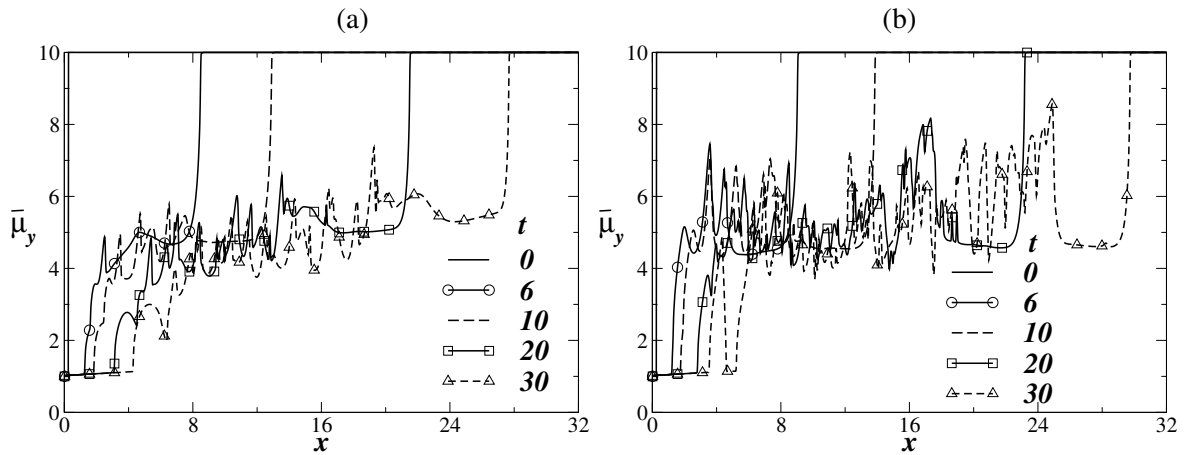


Figure 5.9: Axial variation of normalized average viscosity, $\bar{\mu}_y (\equiv \mu_y/\mu_y^0)$, for (a) $\theta = 5^\circ$, (b) $\theta = 85^\circ$ in a two-dimensional channel. The rest of the parameters are the same as those used to generate Fig. 5.5. Here $\mu_y = \frac{1}{H} \int_0^H \mu dy$, and μ_y^0 is the value of μ_y at $x = 0$.

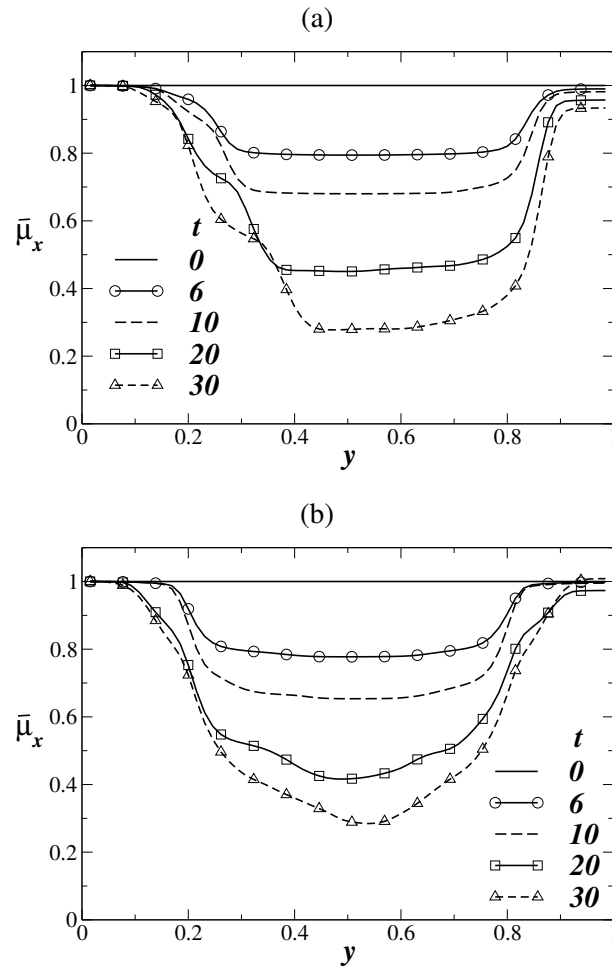


Figure 5.10: Vertical variation of normalized average viscosity, $\bar{\mu}_x (\equiv \mu_x / \mu_x^0)$, for (a) $\theta = 5^\circ$, (b) $\theta = 85^\circ$ in a two-dimensional channel. The rest of the parameters are the same as those used to generate Fig. 5.5. Here $\mu_x = \frac{1}{L} \int_0^L \mu dx$, and μ_x^0 is the value of μ_x at $y = 0$.

Lastly, the results obtained from the two and three-dimensional channel are compared by plotting the spatio-temporal evolution of ϕ contours in Fig. 5.11(a) and (b), respectively for $Re = 100$, $m = 20$, $At = 0.2$, $Fr = 5$, $\theta = 30^\circ$ and $\kappa = 0.005$. It can be observed that 3D effect reduces the short-wave instabilities, which are apparent in the two-dimensional channel. This behavior is also discussed above. Close inspection of Fig. 5.11 also reveals that the velocity of the finger tip is more in three-dimensional channel than that in the two-dimensional channel. We found (not shown here) that the effects of other parameters such as Atwood number, Froude number and surface-tension parameter are similar to that of two-dimensional channel.

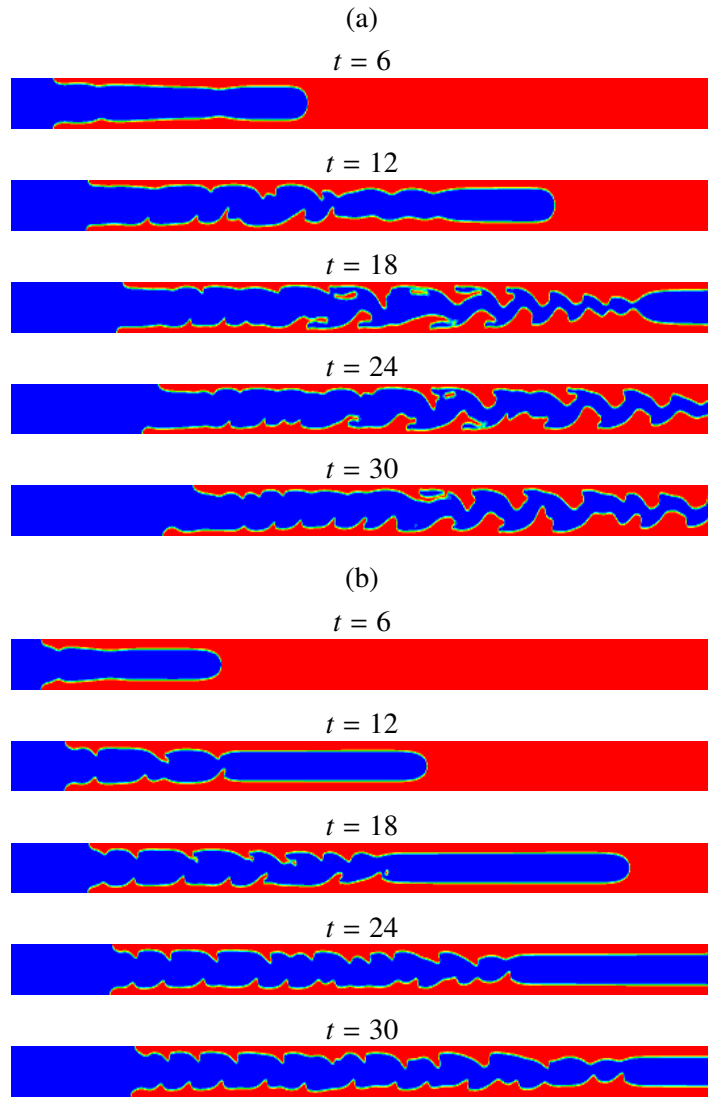


Figure 5.11: Spatio-temporal evolution of the contours of the index function, ϕ . (a) x - y plane at $z = W/2$ (three-dimensional simulation), and (b) the corresponding two-dimensional results. The parameters are $Re = 100$, $m = 20$, $At = 0.2$, $Fr = 5$, $\theta = 30^\circ$ and $\kappa = 0.005$.

5.3 Summary

Three-dimensional simulations of pressure-driven displacement flow of two immiscible liquids are performed in a square duct using a multiphase lattice Boltzmann approach, and compared with the corresponding two-dimensional simulations. The flow dynamics in a three-dimensional channel is quite different than that in two-dimensional channel. In particular, screw-type instabilities are found in three-dimensional channel, whereas saw-tooth type instabilities are apparent in 2D channel. It is also shown that increasing angle of inclination increases the intensity of the instabilities. The effects of Atwood number, Froude number and surface-tension parameter are observed to be qualitatively similar to those in a two-dimensional channel.

CHAPTER 6

Other studies

Apart from the studies reported in previous chapters, few other preliminary studies are carried out. In this chapter, the buoyancy-driven interpenetration of two immiscible fluids in an oscillating confined channel is presented. Here, the effect of time period of oscillation on the mixing characteristics is investigated using the multiphase lattice Boltzmann approach reported in Chapter 2. The geometry considered and results obtained from this study are discussed below.

6.1 Interpenetration of two immiscible fluids in an oscillating channel

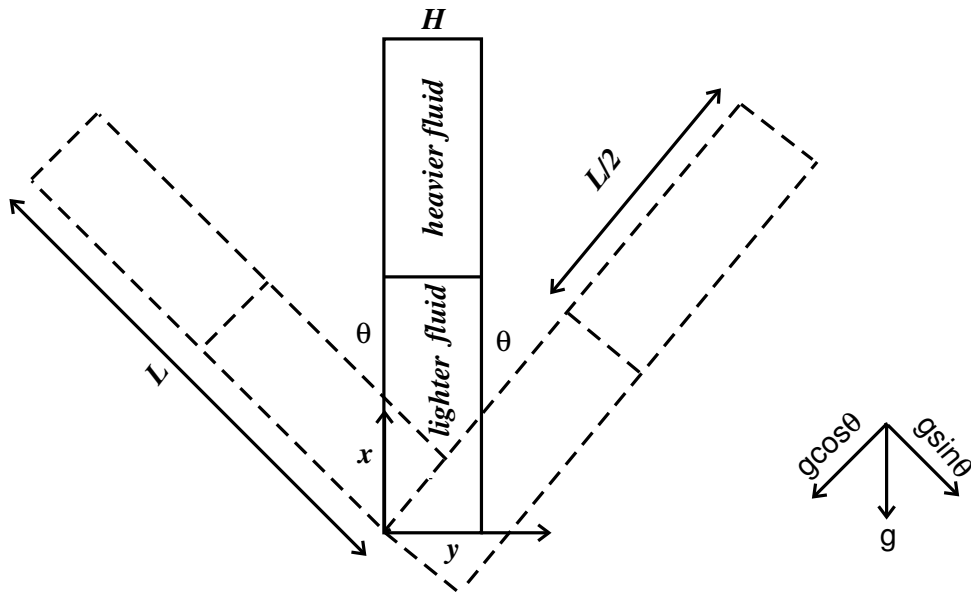


Figure 6.1: Schematic showing the geometry (not to scale) of the system.

The buoyancy-driven flow of two immiscible fluids in an oscillating channel of height L and width H is considered, as shown in Fig. 6.1. The upper and the lower halves of the channel are filled with a fluid having density ρ_1 and viscosity μ_1 and a fluid having density ρ_2 and viscosity μ_2 , respectively; $\rho_1 > \rho_2$. These fluids are initially separated by a partition at $x = L/2$ which is suddenly removed and both the fluids are allowed to interpenetrate into each other at $t > 0$. A two-dimensional rectangular coordinate system (x, y) is used to describe the flow, where x and y denote the axial and the transverse coordinates, respectively. \mathbf{g} is the acceleration due to gravity, such that the components of the gravity, $\mathbf{g}_x (= g \cos \theta)$ and $\mathbf{g}_y (= g \sin \theta)$ act in the axial and the negative transverse direction, respectively. Here, θ is the angle of inclination measured with the vertical, given by $\theta = \theta_m + \cos(2\pi t/T_p)$ where θ_m is the

maximum angle of inclination, t is the time and T_p is the time period of oscillation. As the flow is a balance between inertial and gravity forces, the characteristic velocity is defined as $V = \sqrt{gH}$. Various dimensionless parameters describing the flow are the viscosity ratio ($m = \mu_1/\mu_2$), Atwood number ($At \equiv (\rho_2 - \rho_1)/(\rho_2 + \rho_1)$), Reynolds number ($Re \equiv H^{3/2}g^{1/2}\rho_1/\mu_1$), magnitude of surface tension (κ) and the time period of oscillation (T_p). The gravity is chosen such that $\sqrt{gH} = 0.08$. In the present study, $\kappa = 0$.

6.1.1 Results and discussion

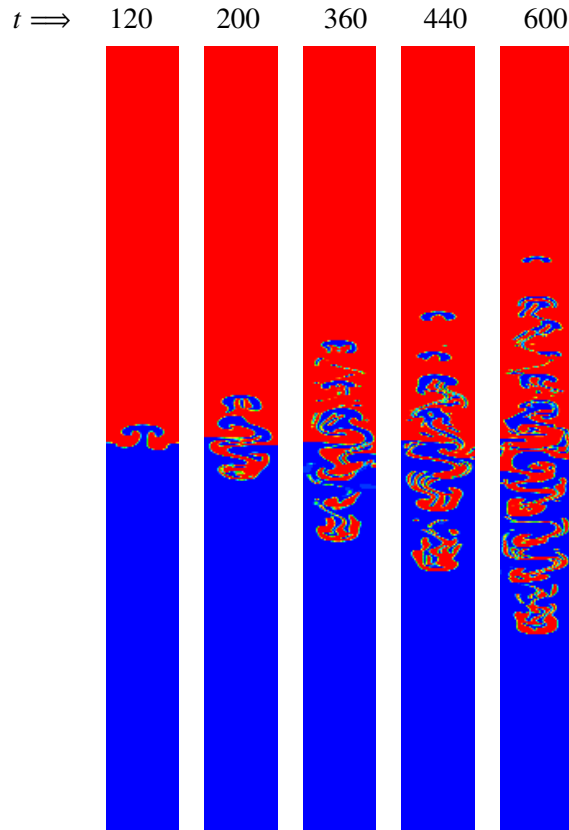


Figure 6.2: Spatio-temporal evolution of density contours in a non-oscillating vertical channel. The simulation parameters are $At = 0.01$, $m = 1$, $Re = 500$, $\theta_m = 0^\circ$ and $\kappa = 0$.

The main objective of the present study is to investigate the effects of time period of oscillation and the Atwood number on the buoyancy induced mixing of two immiscible liquids of equal viscosities but different densities. I begin the presentation of the results by first considering a non-oscillating vertical channel to study the mixing dynamics. Fig. 6.2 shows the spatio-temporal evolution of the density contours in a vertical channel ($\theta_m = 0^\circ$, $T_p = 0$) for $At = 0.01$. The rest of the parameters are $m = 1$, $Re = 500$ and $\kappa = 0$. It can be seen that for $t > 0$, the two fluids interpenetrate each other by moving into the upper and the lower regions of the channel. Here the mixing and the flow are characterized by the competition between inertial and the gravity forces. The gravitational force, g , has two components. The axial component of gravity, proportional to $g\cos\theta$, acts in the negative x -direction. It induces motion of the heavier fluid in the downward direction by displacing the lighter fluid into the upper part of the channel. The lighter fluid, by mass conservation, moves into the region of the displaced heavier fluid. Thus the two fluids accelerate into each other as the time progresses. On the other hand, the fluids

segregate because of the other component of gravity, $g\sin\theta$; however, for $\theta_m = 0^\circ$, there is no effect of this component of gravity on the flow dynamics. Thus in this case, the only effect is due to the axial component of gravity which favors the mixing process due to the formation of the interfacial instabilities as the fingers of the heavier and the lighter fluids penetrate in the downward and the upward directions, respectively. At later times, these instabilities become vigorous resulting in intense ‘mixing’ of the fluids.

Next, consider a channel initially inclined at an angle θ_m and the channel is subjected to oscillations around this angle of inclination. The dynamics obtained in an oscillatory channel, oscillating with a time period of oscillation, $T_p = 9600$ is shown in Fig. 6.3 which shows the spatio-temporal evolution of density contours at various times. Rest of the parameter values are $At = 0.01$, $m = 1$, $Re = 500$, $\theta_m = 45^\circ$ and $\kappa = 0$. In comparison with the density contours obtained in a non-oscillating channel (Fig. 6.2), it can be seen here that the mixing is more vigorous and the interpenetration is more as compared with that in the vertical channel.

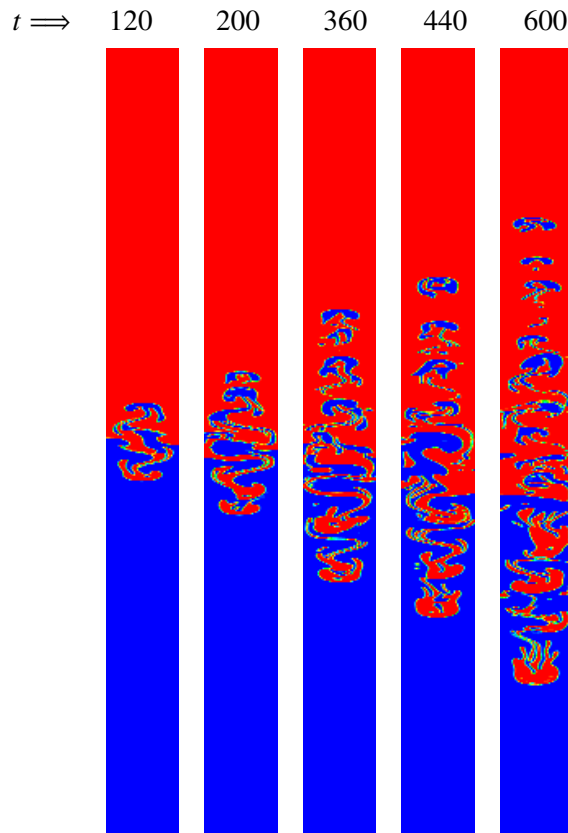


Figure 6.3: Spatio-temporal evolution of density contours in an oscillating channel with $T_p = 9600$. The simulation parameters are $At = 0.01$, $m = 1$, $Re = 500$, $\theta_m = 45^\circ$ and $\kappa = 0$.

The axial variation of depth-averaged c ($\bar{c}_x = \int_0^H c dy/H$) and the transverse variation of axially-averaged c ($\bar{c}_y = \int_0^L c dx/L$) are shown in Fig. 6.4. The parameters that are used to generate this figure are the same as those of Fig. 6.3. Here, c corresponds to the term $(\rho - \rho_2)/(\rho_1 - \rho_2)$. It can be seen that the variation of depth-averaged c (\bar{c}_x) along the axial direction is asymmetrical. This is due to the transverse component of gravity that causes the segregation effect. When the transverse component of gravity is negligible, a symmetrical profile of \bar{c}_x is observed in the case of a vertical channel (not shown). For the set of parameters considered here, it can be observed that the transverse variation of axially-averaged c (\bar{c}_y) is complex. This is due to the unstable interface between the two fluids which can also

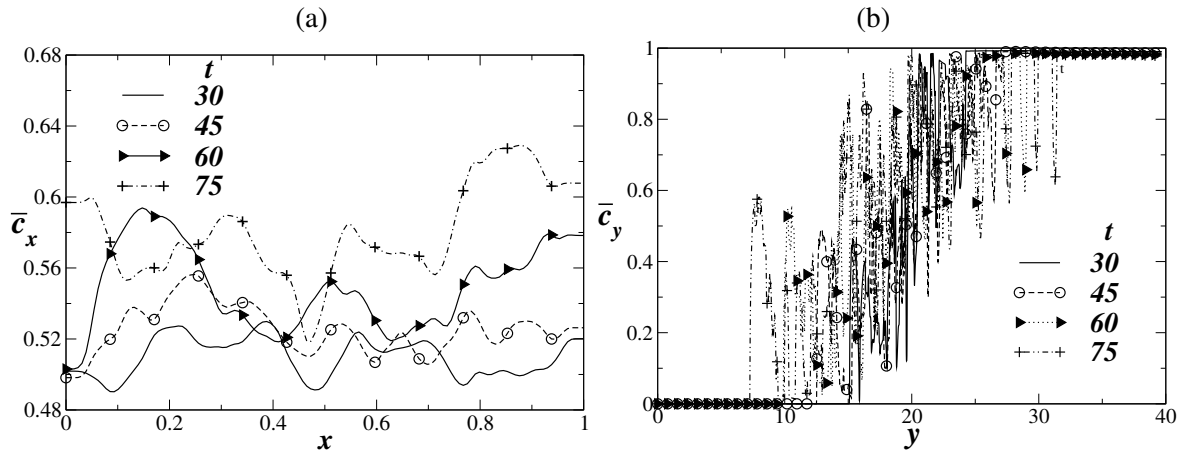


Figure 6.4: Evolution of the (a) axial variation of the depth-averaged c (\bar{c}_x) and (b) the transverse variation of the axially-averaged c (\bar{c}_y) in an oscillating channel with $T_p = 9600$. The rest of the parameter values are $At = 0.01$, $m = 1$, $Re = 500$, $\theta_m = 45^\circ$ and $\kappa = 0$.

be observed from the density contours shown in Fig. 6.4.

The effect of time period of oscillation (T_p) on the mixing characteristics is studied next. For this, a mixing length is defined as the total length of interpenetration of the both the fingers at each time. The mixing length obtained in an oscillating channel (L_m) is normalized with the mixing length obtained in a non-oscillatory channel (L_0). Fig. 6.5 shows the effect of T_p on the variation of the normalized mixing length, L_m/L_0 at various times. It is observed that as the time period of oscillation increases, the normalized mixing length also increases. Also, it can be seen that the oscillation enhances the mixing characteristics at early times. Therefore, intense mixing can be achieved early in a channel subjected to oscillation.

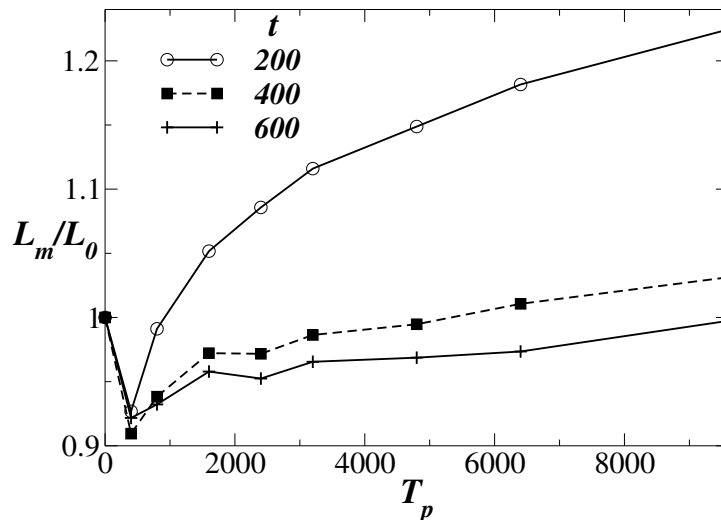


Figure 6.5: The effect of T_p on the normalized mixing length (L_m/L_0). The parameters are $At = 0.01$, $m = 1$, $Re = 500$, $\theta_m = 45^\circ$ and $\kappa = 0$.

Lastly, the effect of Atwood number on the mixing characteristics is investigated. Fig. 6.6 shows the variation of mixing length in an oscillating channel for four different combinations of Atwood number

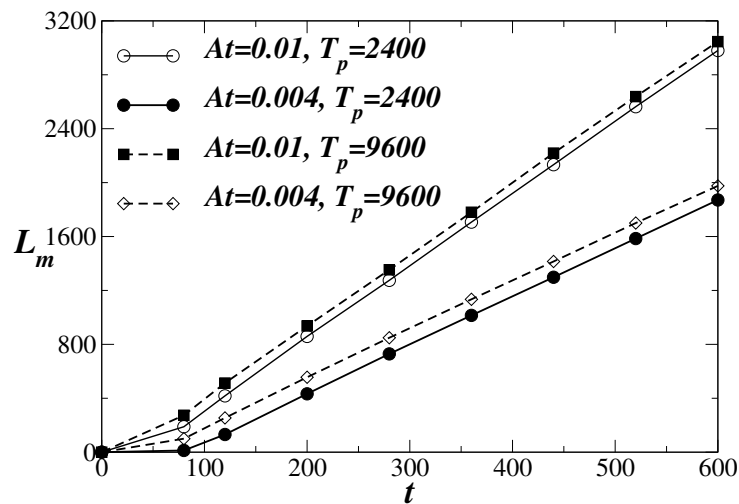


Figure 6.6: The temporal variation of mixing length in an oscillating channel (L_m) for various At and T_p . The parameters are $m = 1$, $Re = 500$, $\theta_m = 45^\circ$ and $\kappa = 0$.

and time period of oscillation. The other simulation parameters are $m = 1$, $Re = 500$, $\theta_m = 45^\circ$ and $\kappa = 0$. It can be seen that the mixing length increases with increasing At and also increasing T_p . It can be concluded from the figure that higher mixing lengths can be achieved with increase in Atwood number and time period of oscillation. Such a combination would give maximum interpenetration of the two fluids.

CHAPTER 7

Conclusions

In this thesis, the flow dynamics and instabilities occurring in buoyancy-driven and pressure-driven displacement flows of two immiscible liquids with varying viscosity and density in two- and three-dimensional channels are investigated using a multiphase LBM approach. The resulting flow in such systems can give rise to several new instability patterns. As the problems considered in this thesis are computationally very expensive, a lattice Boltzmann method is used for solving these problems.

The LBM is an alternative computational method for fluid flows and is found to be very promising for interfacial flows. It is a mesoscopic model derived from lattice gas automata. The explicit nature of this method and the absence of the pressure-Poisson equation (which is essential to satisfy the conservation of mass in conventional Navier-Stokes (N-S) solvers) make the method computationally very economical and an easily parallelizable technique. In addition to this, our LBM code is implemented on graphics processing unit (GPU), which gives 25 times speed up over the corresponding CPU based code. The GPU is a new paradigm for scientific computing. It is a powerful tool for performing parallel computations with less energy consumption (one GPU card requires only 150 Watts and it costs only Rs. 60,000-70,000). The LBM, which itself is computationally faster than the conventional N-S solvers, when implemented on GPU, gives a very high computational speed-up.

The various problems investigated in the present work are discussed below.

(i) Buoyancy-driven flow which is commonly known as lock-exchange flow refers to the interpenetration of two immiscible fluids initially separated by a partition and suddenly allowed to mix under the action of the gravitational force. Considering miscible fluids having different density, but the same dynamic viscosity, this problem has been studied experimentally and numerically by many researchers [Séon *et al.* (2004), Séon *et al.* (2007*a,b*), Hallez & Magnaudet (2008)]. In the present work, the buoyancy-induced interpenetration of two immiscible fluids of varying viscosities and densities is investigated in a confined tilted channel. In this configuration, the gravitational force has two components, which act in the axial and transverse directions. The axial component of gravity induces a downward motion of the heavier fluid, which in turn, by mass conservation, displaces the lighter fluid to move into the region of the heavier fluid. Thus both the heavier and the lighter fluids accelerate into the lower and the upper parts of the channel, respectively. On the other hand, the component of the gravitational force in the transverse direction, acts to segregate the two fluids. The interface between the fluids becomes unstable, which give rise to the development of the interfacial instabilities.

The main aim of this study is to investigate the effects of viscosity differential on the flow dynamics. For high viscosity ratios relatively stable fingers are observed, which move essentially like two individual Poiseuille flows in the opposite directions. The intensity of interfacial instabilities increases with decreasing viscosity differential of the fluids and the flow becomes progressively more complex. The front velocities decrease with increase in viscosity ratios. The effect of other parameters like the angle of inclination and surface tension are also investigated. A three-dimensional extension of this study is carried out and the results are compared with those obtained in two-dimensional channel.

(ii) Next, the effects on imposed pressure-gradient on the flow dynamics has been investigated. In this case, the displacement of an initially resident fluid inside the channel by another fluid of different viscosity and density, which is injected at the inlet, has been studied. As discussed above, the displacement flow of one fluid by another one can be found in many industrial and geological applications. In this case, the flow dynamics is a result of the competition between the imposed pressure-gradient and the axial component of gravity. The pressure-driven flow induces motion of displacing fluid into the channel, whereas the axial component of the gravity opposes this force by accelerating the displaced fluid in the upstream direction. When a less viscous fluid displaces a high viscous fluid, the flow becomes unstable forming interesting instability patterns at the interface separating the fluids.

This is a parametrically rich problem, involving several dimensionless parameters, such as, viscosity ratio, Atwood number, Reynolds number, Froude number, Capillary number and angle of inclination. A detailed parametric study is conducted to investigate the effects of these parameters on the flow dynamics. The Yih-type interfacial instabilities of sawtooth-like shape are observed at the interface separating the fluids. It is found that the displacement rate of the resident fluid decreases with increase in viscosity ratio. Although viscosity ratio has a non-monotonic effect on the velocity of the leading front, the velocity of the trailing front is found to be decreasing with increasing the viscosity ratio. Our results also predict the front velocity of the “lock-exchange flow” of two immiscible fluids in the exchange flow dominated regime which is consistent with the experiments of Séon *et al.* (2005). A single dimensionless parameter $\chi (\equiv 2Re \sin \theta / At Fr^2)$ is derived by balancing the buoyancy force in the axial direction with the imposed pressure force. Various flow regimes such as temporary back flow, stationary back flow and instantaneous displacement are identified based on χ . The critical value of χ for which transition of the exchanged flow regime to the displacement flow regime occurs agrees with the experimental finding of Taghavi *et al.* (2012). A linear stability analysis for a three-layer flow has been conducted and qualitative agreement is found with the results obtained from the lattice Boltzmann simulations.

(iii) Finally, in order to get the complete picture of the instabilities, the above study is extended to three-dimensions. A new screw-type instability is observed in the three-dimensional simulations. It is also shown that increasing angle of inclination increases the intensity of the instabilities. The effects of other parameters like Atwood number, Froude number and surface-tension parameter are observed to be qualitatively similar to those obtained in a two-dimensional channel.

In future, the study conducted in this thesis can be extended to include the temperature and non-Newtonian effects. Also it will be very interesting to study these problems in the very high Reynolds number regime, which are directly relevant to many industrial applications.

APPENDIX I

Derivation of Navier-Stokes equation from the Boltzmann equation

It is well known that hydrodynamic equations can be obtained from the continuous Boltzmann equation [Wagner (2008)].

A Maxwell-Boltzmann equilibrium distribution function and some important identities

Maxwell-Boltzmann equilibrium distribution function is given by

$$f^0(\mathbf{v}) = \frac{n}{(2\pi\theta)^{3/2}} e^{-[(\mathbf{v}-\mathbf{u})^2/2\theta]}. \quad (\text{I.1})$$

In this section, the proof of the following important identities are shown which are used in the subsequent derivations.

$$\int_{-\infty}^{\infty} f^0 = n, \quad (\text{I.2})$$

$$\int_{-\infty}^{\infty} f^0(v_\alpha - u_\alpha) = 0, \quad (\text{I.3})$$

$$\int_{-\infty}^{\infty} f^0(v_\alpha - u_\alpha)(v_\beta - u_\beta) = n\theta\delta_{\alpha\beta}, \quad (\text{I.4})$$

$$\int_{-\infty}^{\infty} f^0(v_\alpha - u_\alpha)(v_\beta - u_\beta)(v_\gamma - u_\gamma) = 0, \quad (\text{I.5})$$

$$\int_{-\infty}^{\infty} f^0(v_\alpha - u_\alpha)(v_\beta - u_\beta)(\mathbf{v} - \mathbf{u})^2 = 5n\theta^2\delta_{\alpha\beta}. \quad (\text{I.6})$$

A.1 Proof of Eq. (I.2)

Left hand side of Eq. (I.2) is given by

$$\begin{aligned}
 \int_{-\infty}^{\infty} f^0 dv &= \int_{-\infty}^{\infty} \frac{n}{(2\pi\theta)^{3/2}} e^{-(v-u)^2/2\theta} dv \\
 &= \frac{n}{(2\pi\theta)^{3/2}} \int_{-\infty}^{\infty} e^{-(v_1-u_1)^2/2\theta} dv_1 \int_{-\infty}^{\infty} e^{-(v_2-u_2)^2/2\theta} dv_2 \int_{-\infty}^{\infty} e^{-(v_3-u_3)^2/2\theta} dv_3 \\
 &= \frac{n}{(2\pi\theta)^{3/2}} I^3,
 \end{aligned} \tag{I.7}$$

where

$$I = \int_{-\infty}^{\infty} e^{-(v_1-u_1)^2/2\theta} dv_1.$$

Let $t = v_1 - u_1 \implies dt = dv_1$

So,

$$I = \int_{-\infty}^{\infty} e^{-t^2/2\theta} dt = \sqrt{2\pi\theta}.$$

So, Eq. (I.7) can be written as

$$\begin{aligned}
 \int_{-\infty}^{\infty} f^0 dv &= \frac{n}{(2\pi\theta)^{3/2}} I^3 \\
 &= \frac{n}{(2\pi\theta)^{3/2}} ((2\pi\theta)^{1/2})^3 \\
 &= n.
 \end{aligned}$$

A.2 Proof of Eq. (I.3)

Left hand side of Eq. (I.3) is given by

$$\begin{aligned}
 \int_{-\infty}^{\infty} f^0(v_\alpha - u_\alpha) dv &= \int_{-\infty}^{\infty} \frac{n}{(2\pi\theta)^{3/2}} e^{-(v-u)^2/2\theta} (v_\alpha - u_\alpha) dv \\
 &= \frac{n}{(2\pi\theta)^{3/2}} \int_{-\infty}^{\infty} e^{-(v_1-u_1)^2/2\theta} (v_\alpha - u_\alpha) dv_1 \int_{-\infty}^{\infty} e^{-(v_2-u_2)^2/2\theta} dv_2 \int_{-\infty}^{\infty} e^{-\frac{(v_3-u_3)^2}{2\theta}} dv_3 \\
 &= \frac{n}{(2\pi\theta)^{3/2}} I_1 \times I_2 \times I_3,
 \end{aligned}$$

where α can take values 1, 2, 3.

For $\alpha = 1$,

$$I_1 = \int_{-\infty}^{\infty} e^{-(v_1-u_1)^2/2\theta} (v_1 - u_1) dv_1.$$

Let $t = (v_1 - u_1)^2 \implies dt = 2(v_1 - u_1) dv_1$

So,

$$I_1 = \int_{-\infty}^{\infty} e^{-t/2\theta} dt = 0.$$

Similarly, for $\alpha = 2$, it can be shown that $I_2 = 0$ (keeping ' $v_2 - u_2$ ' in I_2 term).

and for $\alpha = 3$ it can be shown that $I_3 = 0$ (keeping ' $v_3 - u_3$ ' in I_3 term).
So, for any values of α we have, $I_1 \times I_2 \times I_3 = 0$.

So, LHS :

$$\int_{-\infty}^{\infty} f^0(v_\alpha - u_\alpha)dv = \frac{n}{(2\pi\theta)^{3/2}} \times 0 = 0.$$

A.3 Proof of Eq. (I.4)

Left hand side of Eq. (I.4) is given by

$$\begin{aligned} \int_{-\infty}^{\infty} f^0(v_\alpha - u_\alpha)(v_\beta - u_\beta)dv &= \int_{-\infty}^{\infty} \frac{n}{(2\pi\theta)^{3/2}} e^{-(v-u)^2/2\theta} (v_\alpha - u_\alpha)(v_\beta - u_\beta)dv \\ &= \frac{n}{(2\pi\theta)^{3/2}} \int_{-\infty}^{\infty} e^{-(v_1-u_1)^2/2\theta} (v_\alpha - u_\alpha)(v_\beta - u_\beta)dv_1 \int_{-\infty}^{\infty} e^{-(v_2-u_2)^2/2\theta} dv_2 \int_{-\infty}^{\infty} e^{-(v_3-u_3)^2/2\theta} dv_3 \\ &= \frac{n}{(2\pi\theta)^{3/2}} I_1 \times I_2 \times I_3, \end{aligned} \tag{I.8}$$

where α and β both can take values 1, 2, 3.

For $\alpha = 1$ and $\beta = 1$,

$$I_1 = \int_{-\infty}^{\infty} e^{-(v_1-u_1)^2/2\theta} (v_1 - u_1)^2 dv_1.$$

Let $t = v_1 - u_1 \implies dt = dv_1$

So,

$$\begin{aligned} I_1 &= \int_{-\infty}^{\infty} t^2 e^{-t^2/2\theta} dt = \frac{\sqrt{\pi}}{2} (2\theta)^{3/2}, \\ &\left(\int_{-\infty}^{\infty} x^2 e^{-ax^2} dx = \frac{\sqrt{\pi}}{2} a^{-3/2} \right) \end{aligned}$$

$$I_2 = \sqrt{2\pi\theta},$$

$$I_3 = \sqrt{2\pi\theta}.$$

Similarly for $\alpha = 2$ and $\beta = 2$, (including $(v_2 - u_2)^2$ in I_2 term)

$$I_1 = \sqrt{2\pi\theta},$$

$$I_2 = \frac{\sqrt{\pi}}{2} (2\theta)^{\frac{3}{2}},$$

$$I_3 = \sqrt{2\pi\theta}.$$

and for $\alpha = 3$ and $\beta = 3$, (including $(v_3 - u_3)^2$ in I_3 term)

$$I_1 = \sqrt{2\pi\theta},$$

$$I_2 = \sqrt{2\pi\theta},$$

$$I_3 = \frac{\sqrt{\pi}}{2} (2\theta)^{\frac{3}{2}}.$$

So, for any $\alpha = \beta$, we can say that

$$\begin{aligned} I_1 \times I_2 \times I_3 &= \sqrt{2\pi\theta} \times \sqrt{2\pi\theta} \times \frac{\sqrt{\pi}}{2} (2\theta)^{3/2} \\ \Rightarrow I_1 \times I_2 \times I_3 &= \theta \times (2\pi\theta)^{3/2} \end{aligned} \quad (\text{I.9})$$

For $\alpha = 1$ and $\beta = 2$,

$$\begin{aligned} I_1 &= \int_{-\infty}^{\infty} e^{-\frac{(v_1-u_1)^2}{2\theta}} (v_2 - u_2)(v_1 - u_1) dv_1 \\ &= (v_2 - u_2) \int_{-\infty}^{\infty} e^{-\frac{(v_1-u_1)^2}{2\theta}} (v_1 - u_1) dv_1 \\ &= 0 \end{aligned} \quad (\text{I.10})$$

Similarly, it can be said that for any $\alpha \neq \beta$, at least one of the integral will be zero. So,

$$I_1 \times I_2 \times I_3 = 0$$

From Eq.(I.9) and Eq.(I.10) we can say that

$$I_1 \times I_2 \times I_3 = \theta \times (2\pi\theta)^{3/2} \delta_{\alpha\beta}.$$

where $\delta_{\alpha\beta}$ = Kronecker delta.

So, LHS of Eq.(I.4)

$$\begin{aligned} \int_{-\infty}^{\infty} f^0(v_\alpha - u_\alpha)(v_\beta - u_\beta) dv &= \frac{n}{(2\pi\theta)^{3/2}} \times \theta \times (2\pi\theta)^{3/2} \delta_{\alpha\beta} \\ &= n\theta \delta_{\alpha\beta}. \end{aligned}$$

A.4 Proof of Eq. (I.5)

Left hand side of Eq.(I.5) is given as

$$\begin{aligned} &\int_{-\infty}^{\infty} f^0(v_\alpha - u_\alpha)(v_\beta - u_\beta)(v_\gamma - u_\gamma) dv \\ &= \frac{n}{(2\pi\theta)^{3/2}} \int_{-\infty}^{\infty} e^{-(v-u)^2/2\theta} (v_\alpha - u_\alpha)(v_\beta - u_\beta)(v_\gamma - u_\gamma) dv \\ &= \frac{n}{(2\pi\theta)^{3/2}} \int_{-\infty}^{\infty} e^{-(v_1-u_1)^2/2\theta} (v_\alpha - u_\alpha)(v_\beta - u_\beta)(v_\gamma - u_\gamma) dv_1 \\ &\quad \int_{-\infty}^{\infty} e^{-(v_2-u_2)^2/2\theta} dv_2 \int_{-\infty}^{\infty} e^{-(v_3-u_3)^2/2\theta} dv_3 \\ &= \frac{n}{(2\pi\theta)^{3/2}} I_1 \times I_2 \times I_3, \end{aligned}$$

For $\alpha = 1, \beta = 1$ and $\gamma = 1$, we have

$$I_1 = \int_{-\infty}^{\infty} (v_1 - u_1)^3 e^{-(v_1 - u_1)^2 / 2\theta} dv_1.$$

Let $t = v_1 - u_1 \implies dt = dv_1$

So,

$$I_1 = \int_{-\infty}^{\infty} t^3 e^{-t^2 / 2\theta} dt = 0.$$

For any set of values of α , β , and γ we can group together the term in I_1 , I_2 and I_3 in such a way that at least one of them will be zero. So, for any set of values of α , β , and γ ,

$$I_1 \times I_2 \times I_3 = 0.$$

So, LHS of Eq.(I.5)

$$\int_{-\infty}^{\infty} f^0(v_\alpha - u_\alpha)(v_\beta - u_\beta)(v_\gamma - u_\gamma)dv = 0.$$

A.5 Proof of Eq. (I.6)

Left hand side of Eq.(I.6) is given as

$$\begin{aligned} & \int_{-\infty}^{\infty} f^0(v_\alpha - u_\alpha)(v_\beta - u_\beta)(v - u)^2 dv \\ = & \frac{n}{(2\pi\theta)^{3/2}} \int_{-\infty}^{\infty} e^{-(v-u)^2 / 2\theta} (v_\alpha - u_\alpha)(v_\beta - u_\beta)(v - u)^2 dv \\ = & \frac{n}{(2\pi\theta)^{3/2}} \int_{-\infty}^{\infty} e^{-(v_1 - u_1)^2 / 2\theta} e^{-(v_2 - u_2)^2 / 2\theta} e^{-(v_3 - u_3)^2 / 2\theta} (v_\alpha - u_\alpha)(v_\beta - u_\beta) \left[(v_1 - u_1)^2 + (v_2 - u_2)^2 + (v_3 - u_3)^2 \right] dv, \end{aligned} \quad (\text{I.11})$$

For $\alpha = 1$ and $\beta = 1$, the above integral becomes

$$\frac{n}{(2\pi\theta)^{3/2}} \int_{-\infty}^{\infty} e^{-(v_1 - u_1)^2 / 2\theta} e^{-(v_2 - u_2)^2 / 2\theta} e^{-(v_3 - u_3)^2 / 2\theta} (v_1 - u_1)^2 \left[(v_1 - u_1)^2 + (v_2 - u_2)^2 + (v_3 - u_3)^2 \right] dv$$

Let $v_1 - u_1 = x$, $v_2 - u_2 = y$, $v_3 - u_3 = z$

By making the above substitution, we can write the above integral as

$$\begin{aligned} & \frac{n}{(2\pi\theta)^{3/2}} \int_{-\infty}^{\infty} e^{-x^2 / 2\theta} e^{-y^2 / 2\theta} e^{-z^2 / 2\theta} x^2 (x^2 + y^2 + z^2) dx dy dz \\ = & \frac{n}{(2\pi\theta)^{3/2}} \left[\left(\int_{-\infty}^{\infty} x^4 e^{-x^2 / 2\theta} dx \int_{-\infty}^{\infty} e^{-y^2 / 2\theta} dy \int_{-\infty}^{\infty} e^{-z^2 / 2\theta} dz \right) \right. \\ & + \left(\int_{-\infty}^{\infty} x^2 e^{-\frac{x^2}{2\theta}} dx \int_{-\infty}^{\infty} y^2 e^{-y^2 / 2\theta} dy \int_{-\infty}^{\infty} e^{-z^2 / 2\theta} dz \right) \\ & \left. + \left(\int_{-\infty}^{\infty} x^2 e^{-x^2 / 2\theta} dx \int_{-\infty}^{\infty} e^{-y^2 / 2\theta} dy \int_{-\infty}^{\infty} z^2 e^{-z^2 / 2\theta} dz \right) \right] \end{aligned} \quad (\text{I.12})$$

$$\begin{aligned}
&= \frac{n}{(2\pi\theta)^{3/2}} \left[\left(\sqrt{3}/4(2\theta)^{5/2} \times \sqrt{2\theta\pi} \times \sqrt{2\theta\pi} \right) \right. \\
&\quad + \left(\frac{\sqrt{\pi}}{2}(2\theta)^{3/2} \times \frac{\sqrt{\pi}}{2}(2\theta)^{3/2} \times \sqrt{2\theta\pi} \right) \\
&\quad \left. + \left(\frac{\sqrt{\pi}}{2}(2\theta)^{3/2} \times \sqrt{2\theta\pi} \times \frac{\sqrt{\pi}}{2}(2\theta)^{3/2} \right) \right]
\end{aligned} \tag{I.13}$$

$$\begin{aligned}
&= \frac{n}{(2\pi\theta)^{3/2}} \left[\left(2\pi\theta \times \sqrt{\pi} \frac{3}{4}(2\theta)^{5/2} \right) + \left(2 \times (2\theta)^3 \times \sqrt{2\theta\pi} \right) \right] \\
&= \frac{n}{(2\pi\theta)^{3/2}} \times (2\theta)^{7/2} \times \left(\frac{3}{4}\pi^{3/2} + \frac{2}{4}\pi^{3/2} \right) = n(2\theta)^2 \times 5/4 = 5n\theta^2.
\end{aligned} \tag{I.14}$$

We can obtain the same result for $\alpha = 2; \beta = 2$ and $\alpha = 3; \beta = 3$, by grouping together the terms in appropriate integrals.

So, for any $\alpha = \beta$, LHS of Eq.(I.6) = $5n\theta^2$.

But for any $\alpha \neq \beta$, for example $\alpha = 1, \beta = 2$

LHS of Eq.(I.6)

$$= \frac{n}{(2\pi\theta)^{3/2}} \int_{-\infty}^{\infty} e^{-\frac{(v_1-u_1)^2}{2\theta}} e^{-\frac{(v_2-u_2)^2}{2\theta}} e^{-\frac{(v_3-u_3)^2}{2\theta}} \left[(v_1 - u_1)^2 + (v_2 - u_2)^2 + (v_3 - u_3)^2 \right] (v_1 - u_1)(v_2 - u_2)$$

Let $v_1 - u_1 = x, v_2 - u_2 = y, v_3 - u_3 = z$

So,

$$\begin{aligned}
&= \frac{n}{(2\pi\theta)^{3/2}} \left[\int_{-\infty}^{\infty} (x^2 + y^2 + z^2)xy \left(e^{-x^2/2\theta} \times e^{-y^2/2\theta} \times e^{-z^2/2\theta} \right) \right] \\
&= \frac{n}{(2\pi\theta)^{3/2}} \left[\left(\int_{-\infty}^{\infty} x^3 e^{-x^2/2\theta} dx \int_{-\infty}^{\infty} y e^{-y^2/2\theta} dy \int_{-\infty}^{\infty} e^{-z^2/2\theta} dz \right) \right. \\
&\quad + \left(\int_{-\infty}^{\infty} x e^{-x^2/2\theta} dx \int_{-\infty}^{\infty} y^3 e^{-y^2/2\theta} dy \int_{-\infty}^{\infty} e^{-z^2/2\theta} dz \right) \\
&\quad \left. + \left(\int_{-\infty}^{\infty} x e^{-x^2/2\theta} dx \int_{-\infty}^{\infty} y e^{-y^2/2\theta} dy \int_{-\infty}^{\infty} z e^{-z^2/2\theta} dz \right) \right] \\
&= \frac{n}{(2\pi\theta)^{3/2}} (0 + 0 + 0) = 0
\end{aligned} \tag{I.15}$$

So, for any $\alpha \neq \beta$, LHS of Eq.(I.6) = 0.

Thus, we can say that

$$\int_{-\infty}^{\infty} f^0(v_\alpha - u_\alpha)(v_\beta - u_\beta)(v - u)^2 = 5n\theta^2 \delta_{\alpha\beta}.$$

where $\delta_{\alpha\beta}$ is kroneckor delta.

B Moments of Maxwell-Boltzmann equilibrium distribution function

B.1 Zeroth moment of equilibrium distribution function

Zeroth moment of equilibrium distribution function is given by Eq. (I.2) which we have proved in the previous section.

B.2 First moment of equilibrium distribution function

First velocity moment of equilibrium distribution function is

$$\int_{-\infty}^{\infty} f^0 v_{\alpha} = nu_{\alpha}.$$

To prove this we start from Eq. (I.3) (which we have proved in the previous section) i.e.

$$\begin{aligned} \int_{-\infty}^{\infty} f^0 (v_{\alpha} - u_{\alpha}) &= 0 \\ \Rightarrow \int_{-\infty}^{\infty} f^0 v_{\alpha} - \int_{-\infty}^{\infty} f^0 u_{\alpha} &= 0 \\ \Rightarrow \int_{-\infty}^{\infty} f^0 v_{\alpha} &= u_{\alpha} \int_{-\infty}^{\infty} f^0 \\ \Rightarrow \int_{-\infty}^{\infty} f^0 v_{\alpha} &= nu_{\alpha} \end{aligned} \tag{I.16}$$

B.3 Second moment of equilibrium distribution function

Second velocity moment of equilibrium distribution function is

$$\int_{-\infty}^{\infty} f^0 v_{\alpha} v_{\beta} = nu_{\alpha} u_{\beta} + n\theta \delta_{\alpha\beta}.$$

To prove this we start from Eq. (I.4) (which we have proved in the previous section) i.e.

$$\int_{-\infty}^{\infty} f^0 (v_{\alpha} - u_{\alpha})(v_{\beta} - u_{\beta}) = n\theta \delta_{\alpha\beta}$$

$$\begin{aligned}
&\Rightarrow \int_{-\infty}^{\infty} f^0 v_\alpha v_\beta - \int_{-\infty}^{\infty} f^0 v_\alpha u_\beta - \int_{-\infty}^{\infty} f^0 u_\alpha v_\beta + \int_{-\infty}^{\infty} f^0 u_\alpha u_\beta = n\theta\delta_{\alpha\beta} \\
&\Rightarrow \int_{-\infty}^{\infty} f^0 v_\alpha v_\beta - u_\beta \int_{-\infty}^{\infty} f^0 v_\alpha - u_\alpha \int_{-\infty}^{\infty} f^0 v_\beta + u_\beta \int_{-\infty}^{\infty} f^0 = n\theta\delta_{\alpha\beta} \\
&\Rightarrow \int_{-\infty}^{\infty} f^0 v_\alpha v_\beta - nu_\alpha u_\beta - nu_\alpha u_\beta + nu_\alpha u_\beta = n\theta\delta_{\alpha\beta} \\
&\Rightarrow \int_{-\infty}^{\infty} f^0 v_\alpha v_\beta = nu_\alpha u_\beta + n\theta\delta_{\alpha\beta}
\end{aligned} \tag{I.17}$$

B.4 Third moment of equilibrium distribution function

Third velocity moment of equilibrium distribution function is

$$\int_{-\infty}^{\infty} f^0 v_\alpha v_\beta v_\gamma = n\theta(u_\alpha\delta_{\beta\gamma} + u_\beta\delta_{\alpha\gamma} + u_\gamma\delta_{\alpha\beta}) + nu_\alpha u_\beta u_\gamma.$$

To prove this we start from Eq. (I.5) (which we have proved in the previous section) i.e.

$$\begin{aligned}
&\int_{-\infty}^{\infty} f^0 (v_\alpha - u_\alpha)(v_\beta - u_\beta)(v_\gamma - u_\gamma) = 0 \\
&\Rightarrow \int_{-\infty}^{\infty} f^0 (v_\alpha v_\beta - v_\alpha u_\beta - u_\alpha v_\beta + u_\alpha u_\beta)(v_\gamma - u_\gamma) = 0 \\
&\Rightarrow \int_{-\infty}^{\infty} f^0 v_\alpha v_\beta v_\gamma - \int_{-\infty}^{\infty} f^0 v_\alpha u_\beta v_\gamma - \int_{-\infty}^{\infty} f^0 u_\alpha v_\beta v_\gamma + \int_{-\infty}^{\infty} f^0 u_\alpha u_\beta v_\gamma \\
&- \int_{-\infty}^{\infty} f^0 v_\alpha v_\beta u_\gamma + \int_{-\infty}^{\infty} f^0 v_\alpha u_\beta u_\gamma + \int_{-\infty}^{\infty} f^0 u_\alpha v_\beta u_\gamma - \int_{-\infty}^{\infty} f^0 u_\alpha u_\beta u_\gamma = 0 \\
&\Rightarrow \int_{-\infty}^{\infty} f^0 v_\alpha v_\beta v_\gamma - u_\beta \int_{-\infty}^{\infty} f^0 v_\alpha v_\gamma - u_\alpha \int_{-\infty}^{\infty} f^0 v_\beta v_\gamma + u_\alpha u_\beta \int_{-\infty}^{\infty} f^0 v_\gamma \\
&- u_\gamma \int_{-\infty}^{\infty} f^0 v_\alpha v_\beta + u_\beta u_\gamma \int_{-\infty}^{\infty} f^0 v_\alpha + u_\alpha u_\gamma \int_{-\infty}^{\infty} f^0 v_\beta - u_\alpha u_\beta u_\gamma \int_{-\infty}^{\infty} f^0 = 0 \\
&\Rightarrow \int_{-\infty}^{\infty} f^0 v_\alpha v_\beta v_\gamma - u_\beta (nu_\alpha u_\gamma + n\theta\delta_{\alpha\gamma}) - u_\alpha (nu_\beta u_\gamma + n\theta\delta_{\beta\gamma}) + u_\alpha u_\beta (nu_\gamma) \\
&- u_\gamma (nu_\alpha u_\beta + n\theta\delta_{\alpha\beta}) + u_\alpha u_\gamma (nu_\beta) + u_\beta u_\gamma (nu_\alpha) - nu_\alpha u_\beta u_\gamma = 0 \\
&\Rightarrow \int_{-\infty}^{\infty} f^0 v_\alpha v_\beta v_\gamma - nu_\beta\theta\delta_{\alpha\gamma} - nu_\alpha u_\beta u_\gamma - nu_\alpha\theta\delta_{\beta\gamma} - nu_\gamma\theta\delta_{\alpha\beta} = 0 \\
&\Rightarrow \int_{-\infty}^{\infty} f^0 v_\alpha v_\beta v_\gamma = nu_\alpha u_\beta u_\gamma + n\theta(u_\alpha\delta_{\beta\gamma} + u_\beta\delta_{\alpha\gamma} + u_\gamma\delta_{\alpha\beta})
\end{aligned} \tag{I.18}$$

C Conservation of mass

Boltzmann equation with BGK approximation for collision operator can be written as

$$\partial_t f + v_\alpha \partial_\alpha f + F \partial_v f = \frac{1}{\tau} (f^0 - f). \tag{I.19}$$

Integrating, we get

$$\begin{aligned}
& \int \partial_t f \, dv + \int v_\alpha \partial_\alpha f \, dv + \int F \partial_v f \, dv = \int \frac{1}{\tau} (f^0 - f) \, dv \\
\Rightarrow & \partial_t \int f \, dv + \partial_\alpha \int v_\alpha f \, dv + \partial_v \int F f \, dv = \int \frac{1}{\tau} (f^0 - f) \, dv \\
\Rightarrow & \partial_t n + \partial_\alpha (n u_\alpha) + F \partial_v n = \frac{1}{\tau} (n - n) \\
\Rightarrow & \partial_t n + \partial_\alpha (n u_\alpha) = 0
\end{aligned} \tag{I.20}$$

D Conservation of momentum

From Eq. (I.19), we can write

$$f = f^0 - \tau(\partial_t f + v_\alpha \partial_\alpha f + F \partial_v f). \tag{I.21}$$

Eq. (I.19) can be re-written as

$$\partial_t f + v_\beta \partial_\beta f + F_\beta \partial_{v_\beta} f = \frac{1}{\tau} (f^0 - f).$$

multiplying “ v_α ” on both sides of the above equation and integrating, we get

$$\begin{aligned}
& \int v_\alpha \partial_t f \, dv + \int v_\alpha v_\beta \partial_\beta f \, dv + \int F_\beta v_\alpha \partial_{v_\beta} f \, dv = \int \frac{1}{\tau} (f^0 v_\alpha - f v_\alpha) \, dv \\
\Rightarrow & \partial_t \int v_\alpha f \, dv + \partial_\beta \int v_\alpha v_\beta f \, dv + F_\beta \int v_\alpha \partial_{v_\beta} f \, dv = \frac{1}{\tau} \int (f^0 v_\alpha - f v_\alpha) \, dv \\
\Rightarrow & \partial_t \int v_\alpha f \, dv + \partial_\beta \int v_\alpha v_\beta f \, dv + F_\beta \int v_\alpha \partial_{v_\beta} f \, dv = \frac{1}{\tau} (n u_\alpha - n u_\alpha) \\
\Rightarrow & \partial_t \int v_\alpha f \, dv + \partial_\beta \int v_\alpha v_\beta f \, dv + F_\beta \int v_\alpha \partial_{v_\beta} f \, dv = 0
\end{aligned} \tag{I.22}$$

Now, we simplify each term of Eq. (I.22) one by one.

Third term of left hand side of Eq. (I.22) is

$$\begin{aligned}
F_\beta \int v_\alpha \partial_{v_\beta} f \, dv &= F_\beta \left[v_\alpha \int \partial_{v_\beta} f \, dv - \int \left(\int \partial_{v_\beta} f \, dv \right) dv \right] \\
&= F_\beta \left[v_\alpha \partial_{v_\beta} \int f \, dv - \int (\partial_{v_\beta} \int f \, dv) dv \right] \\
&= F_\beta (v_\alpha \partial_{v_\beta} n - \int f \, dv) \\
&= F_\beta (0 - n) \\
&= -n F_\alpha
\end{aligned} \tag{I.23}$$

Substituting Eq. (I.23) in Eq. (I.22), we get

$$\begin{aligned}\partial_t \int v_\alpha f dv + \partial_\beta \int v_\alpha v_\beta f dv - nF_\alpha &= 0 \\ \Rightarrow \partial_t(nu_\alpha) + \partial_\beta \int v_\alpha v_\beta f dv - nF_\alpha &= 0\end{aligned}\quad (\text{I.24})$$

Eq. (I.21) can be re-written as

$$f = f^0 - \tau(\partial_t f + v_\gamma \partial_\gamma f + F_\gamma \partial_{v_\gamma} f).$$

multiplying “ $v_\alpha v_\beta$ ” with all the terms of the above equation and integrating, we get

$$\int f v_\alpha v_\beta dv = \int f^0 v_\alpha v_\beta dv - \tau \left[\int v_\alpha v_\beta \partial_t f dv + \int v_\alpha v_\beta v_\gamma \partial_\gamma f dv + F_\gamma \int v_\alpha v_\beta \partial_{v_\gamma} f dv \right] \quad (\text{I.25})$$

If we evaluate Eq. (I.25) upto first order in derivative (by doing Taylor series expansion around the equilibrium point) and substitute it in Eq. I.22 we will get Euler equation.

Up to first order in derivative,

$$\begin{aligned}\int f v_\alpha v_\beta dv &= \int f^0 v_\alpha v_\beta dv \\ \Rightarrow \int f v_\alpha v_\beta dv &= nu_\alpha u_\beta + n\theta \delta_{\alpha\beta}\end{aligned}\quad (\text{I.26})$$

Substituting Eq. (I.26) in Eq. (I.24), we get

$$\begin{aligned}\partial_t(nu_\alpha) + \partial_\beta(nu_\alpha u_\beta + n\theta \delta_{\alpha\beta}) - nF_\alpha &= 0 \\ \Rightarrow \partial_t(nu_\alpha) + \partial_\beta(nu_\alpha u_\beta) = nF_\alpha - \partial_\beta(n\theta \delta_{\alpha\beta})\end{aligned}\quad (\text{I.27})$$

where Kronecker delta, $\delta_{\alpha\beta}$, is given as

$$\delta_{\alpha\beta} = \begin{cases} 1, & \alpha = \beta \\ 0, & \alpha \neq \beta. \end{cases} \quad (\text{I.28})$$

So, we can write Eq. (I.27) as

$$\partial_t(nu_\alpha) + \partial_\beta(nu_\alpha u_\beta) = nF_\alpha - \partial_\alpha(n\theta) \quad (\text{I.29})$$

$$\begin{aligned}\Rightarrow u_\alpha \partial_t n + n \partial_t u_\alpha + u_\alpha \partial_\beta(nu_\beta) + nu_\beta \partial_\beta u_\alpha &= nF_\alpha - \partial_\alpha(n\theta) \\ \Rightarrow u_\alpha(\partial_t n + \partial_\beta(nu_\beta)) + n \partial_t u_\alpha + nu_\beta \partial_\beta u_\alpha &= nF_\alpha - \partial_\alpha(n\theta)\end{aligned}\quad (\text{I.30})$$

The bracketed term of left hand side of Eq. (I.30) is zero by equation of continuity(Eq. (I.20)). So, Eq. (I.30) can be written as

$$\partial_t u_\alpha + u_\beta \partial_\beta u_\alpha = F_\alpha - \frac{1}{n} \partial_\alpha(n\theta). \quad (\text{I.31})$$

We will use Eqs. (I.30) and (I.31) when we will derive Eq. (I.23) up to second order in derivative and then we will substitute that in Eq. (I.24). That will give us the Navier Stokes equation. So, we have to evaluate three more terms of Eq. (I.25).

Force term in Eq. (I.25) is

$$\begin{aligned}
F_\gamma \int v_\alpha v_\beta \partial_{v_\gamma} f dv &= F_\gamma \left[v_\alpha v_\beta \left(\int \partial_{v_\gamma} f dv \right) - \int (v_\alpha v_\beta)' \left(\int \partial_{v_\gamma} f dv \right) \right] \\
&= F_\gamma \left[v_\alpha v_\beta \partial_{v_\gamma} \left(\int f dv \right) - \int (v_\alpha + v_\beta) \left(\int \partial_{v_\gamma} f dv \right) \right] \\
&= F_\gamma \left[v_\alpha v_\beta \partial_{v_\gamma} n - \int (v_\beta + v_\alpha) f dv \right] \\
&= F_\gamma (-nu_\beta - nu_\alpha) \\
&= -nF_\alpha u_\beta - nF_\beta u_\alpha
\end{aligned} \tag{I.32}$$

Substituting Eq. (I.32) in Eq. (I.25), we get

$$\int f v_\alpha v_\beta dv = \int f^0 v_\alpha v_\beta dv - \tau \left[\partial_t \int f^0 v_\alpha v_\beta dv + \partial_\gamma \int f^0 v_\alpha v_\beta v_\gamma dv - nF_\alpha u_\beta - nF_\beta u_\alpha \right] \tag{I.33}$$

While obtaining Eq. (I.33) from Eq. (I.25), we have also made the following approximation

$$\begin{aligned}
\partial_t \int f v_\alpha v_\beta dv &\approx \partial_t \int f^0 v_\alpha v_\beta dv, \\
\partial_\gamma \int f v_\alpha v_\beta v_\gamma dv &\approx \partial_\gamma \int f^0 v_\alpha v_\beta v_\gamma dv.
\end{aligned}$$

The time derivative term of Eq. (I.33) can be simplify as

$$\begin{aligned}
\partial_t \left(\int f^0 v_\alpha v_\beta dv \right) &= \partial_t (nu_\alpha u_\beta + n\theta \delta_{\alpha\beta}) \\
&= u_\beta \partial_t (nu_\alpha) + nu_\alpha \partial_t u_\beta + \theta \delta_{\alpha\beta} \partial_t n + n \partial_t \theta \delta_{\alpha\beta}
\end{aligned} \tag{I.34}$$

From Eq. (I.29), we can say that

$$\partial_t (nu_\alpha) = nF_\alpha - \partial_\alpha (n\theta) - \partial_\gamma (nu_\alpha u_\gamma) \tag{I.35}$$

From Eq. I.31, we can say that

$$\partial_t u_\beta = F_\beta - \frac{1}{n} \partial_\beta (n\theta) - u_\gamma \partial_\gamma u_\beta \tag{I.36}$$

From equation of continuity(Eq. I.20), we can say that

$$\partial_t n = -\partial_\gamma (nu_\gamma) \tag{I.37}$$

and we use the relation

$$\partial_t \theta = -u_\gamma \partial_\gamma \theta - \frac{2}{3} \partial_\gamma (\theta u_\gamma) \tag{I.38}$$

We have used the above relation directly but this can also be derived from by multiplying $(v - u)^2$ with Eq. (I.22). Substituting Eqs. (I.35), (I.36), (I.37) and (I.38) in Eq. (I.34), we get

$$\begin{aligned}
\partial_t \left(\int f^0 v_\alpha v_\beta dv \right) &= u_\beta \left[nF_\alpha - \partial_\alpha (n\theta) - \partial_\gamma (nu_\alpha u_\gamma) \right] + nu_\alpha \left[F_\beta - \frac{1}{n} \partial_\beta (n\theta) - u_\gamma \partial_\gamma u_\beta \right] \\
&\quad + \theta \delta_{\alpha\beta} (-\partial_\gamma (nu_\gamma)) + n \delta_{\alpha\beta} \left[-u_\gamma \partial_\gamma \theta - \frac{2}{3} \partial_\gamma (\theta u_\gamma) \right]
\end{aligned} \tag{I.39}$$

The space derivative term in Eq. (I.33) can be simplified as

$$\begin{aligned}
\partial_\gamma \int f^0 v_\alpha v_\beta v_\gamma dv &= \partial_\gamma [n\theta(u_\alpha \delta_{\beta\gamma} + u_\beta \delta_{\alpha\gamma} + u_\gamma \delta_{\alpha\beta}) + nu_\alpha u_\beta u_\gamma] \\
&= \partial_\gamma(n\theta u_\alpha \delta_{\beta\gamma}) + \partial_\gamma(n\theta u_\beta \delta_{\alpha\gamma}) + \partial_\gamma(n\theta u_\gamma \delta_{\alpha\beta}) + \partial_\gamma(nu_\alpha u_\beta u_\gamma) \\
&= \partial_\beta(n\theta u_\alpha) + \partial_\alpha(n\theta u_\beta) + \partial_\gamma(n\theta u_\gamma \delta_{\alpha\beta}) + \partial_\gamma(nu_\alpha u_\beta u_\gamma)
\end{aligned} \tag{I.40}$$

Adding Eqs. (I.39) and (I.40), we get

$$\begin{aligned}
\partial_t \left(\int f^0 v_\alpha v_\beta dv \right) + \partial_\gamma \int f^0 v_\alpha v_\beta v_\gamma dv &= -\partial_\gamma(nu_\alpha u_\beta u_\gamma) - u_\alpha \partial_\beta(n\theta) - u_\beta \partial_\alpha(n\theta) \\
&\quad + n(F_\alpha u_\beta + F_\beta u_\alpha) - \delta_{\alpha\beta} \partial_\gamma(nu_\gamma \theta) - \frac{2}{3} n \delta_{\alpha\beta} \partial_\gamma(\theta u_\gamma) \\
&\quad + \partial_\beta(n\theta u_\alpha) + \partial_\alpha(n\theta u_\beta) + \partial_\gamma(n\theta u_\gamma \delta_{\alpha\beta}) + \partial_\gamma(nu_\alpha u_\beta u_\gamma) \\
&= n\theta \partial_\beta(u_\alpha) + n\theta \partial_\alpha(u_\beta) + n(F_\alpha u_\beta + F_\beta u_\alpha) - \frac{2}{3} n \delta_{\alpha\beta} \partial_\gamma(\theta u_\gamma)
\end{aligned} \tag{I.41}$$

Substituting Eq. (I.41) in Eq. (I.33), we get

$$\begin{aligned}
\partial_t \int f v_\alpha v_\beta dv &= nu_\alpha u_\beta + n\theta \delta_{\alpha\beta} \\
&\quad - \tau \left[n\theta(\partial_\beta u_\alpha + \partial_\alpha u_\beta) + n(F_\alpha u_\beta + F_\beta u_\alpha) - \frac{2}{3} n \delta_{\alpha\beta} \partial_\gamma(u_\gamma \theta) - nF_\alpha u_\beta - nF_\beta u_\alpha \right] \\
&\Rightarrow \int f v_\alpha v_\beta dv = nu_\alpha u_\beta + n\theta \delta_{\alpha\beta} - n\theta \tau \left(\partial_\beta u_\alpha + \partial_\alpha u_\beta - \frac{2}{3} \delta_{\alpha\beta} \partial_\gamma(u_\gamma) \right) \\
&\Rightarrow \int f v_\alpha v_\beta dv = nu_\alpha u_\beta + n\theta \delta_{\alpha\beta} - \eta \left(\partial_\beta u_\alpha + \partial_\alpha u_\beta - \frac{2}{3} \delta_{\alpha\beta} \partial_\gamma(u_\gamma) \right)
\end{aligned} \tag{I.42}$$

where $\eta = n\theta\tau$.

Now, substituting Eq. (I.42) in Eq. (I.25), we get

$$\begin{aligned}
\partial_t(nu_\alpha) + \partial_\beta \left[nu_\alpha u_\beta + n\theta \delta_{\alpha\beta} - \eta \left(\partial_\beta u_\alpha + \partial_\alpha u_\beta - \frac{2}{3} \delta_{\alpha\beta} \partial_\gamma(u_\gamma) \right) \right] - nF_\alpha &= 0 \\
\Rightarrow \partial_t(nu_\alpha) + \partial_\beta(nu_\alpha u_\beta) + \partial_\beta(n\theta) \delta_{\alpha\beta} = nF_\alpha + \partial_\beta \left[\eta \left(\partial_\beta u_\alpha + \partial_\alpha u_\beta - \frac{2}{3} \delta_{\alpha\beta} \partial_\gamma(u_\gamma) \right) \right]
\end{aligned} \tag{I.43}$$

For $\alpha = \beta$, $\delta_{\alpha\beta} = 1$.

So, Eq. (I.43) can be written as

$$\begin{aligned}
u_\alpha \partial_t n + n \partial_t(u_\alpha) + u_\alpha \partial_\beta(nu_\beta) + nu_\beta \partial_\beta u_\alpha &= -\partial_\alpha(n\theta) + nF_\alpha + \partial_\beta \left[\eta \left(\partial_\beta u_\alpha + \partial_\alpha u_\beta - \frac{2}{3} \delta_{\alpha\beta} \partial_\gamma(u_\gamma) \right) \right] \\
\Rightarrow u_\alpha \left(\partial_t n + \partial_\beta(nu_\beta) \right) + n \partial_t(u_\alpha) + nu_\beta \partial_\beta u_\alpha &= -\partial_\alpha(n\theta) + nF_\alpha + \partial_\beta \left[\eta \left(\partial_\beta u_\alpha + \partial_\alpha u_\beta - \frac{2}{3} \delta_{\alpha\beta} \partial_\gamma(u_\gamma) \right) \right]
\end{aligned} \tag{I.44}$$

Using equation of continuity i.e Eq. (I.20) in the above equation, we get

$$n\partial_t(u_\alpha) + nu_\beta\partial_\beta u_\alpha = -\partial_\alpha(n\theta) + nF_\alpha + \partial_\beta \left[\eta \left(\partial_\beta u_\alpha + \partial_\alpha u_\beta - \frac{2}{3}\delta_{\alpha\beta}\partial_\gamma(u_\gamma) \right) \right]. \quad (\text{I.45})$$

Eq. (I.45) is the compressible Navier stokes equation in tensor notation.

He & Luo (1997*a,b*) gave a much needed theoretical foundation to the lattice Boltzmann method by deriving the lattice Boltzmann equation from the Boltzmann equation. Navier-Stokes equation can also be derived from the lattice Boltzmann equation by following the Chapman-Enskog multi-scale expansion. A detail derivation of Navier-Stokes equation from lattice Boltzmann equation was also given by Dr. Erlend M. Viggen in his doctoral thesis [Viggen (2009)].

Bibliography

- BAI, R., CHEN, K. & JOSEPH, D. D. 1992 Lubricated pipelining: stability of core annular flow. part 5. experiments and comparison with theory. *J. Fluid Mech.* **240**, 97–132.
- BAIRD, M., ARAVAMUDAN, K., RAMA RAO, N. V., CHADAM, J. & PIERCE, A. P. 1992 Unsteady axial mixing by natural convection in a vertical column. *AIChE J.* **38**, 1825–1834.
- BENJAMIN, T. B. 1968 Gravity currents and related phenomena. *J. Fluid Mech.* **31**, 209–248.
- BHATNAGAR, P. L., GROSS, E. P. & KROOK, M. 1954 A model for collision process in gases. I. Small amplitude processes in charged and neutral one-component system. *Phys. Rev.* **94**, 511–525.
- BOOMKAMP, P. A. M. & MIESEN, R. H. M. 1996 Classification of instabilities in parallel two-phase flow. *Int. J. Multiphase Flow* **22**, 67–88.
- CAO, Q., VENTRESCA, L., SREENIVAS, K. R. & PRASAD, A. K. 2003 Instability due to viscosity stratification downstream of a centreline injector. *Can. J. Chem. Eng.* **81**, 913–922.
- CARNAHAN, N. F. & STARLING, K. E. 1969 Equation of state for non-attracting rigid spheres. *J. Chem. Phys.* **51**, 635–636.
- CHANG, Q. & ALEXANDER, J. I. D. 2006 Application of the lattice Boltzmann method to two-phase Rayleigh-Benard convection with a deformable interface. *J. Comput. Phys.* **212**, 473–489.
- CHARLES, M. E., GOVIER, G. W. & HODGSON, G. W. 1961 The horizontal pipeline flow of equal density oil-water mixtures. *Can. J. Chem. Eng.* **39**, 27–36.
- CHEN, C.-Y. & MEIBURG, E. 1996 Miscible displacement in capillary tubes. Part 2. Numerical simulations. *J. Fluid Mech.* **326**, 57–90.
- CHEN, S. & DOOLEN, G. D. 1998 Lattice Boltzmann method for fluid flows. *Ann. Rev. Fluid Mech.* **30**, 329–364.
- CHEN, S., MARTINEZ, D. & MEI, R. 1996 On boundary conditions in lattice Boltzmann methods. *Phys. Fluids* **8**, 2527–2536.
- CHIN, J., BOEK, E. S. & COVENEY, P. V. 2002 Lattice Boltzmann simulation of the flow of binary immiscible fluids with different viscosities using the Shan-Chen microscopic interaction model. *Phil. Trans. Math. Phys. Eng. Sci.* **360**, 547–558.
- CHORIN, A. J. 1967 A numerical method for solving incompressible viscous flow problems. *J. Comput. Phys.* **2**, 12–26.

- CLAYTON, T., SOMMERFIELD, M. S. & TSUJI, Y. 1998 *Multiphase flows with droplets and particles*. CRC Press.
- COX, B. G. 1962 On driving a viscous fluid out of a tube. *J. Fluid Mech.* **14**, 81–96.
- DEBACQ, M., HULIN, J. P., SALIN, D., PERRIN, B. & HINCH, E. J. 2003 Buoyant mixing of miscible fluids of varying viscosities in vertical tubes. *Phys. Fluids* **15** (12), 3846–3855.
- DING, H., SPELT, P. D. M. & SHU, C. 2007 Diffuse interface model for incompressible two-phase flows with large density ratios. *J. Comput. Phys* **226**, 2078–2095.
- D’OLCE, M., J. MARTIN, N. RAKOTOMALALA, D. S. & TALON, L. 2008 Pearl and mushroom instability patterns in two miscible fluids core annular flows. *Phys. Fluids* **20**, 024104(1–4).
- DONG, B., YAN, Y. Y., LI, W. & SONG, Y. 2010 Lattice Boltzmann simulation of viscous fingering phenomenon of immiscible fluids displacement in a channel. *Computers & Fluids* **39**, 768–779.
- ERN, P., CHARRU, F. & LUCHINI, P. 2003 Stability analysis of a shear flow with strongly stratified viscosity. *J. Fluid Mech.* **496**, 295–312.
- FAKHARI, A. & RAHIMIAN, M. H. 2009 Simulation of falling droplet by the lattice Boltzmann method. *Communications in Nonlinear Science and Numerical Simulations* **14**, 3046–3055.
- FAKHARI, A. & RAHIMIAN, M. H. 2010 Investigation of deformation and breakup of a moving droplet by the method of lattice Boltzmann equations. *Int. J. Numer. Meth. Fluids* **64**, 827–849.
- FRIGAARD, I. A. 2001 Super-stable parallel flows of multiple visco-plastic fluids. *J. Non-Newt. Fluid Mech.* **100**, 49–76.
- GABARD, C. & HULIN, J.-P. 2003 Miscible displacement of non-Newtonian fluids in a vertical tube. *Eur. Phys. J. E.* **11**, 231–241.
- GOVINDARAJAN, R. 2004 Effect of miscibility on the linear instability of two-fluid channel flow. *Int. J. Multiphase Flow* **30**, 1177–1192.
- GOVINDARAJAN, R., L’VOV, S. V. & PROCACCIA, I. 2001 Retardation of the onset of turbulence by minor viscosity contrasts. *Phys. Rev. Lett.* **87**, 174501(1–4).
- GOYAL, N. & MEIBURG, E. 2006 Miscible displacements in Hele-Shaw cells: two-dimensional base states and their linear stability. *J. Fluid Mech.* **558**, 329–355.
- GOYAL, N., PICHLER, H. & MEIBURG, E. 2007 Variable-density miscible displacements in a vertical Hele-Shaw cell: linear stability. *J. Fluid Mech.* **584**, 357–372.
- GROSFILS, P., BOON, J. P. & CHIN, J. 2004 Structural and dynamical characterization of Hele-Shaw viscous fingering. *Phil. Trans. Math. Phys. Eng. Sci.* **362**, 1723–1734.
- GRUNAU, D., CHEN, S. & EGGERT, K. 1993 A lattice Boltzmann model for multiphase fluid flows. *Phys. Fluids A*, **5**, 2557.
- GUNSTENSEN, A. K., ROTHMAN, D. H., ZALESKI, S. & ZANETTI, G. 1991 Lattice Boltzmann model for immiscible fluids. *Phys. Rev. A*, **43**, 4320–4327.
- GUO, Z., ZHENG, C. & SHI, B. 2002 An extrapolation method for boundary conditions in lattice Boltzmann method. *Phys. Fluids* **14**, 2007–2010.

- HALLEZ, Y. & MAGNAUDET, J. 2008 Effects of channel geometry on buoyancy-driven mixing. *Phys. Fluids* **20**, 053306(1–9).
- HE, X., CHEN, S. & ZHANG, R. 1999a A lattice Boltzmann scheme for incompressible multiphase flow and its application in simulation of Rayleigh-Taylor instability. *J. Comput. Phys* **152**, 642–663.
- HE, X. & LUO, L. S. 1997a A priori derivation of the lattice Boltzmann equation. *Physical Review E* **55**, 6811–6817.
- HE, X. & LUO, L. S. 1997b Theory of the lattice Boltzmann method: From the Boltzmann equation to the lattice Boltzmann equation. *Physical Review E* **56**, R6333–R6336.
- HE, X., ZHANG, R., CHEN, S. & DOOLEN, G. D. 1999b On the three-dimensional Rayleigh-Taylor instability. *Phys. Fluids* **11(5)**, 1143–1152.
- HICKOX, C. E. 1971 Instability due to viscosity and density stratification in axisymmetric pipe flow. *Phys. Fluids* **14**, 251–262.
- HILL, S., M.A., P. F. & F.S.S 1952 Channeling in packed columns. *Chem. Engng. Sci.* **1**, 247–253.
- HINCH, E. J. 1984 A note on the mechanism of the instability at the interface between two shearing fluids. *J. Fluid Mech.* **144**, 463–465.
- HOMSY, G. M. 1987 Viscous fingering in porous media. *Ann. Rev. Fluid Mech.* **19**, 271–311.
- HOOPER, A. P. & BOYD, W. G. C. 1983 Shear flow instability at the interface between two fluids. *J. Fluid Mech.* **128**, 507–528.
- HOOPER, A. P. & GRIMSHAW, R. 1985 Nonlinear instability at the interface between two viscous fluids. *Phys. Fluids* **28(1)**, 37–45.
- HU, H. H. & JOSEPH, D. D. 1989 Lubricated pipelining: Stability of core-annular flow. Part 2. *J. Fluid Mech.* **205**, 359–396.
- HU, H. H., LUNDGREN, T. S. & JOSEPH, D. D. 1990 Stability of core-annular flow with very small viscosity ratio. *Phys. Fluids A* **2**, 1945–1954.
- HU, H. H. & PATANKAR, N. 1995 Non-axisymmetric instability of core-annular flow. *J. Fluid Mech.* **290**, 213–224.
- JOSEPH, D. D., BAI, R., CHEN, K. P. & RENARDY, Y. Y. 1997 Core-annular flows. *Ann. Rev. Fluid Mech.* **29**, 65–94.
- JOSEPH, D. D., RENARDY, M. & RENARDY, Y. Y. 1984 Instability of the flow of two immiscible liquids with different viscosities in a pipe. *J. Fluid Mech.* **141**, 309–317.
- KANG, Q., ZHANG, D. & CHEN, S. 2004 Immiscible displacement in a channel: simulations of fingering in two dimensions. *Adv. Water Resour.* **27**, 13–22.
- KAO, T. W. & PARK, C. 1972 Experimental investigations of the stability of channel flows. part 2. two-layered co-current flow in a rectangular channel. *J. Fluid Mech.* **52**, 401–423.
- KOURIS, C. & TSAMOPOULOS, J. 2001 Dynamics of axisymmetric core-annular flow in a straight tube. I. The more viscous fluid in the core, bamboo waves. *Phys. Fluids* **13**, 841–858.

- KOURIS, C. & TSAMOPOULOS, J. 2002 Dynamics of axisymmetric core-annular flow in a straight tube. II. The less viscous fluid in the core, saw tooth waves. *Phys. Fluids* **14**, 1011–1029.
- KUANG, J., MAXWORTHY, T. & PETITJEANS, P. 2003 Miscible displacements between silicone oils in capillary tubes. *Eur. J. Mech.* **22**, 271–277.
- LAJEUNESSE, E., MARTIN, J., RAKOTOMALALA, N. & SALIN, D. 1997 3D instability of miscible displacements in a Hele-Shaw cell. *Phys. Rev. Lett.* **79**, 5254–5257.
- LAJEUNESSE, E., MARTIN, J., RAKOTOMALALA, N., SALIN, D. & YORTSOS, Y. C. 1999 Miscible displacement in a Hele-Shaw cell at high rates. *J. Fluid Mech.* **398**, 299–319.
- LATVA-KOKKO, M. & ROTHMAN, D. H. 2005 Diffusion properties of gradient-based lattice Boltzmann models of immiscible fluids. *Phys. Rev. E* **71**, 056702(1–8).
- LEE, H. G. & KIM, J. 2013 Buoyancy-driven mixing of multi-component fluids in two-dimensional tilted channels. *European J. of Mechanics B/Fluids* **42**, 37–46.
- LEE, T. & LIN, C.-L. 2005 A stable discretization of the lattice Boltzmann equation for simulation of incompressible two-phase flows at high density ratio. *J. Comput. Phys* **206**, 16–47.
- LI, J. & RENARDY, Y. Y. 1999 Direct simulation of unsteady axisymmetric core-annular flow with high viscosity ratio. *J. Fluid Mech.* **391**, 123–149.
- LI, S. M. & TAFTI, D. K. 2009 Near-critical CO₂ liquid-vapor flow in a sub-microchannel. part i: Mean-field free-energy D2Q9 lattice Boltzmann method. *Int. J. Multiphase Flow* **35**, 725–737.
- LI, W., FAN, Z., WEI, X. & KAUFMAN, A. 2005 GPU-based flow simulation with complex boundaries. *GPU Gems II, Chapter 47, Addison Wesley* .
- LISHCHUK, S. V., HALLIDAY, I. & CARE, C. M. 2008 Multicomponent lattice Boltzmann method for fluids with a density contrast. *Phys. Rev. E* **77**, 036702(1–8).
- MALIK, S. V. & HOOPER, A. P. 2005 Linear stability and energy growth of viscosity stratified flows. *Phys. Fluids* **17**, 024101(1–9).
- MELCHER, J. & TAYLOR, G. 1969 Electrohydrodynamics: A review of the role of interfacial shear stresses. *Ann. Rev. Fluid Mech.* **1**, 111–146.
- MOHAMMADI, S. M., CARRASCO-TEJA, M., STOREY, S., FRIGAARD, I. A. & MARTINEZ, D. M. 2010 An experimental study of laminar displacement flows in narrow vertical eccentric annuli. *J. Fluid Mech.* **649**, 371–398.
- NOBLE, D. R., GEORGIADIS, J. G. & BUCKIUS, R. O. 1995 Direct assessment of lattice Boltzmann hydrodynamics and boundary conditions for recirculating flows. *J. Stat. Phys.* **81**, 17–33.
- NOUAR, C., KABOUYA, N., DUSEK, J. & MAMOU, M. 2007 Modal and non-modal linear stability of the plane Bingham-Poiseuille flow. *J. Fluid Mech.* **577**, 211–239.
- NVIDIA 2010 NVIDIA CUDA C programming guide. *Version 3.2* .
- OLIVEIRA, R. M. & MEIBURG, E. 2011 Miscible displacements in Hele-Shaw cells: three-dimensional Navier-Stokes simulations. *J. Fluid Mech.* **687**, 431–460.

- PENG, L., NOMURA, K., OYAKAWA, T., KALIA, R., NAKANO, A. & VASHISHTA, P. 2008 Parallel lattice Boltzmann flow simulation on emerging multi-core platforms. *Euro-Par2008 - Parallel Processing* **5168**, *Lecture Notes in Computer Science*, 763–777.
- PETITJEANS, P. & MAXWORTHY, P. 1996 Miscible displacements in capillary tubes. Part 1. Experiments. *J. Fluid Mech.* **326**, 37–56.
- PREMNATH, K. N. & ABRAHAM, J. 2005 Lattice Boltzmann model for axisymmetric multiphase flows. *Phys. Rev. E* **71**, 056706(1–17).
- PREZIOSI, L., CHEN, K. & JOSEPH, D. D. 1989 Lubricated pipelining: Stability of core-annular flow. *J. Fluid Mech.* **201**, 323–350.
- QIAN, Y. H., DHUMI'RES, D. & LALLEMAND, P. 1992 Lattice BGK models for Navier-Stokes equation. *Europhys. Lett.* **17**, 479–84.
- RAKOTOMALALA, N., SALIN, D. & WATZKY, P. 1997 Miscible displacement between two parallel plates: BGK lattice gas simulations. *J. Fluid Mech.* **338**, 277–297.
- RANGANATHAN, B. T. & GOVINDARAJAN, R. 2001 Stabilisation and destabilisation of channel flow by location of viscosity-stratified fluid layer. *Phys. Fluids*. **13**(1), 1–3.
- REDAPANGU, P. R., VANKA, S. P. & SAHU, K. C. 2012 Multiphase lattice Boltzmann simulations of buoyancy-induced flow of two immiscible fluids with different viscosities. *European Journal of Mechanics B/Fluids* **34**, 105–114.
- REGNER, M., HENNINGSSON, M., WIKLUND, J., ÖSTERGREN, K. & TRÄGÅRDH, C. 2007 Predicting the displacement of yoghurt by water in a pipe using CFD. *Chem. eng. Technology* **30**, 844–853.
- RENARDY, Y. Y. & JOSEPH, D. D. 1985 Couette-flow of two fluids between concentric cylinders. *J. Fluid Mech.* **150**, 381–394.
- RIAZ, A. & MEIBURG, E. 2003 Three-dimensional miscible displacement simulations in homogeneous porous media with gravity override. *J. Fluid Mech.* **494**, 95–117.
- RIVET, J. P. & BOON, J. P. 2000 *Lattice Gas Hydrodynamics*. Cambridge University Press.
- ROTHMAN, D. & ZALESKI, S. 1997 *Lattice Gas Cellular Automata: Simple models of Complex Hydrodynamics*. Cambridge University Press.
- SAFFMAN, P. G. & TAYLOR, G. I. 1958 The penetration of a fluid into a porous medium or Hele–Shaw cell containing a more viscous liquid. *Proc. R. Soc. Lond. A* **245**, 312–329.
- SAHU, K. C., DING, H., VALLURI, P. & MATAR, O. K. 2009a Linear stability analysis and numerical simulation of miscible two-layer channel flow. *Phys. Fluids* **21**, 042104(1–8).
- SAHU, K. C., DING, H., VALLURI, P. & MATAR, O. K. 2009b Pressure-driven miscible two-fluid channel flow with density gradients. *Phys. Fluids* **21**, 043603(1–10).
- SAHU, K. C. & GOVINDARAJAN, R. 2011 Linear stability of double-diffusive two-fluid channel flow. *J. Fluid Mech.* **687**, 529–539.
- SAHU, K. C. & GOVINDARAJAN, R. 2014 Instabilities in viscosity-stratified flow. *Ann. Rev. Fluid Mech.* **46**, 331–353.

- SAHU, K. C. & MATAR, O. K. 2010 Three-dimensional linear instability in pressure-driven two-layer channel flow of a Newtonian and a Herschel-Bulkley fluid. *Phys. Fluids* **22**, 112103(1–14).
- SAHU, K. C. & MATAR, O. K. 2011 Three-dimensional convective and absolute instabilities in pressure-driven two-layer channel flow. *Int. J. Numer. Meth. Fluids* **37**, 987–993.
- SAHU, K. C., VALLURI, P., SPELT, P. D. M. & MATAR, O. K. 2007 Linear instability of pressure-driven channel flow of a Newtonian and Herschel-Bulkley fluid. *Phys. Fluids* **19**, 122101(1–11).
- SAHU, K. C. & VANKA, S. P. 2011 A multiphase lattice Boltzmann study of buoyancy-induced mixing in a tilted channel. *Computers & Fluids* **50**, 199–215.
- SCOFFONI, J., LAJEUNESSE, E. & HOMSY, G. M. 2001 Interface instabilities during displacement of two miscible fluids in a vertical pipe. *Phys. Fluids* **13**, 553–556.
- SELVAM, B., MERK, S., GOVINDARAJAN, R. & MEIBURG, E. 2007 Stability of miscible core-annular flows with viscosity stratification. *J. Fluid Mech.* **592**, 23–49.
- SELVAM, B., TALON, L., LESSHAFFT, L. & MEIBURG, E. 2009 Convective/absolute instability in miscible core-annular flow. Part 2. Numerical simulations and nonlinear global modes. *J. Fluid Mech.* **618**, 323–348.
- SÉON, T., HULIN, J. P., SALIN, D., PERRIN, B. & HINCH, E. J. 2006a From turbulent mixing to gravity currents in tilted tubes. *Phys. Fluids* **18**, 091103.
- SÉON, T., HULIN, J. P., SALIN, D., PERRIN, B. & J., H. E. 2006b Laser-induced fluorescence measurements of buoyancy driven mixing in tilted tubes. *Phys. Fluids* **18**, 041701(1–4).
- SÉON, T., SALIN, D., HULIN, J. P., HINCH, E. J. & PERRIN, B. 2007a Transient buoyancy-driven front dynamics in nearly horizontal tubes. *Phys. Fluids* **19**, 123603(1–4).
- SÉON, T., SALIN, D., HULIN, J. P., PERRIN, B. & HINCH, E. J. 2004 Buoyant mixing of miscible fluids in tilted tubes. *Phys. Fluids* **16**, L103–L106.
- SÉON, T., SALIN, D., HULIN, J. P., PERRIN, B. & HINCH, E. J. 2005 Buoyancy driven front dynamics in tilted tubes. *Phys. Fluids* **17**, 031702(1–4).
- SÉON, T., ZNAIEN, J., PERRIN, B., HINCH, E. J., SALIN, D. & HULIN, J. P. 2007b Front dynamics and macroscopic diffusion in buoyant mixing in a tilted tube. *Phys. Fluids* **19** (12), 125105(1–7).
- SHAN, X. & CHEN, H. 1993a Lattice Boltzmann model for simulating flows with multiple phases and components. *Phys. Rev. E* **47**, 1815–1819.
- SHAN, X. & CHEN, H. 1993b Lattice Boltzmann model for simulating flows with multiple phases and components. *Phys. Rev. E* **47**(3), 1815–1819.
- SHAN, X. & DOOLEN, G. 1995 Multicomponent lattice-Boltzmann model with interparticle interaction. *J. Stat. Phys* **81**, 379–393.
- SHUI, L., EIJKEL, J. C. T. & BERG, A. V. D. 2007 Multiphase flow in micro and nanochannels. *Sensors and Actuators* **121**, 263–276.
- SQUIRE, H. B. 1933 On the stability for three-dimensional disturbances of viscous fluid flow between parallel walls. *Proc. Roy. Soc. London Ser. A* **142**, 621–628.

- SWIFT, M. R., ORLANDINI, S. E., OSBORN, W. R. & YEOMANS, J. M. 1996 Lattice-Boltzmann simulations of liquid-gas and binary-fluid systems. *Phys. Rev. E* **54**, 5041–5052.
- SWIFT, M. R., OSBORN, W. R. & YEOMANS, J. M. 1995 Lattice-Boltzmann simulation of nonideal fluids. *Phys. Rev. Lett.* **75**, 830–833.
- TAGHAVI, S. M., ALBA, K., SÉON, T., WIELAGE-BURCHARD, K., MARTINEZ, D. M. & FRIGAARD, I. A. 2012 Miscible displacement flows in near-horizontal ducts at low Atwood number. *J. Fluid Mech.* **696**, 175–214.
- TAGHAVI, S. M., SÉON, T., MARTINEZ, D. M. & FRIGAARD, I. A. 2010 Influence of an imposed flow on the stability of a gravity current in a near horizontal duct. *Phys. Fluids* **22**, 031702(1–4).
- TAGHAVI, S. M., SÉON, T., MARTINEZ, D. M. & FRIGAARD, I. A. 2011 Stationary residual layers in buoyant Newtonian displacement flows. *Phys. Fluids* **23**, 044105(1–15).
- TAN, C. T. & HOMS, G. M. 1986 Stability of miscible displacements: rectangular flow. *Phys. Fluids* **29**, 73549.
- TAYLOR, G. I. 1961 Deposition of viscous fluid on the wall of a tube. *J. Fluid Mech.* **10**, 161–165.
- TOLKE, J. 2008 Implementation of a lattice Boltzmann kernel using the compute unified device architecture developed by NVIDIA. *Computing and Visualization in Science* .
- VANKA, S. P., SHINN, A. F. & SAHU, K. C., ed. 2011 *Computational fluid dynamics using graphics processing units: Challenges and Opportunities*, Denver, Colorado, USA. Proceedings of the ASME IMECE.
- VIGGEN, E. M. 2009 The lattice Boltzmann method with application in acoustics. PhD thesis, Department of Physics, NTNU.
- WAGNER, A. J. 2008 *A Practical Introduction to the Lattice Boltzmann Method*.
- WEI, H. H. & RUMSCHITZKI, D. S. 2002a The linear stability of a core-annular flow in an asymptotically corrugated tube. *J. Fluid Mech.* **466**, 113–147.
- WEI, H. H. & RUMSCHITZKI, D. S. 2002b The weakly nonlinear interfacial stability of a core-annular flow in a corrugated tube. *J. Fluid Mech.* **466**, 149–177.
- WHITEHEAD, J. A. & HELFRICH, K. R. 1991 Instability of the flow with temperature-dependent viscosity: a model of magma dynamics. *J. Geophysical Res.* **96**, 4145–4155.
- WU, L., TSUTAHARA, M., KIM, L. & HA, M. Y. 2008a Numerical simulations of droplet formation in a cross-junction microchannel by the lattice Boltzmann method. *Int. J. Numer. Meth. Fluids* **57**, 793–810.
- WU, L., TSUTAHARA, M., KIM, L. & HA, M. Y. 2008b Three dimensional lattice Boltzmann simulations of droplet formation in a cross-junction channel. *Int. J. Multiphase Flow* **34**, 852–864.
- YANG, Z. & YORTSOS, Y. C. 1997 Asymptotic solutions of miscible displacements in geometries of large aspect ratio. *Phys. Fluids* **9**, 286–298.
- YIANTSIOS, S. G. & HIGGINS, B. G. 1988a Linear stability of plane Poiseuille flow of two superposed fluids. *Phys. Fluids* **31**, 3225–3238.

YIANTSIOS, S. G. & HIGGINS, B. G. 1988*b* Numerical solution of eigenvalue problems using the compound matrix-method. *J. Comp. Phys.* **74**, 25–40.

YIH, C. S. 1967 Instability due to viscous stratification. *J. Fluid Mech.* **27**, 337–352.

ZHANG, R., HE, X. & CHEN, S. 2000 Interface and surface tension in incompressible lattice Boltzmann multiphase model. *Computer Physics Communications* **129**, 121–130.